Mass spectrometric investigation of the OH induced oxidation of isoprene using O_2^+ as a chemical ionization reagent

Aeysha Ahmad

A dissertation submitted to the Faculty of Graduate studies in partial fulfillment of the requirements for the degree of

Master's in Chemistry

Graduate program in Centre of Atmospheric Chemistry
York University
Toronto, Canada

December 2011

Mass spectrometric investigation of the OH Induced oxidation of isoprene using O_2^+ as a chemical ionization reagent

by **Aeysha Ahmad**

A dissertation submitted to the Faculty of Graduate Studies of York University in partial fulfillment of the requirements for the degree of

MASTER OF CHEMISTRY

Abstract

Isoprene (2-methyl-1,3-butadiene) is a dominant non-methane organic compound emitted into the atmosphere by vegetation, with an annual global emission rate of 500 Tg/yr. It represents almost 50% of all biogenic non-methane hydrocarbons on a global scale. It has a substantial impact on troposphere oxidants. The focus of this research is a preliminary investigation of isoprene oxidation reaction, in the presence of OH radicals and high NO_X concentrations.

An ion-trap time of flight mass spectrometer was used for analysis. It consisted of a source chamber and a flight tube. Main portion of the source chamber contained a quadrupole ion-trap where chemical ionization and ion storage took place. O_2^+ ions were used as chemical ionization reagent. Sample fragments were stored in the center of the ion-trap where their trajectories were stable, then after a certain period of storage time ejected simultaneously into the flight tube for mass analysis.

In order to trap heavier masses, conditions for ion-trap efficiency were improved and to achieve quantitative results, the mass spectrometer was calibrated and calibration spectra were generated for isoprene and its oxidation products. This helped in calculating concentrations, as a function of time, for reactants and products of isoprene oxidation. The percentage yields of the products (methacrolein and methyl vinyl ketone) were also determined.

Acknowledgements

I would like to thank my supervisor Dr. Michael Mozurkowich for his support. He has encouraged me to grow in various aspects of research work and his innovative thinking has been a great inspiration. I would also thank members of my supervisory committee Dr. J. Rudolph and Dr. G. W. Harris for their suggestions.

I have been fortunate to have worked with in a cohesive research group, especially Abdul Qadir. I valued many discussions we have had.

On a personal note, I would like to thank my mother for her encouragement through tough times. I'm also thankful to my daughters Sarah and Zara for being there for me and these three people I love the most in this world.

Table of Contents

List of symbols and abbreviations

A	Radius of the droplet
α	Alpha values / Response factors
$\alpha_{(58,acet)}$	Alpha value of m/z 58, contributed my acetone
A_1	Repeller plate
Acet	Acetone
β	Beta values (for second order reactions)
CO_2	Carbon dioxide
CO	Carbon monoxide
C_1	Sample concentration in ionization region
C_0	Initial mixing ratio
C_S	Sample flow concentration
CSTR	Continously stirred tank reactor
$C_{(t)}$	Concentration changing with time
$C_{(t),IPN,\ initial}$	Initial concentration of IPN changing with time, before turning on the UV lights
$C_{(t),acet,\ final}$	Final concentration of acetone changing with time, at the end of experiment
DC	Direct current
DDG	Digital delay generator
D_z	Depth of potential well in axial direction
D_r	Depth of potential well in radial direction

ρ	Density
e^- gun	Electron gun
e^-_p	Primary electrons
γ	Gemma
Σ	Sum of all values
GC-MS	Gas chromatographic – mass spectrometer
IPN	Isopropyl nitrite
Isop	Isoprene
IT-ToF MS	Ion-trap, time of flight mass spectrometer
LML	Lower mass limit
L/s	Litre per second
LV	Leak valve
MAC	Methacrolein
MCP	Microchannel plate detector
MFC	Mass flow controller
mV	Millivolts
MVK	Methyl vinyl ketone
m/z	Mass-to-charge ratio
N	Number of data points
NOx	$NO + NO_2$
NO	Nitric oxide
OH	Hydroxyl radical

POM	Particulate organic matter
Ppm	Parts per million
PTR-MS	Proton transfer reaction - mass spectrometry
P_{vap}	Vapour pressure
Q	Calibrated gas flow rate
Q_L	Liquid flow rate
R	Gas constant
RF	Radio frequency
R_0	Radius of ring electrode in central horizontal plane
RO_2	Alkyl peroxy radical
SOA	Secondary organic aerosol
S	Signal
S_0	Background signal
S_{43}	Overall signal at m/z 43
$S_{43,IPN}$	IPN contribution at m/z 43
$S_{39\text{-}isop}$	Left over signal at m/z 39 after removing isoprene contribution from it
τ_D	Dilution time constant
τ_I	Resident time constant
t_{avg}	Averaging interval
Tg/yr	Teragram per year

tau_I	Instrumental time constant
t_0	Time switched sample to ToF
ToF	Time of flight
UV	Ultraviolet
V	Volume of the flask
VOCs	Volatile organic compounds
V_npnts	Number of data points fitted
V_{SA}	Initial gas volume of analyte
ω_r	Fundamental radial secular frequency
ω_z	Fundamental axial secular frequency
z_0	Radius of ring electrode along axis of the ion trap

Chapter 1: Introduction

1.1: Motivation

Oxidation of volatile organic compounds (VOCs) plays an important role in our atmosphere. Some VOCs have high emission rates and play a major role in secondary particulate matter formation. These particles are involved in many current environmental issues such as climate change (*Eldering,* 1996), photochemical smog (*Volkame,* 2005), acid rain and visibility degradation (*Ghan,* 2007).

Particles in high concentrations have also been associated with adverse health effects and increased mortality (*Schlesinge,* 2003). Considering the adverse effects of these particles, it is important to investigate the oxidation processes of these volatile organic compounds.

On a global scale, total emissions of biogenic VOCs exceed the anthropogenic VOC emissions (*Guenther*, 1995) and isoprene is the most important biogenic volatile organic compound. It has the largest flux of any single hydrocarbon, apart from methane, with global emissions estimated between 250 and 503 Tg/yr (*Müller,* 1992; *Guenther,* 1995). Isoprene is more reactive towards three important atmospheric oxidants, $OH^{\cdot}$, NO^{3-} and O_3 (*Atkinson,* 1994, 1997). Recent field studies have revealed that isoprene dominates the day time photochemistry, in rural and remote regions from the tropics up to higher latitudes (*Biesenthal,* 1998). The greatest impact of isoprene on the atmosphere is observed through its oxidation products. Isoprene's first set of oxidation products include three distinct functional groups: the carbonyl, the hydroxycarbonyl and the hydroxy alkyl

nitrate. Each of these species has a different atmospheric impact upon ozone formation (*Henze,* 2006; *Lars,* 2000) and the OH radical depletion (*McKeen*, 1997). These species also affect chemistry of NO_x with the formation of alkyl nitrates (*Chen*, 1998).

Therefore, it is crucial to study oxidation mechanism of isoprene to understand the troposphere chemistry (*Donahue*, 2002).

1.2: OH-Radical initiated Oxidation of Isoprene

Isoprene decays from the atmosphere primarily by its reaction with OH radical (*Guenther*, 1995). It has been reported that at ambient temperature isoprene is oxidized by OH radical with rate constants in the range of $(0.9 \pm 0.26) \times 10^{-10}$ to $(1.1 \pm 0.23) \times 10^{-10}$ cm^3/s (*Woojin*, 2005). While, oxidation products of isoprene, for example methyl vinyl ketone and methacrolein, are oxidized by OH radical, with rate constants of 0.2×10^{-10} and 0.3×10^{-10} cm^3/s respectively, at same temperature.

The reaction of isoprene with OH radical takes place by $OH^{\cdot}$ addition to isoprene, in four distinct locations, at either end of its two double bonds (Campuzano, 2000). The four addition sites lead to the formation of four allylic radicals (see figure 1.1). According to recent estimates, in the case of 60% to 93% of the overall addition reactions, OH radical adds to the end carbons (allylic radicals a and b, from figure 1.1). The second step in the oxidation sequence is the addition of molecular oxygen to form a total of eight possible peroxy radicals (*Jenkin*, 1995; *Seinfeld*, 1992).

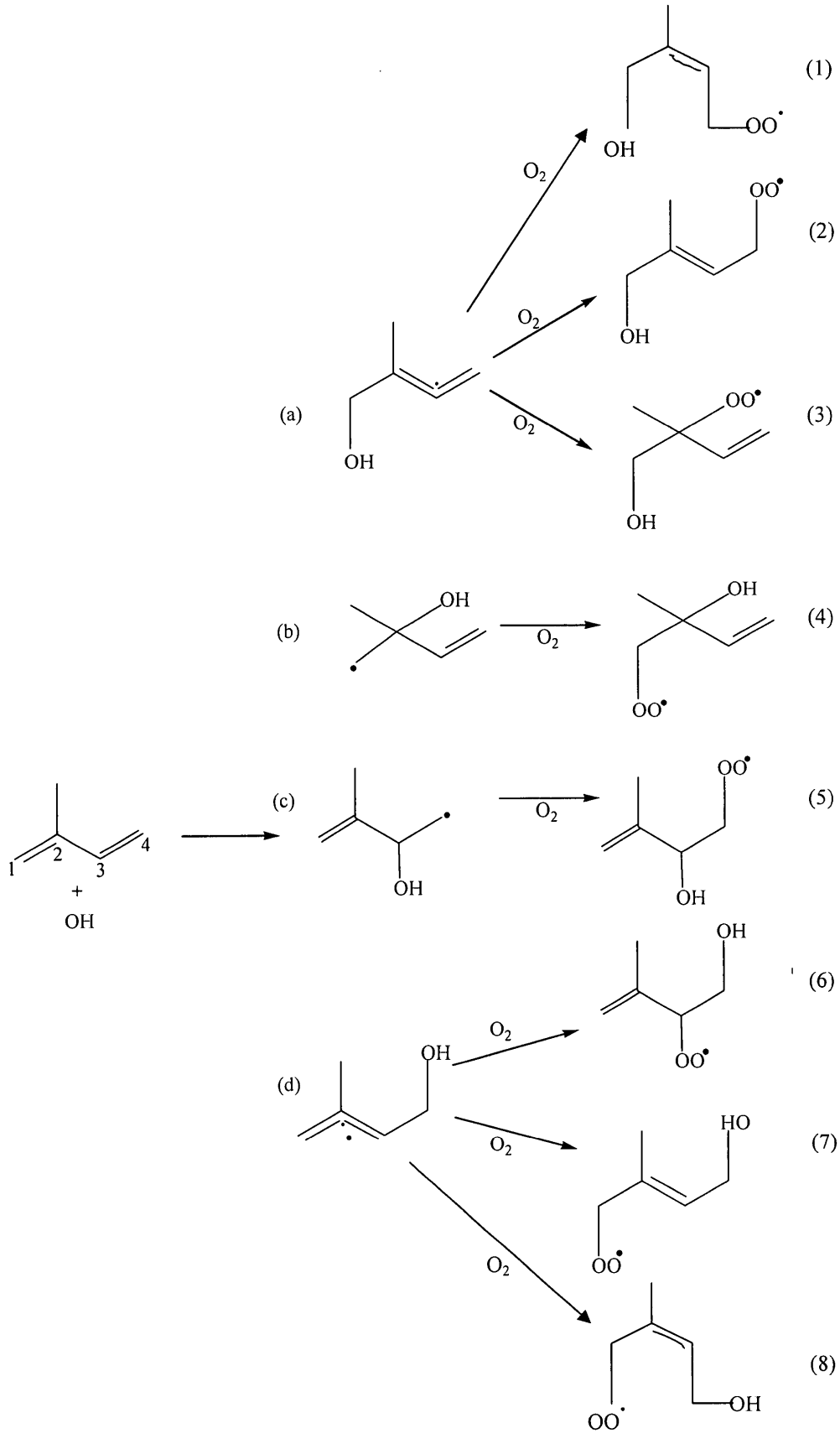

Figure 1.1: Formation of eight peroxy radicals from OH initiated oxidation of isoprene

In the presence of NO at higher concentrations, the first order oxidation products of isoprene are thought to include hydroxycarbonyl species, alkyl nitrates, methyl vinyl ketone (MVK), methacrolein (MAC), formaldehyde and 3-methyl furan (3MF) (*Atkinson*, 1989; *Tuazon*, 1990a; *Paulson*, 1992; *Miyoshi*, 1994; *Suzanne*, 1992; *Biesenthal*, 1997; *Lars*, 1999; *Jun*, 2003; *Woojin*, 2005; *Jesse*, 2006; *Paulot*, 2009; *Kourtchev*, 2005; *Richard*, 2006; *Magda*, 2006).

Different techniques have been used to study these oxidation products of isoprene, using OH radical as an oxidizing agent. For example, *Woojin et. al.* (2005), studied the OH radical initiated oxidation of isoprene in the absence of NO (nitrogen oxide), at a constant chamber temperature of 323 K. The system consisted of a quartz reaction chamber (~ 190 cm^3), stationed inside a gas chromatographic oven (HP 5890). The chamber was connected to an electron impact mass spectrometer (HP 5989A MS Engine) by a fused silica tube (75cm x 100μm). Helium was added to the chamber, to dilute the concentration of isoprene. OH radicals were produced by photolysis of hydrogen peroxide (H_2O_2) with 8-W UV lamps, at 254 nm, attached outside the door of GC oven. Radiation was maximized in the reaction chamber by lining the inside of GC oven with reflective tape. The percentage yields of three products were determined, namely methacrolein (19%), methyl vinyl ketone (14%) and 3-methyl furan (3%). The remaining products were identified as C_5-diols, C_5-carbonyl species, CO_2 and CO.

Jun et. al. (2003), used proton-transfer reaction mass spectrometric technique (PTR-MS) to study OH radical initiated oxidation of isoprene. The instrument consisted of a

discharge source of H_3O^+ ions, a high-pressure turbulent flow reactor and a quadrupole mass spectrometer. Proton transfer reactions between the volatile organic compounds (VOCs) and the hydronium ions (H_3O^+) took place in the reactor, a general reaction would be

$$R + H_3O^+ \rightarrow RH^+ + H_2O \qquad \text{reaction 1.1}$$

Converting the reagent (H_3O^+ ions) into the protonated product ions (RH^+) which were then detected by the mass spectrometer. The value of the proton-transfer reaction rate constant was known, which allowed quantification of products formed. The identified products were methacrolein, methyl vinyl ketone, 3-methyl furan, organic nitrates, C_4-hydroxycarbonyl, C_5-hydroxycarbonyl and C_5-carbonyl. The yields of MVK, MAC and 3MF were reported to be 29 to 36%, 21 to 25% and 4.4% respectively. In addition, the measured yields of alkyl nitrates ranged from 4% to 14%.

Benkelberg et. al. (2000), used gas chromatography-mass spectrometry (GC-MS) to study OH radical induced oxidation of isoprene in NO_x free condition. Reactions were carried out in glass bulbs of 2 L capacity, filled with hydrogen peroxide (the OH radical precursor) and 0.01 to 0.1% of isoprene (mole fraction in synthetic air). The interior walls of the bulbs were treated with dimethyl-dichlorosilane to minimize losses of hydroxycarbonyl compounds and diols. Each bulb was provided with teflon-stoppered shut-off valves, a silicone rubber septum and a quartz finger reaching into the center of the bulb, into which a mercury lamp was inserted. The reaction started with turning on the mercury lamp, which resulted in photolysis of H_2O_2 and production of OH radicals. Following irradiation, the bulb was connected to the sample loop of a gas

chromatography via a thin teflon tube pushed through a hole pierced in the septum. Samples were transferred by means of a suction pump and nitrogen carrier gas. The sample loop of the gas chromatography was heated to 160 ^{0}C. Product identification was made by comparison of peak retention times with those of reference samples commercially available. Products monitored were methyl vinyl ketone, methacrolein, 1-hydroxy-3-methylbut-3-en-2-one and 3-methyl-3-oxo-butane.

Hence, different techniques are used in published literature, to study OH initiated oxidation of isoprene. The focus of our research is to identify the products formed and their % yields.

1.3: Particulate Matter Formation from Isoprene Oxidation

Recent field studies (e.g. *Claeys*, 2004; *Edeny*, 2005; *Kleindienst*, 2007b) and laboratory studies (e.g. *Kroll*, 2005, 2006; *Kleindienst.*, 2006; *Ng*, 2008) have identified that isoprene oxidation contributes to the formation of atmospheric SOA (Secondary Organic Aerosols) formation.

SOA formation is influenced by several factors, such as NO_x concentration, $RO_2^{\cdot}$ (alkyl peroxide radicals) concentration, temperature, and heterogeneous reactions. Chamber studies revealed that SOA yields are 1-2% at high NOx levels and 3% at low NOx levels (*Kroll*, 2005, 2006). Overall contribution of isoprene to the total atmospheric particulate organic matter (POM) is ~ 9 Tg/yr.

Claeys et al. (2004a) provided the first evidence of secondary organic aerosol formation from isoprene. The study featured aerosol analysis from the Amazonian rain forest, by collecting filtered samples using GC-MS. 2-methylthreitol and 2-methylerythritol collectively known as 2-methyl tetrols were identified in atmospheric POM. 2-methyl tetrols have the same carbon skeleton as isoprene and subsequent studies performed in Amazonian rain forest (*Wang,* 2005), boreal forest in Finland (*Kourtchev*, 2005), forests in central Europe (*Ion,* 2005) and regions in United States (*Edney*, 2005; *Xia,* 2006; *Ding,* 2008) confirmed that 2-methyl tetrols exhibit similar trends to those of isoprene emissions, with abundances highest in daytime (e.g. *Plewka,* 2006) and summer (e.g. *Kleindienst,* 2007a). This strongly suggests that 2-methyl tetrols are formed from the oxidation of isoprene.

In addition, other polyhydroxylated compounds with the carbon skeleton of isoprene or methacrolein have been measured in atmospheric aerosol. These include C_5 alkene triols, methylglyceric acid, characterized by intense deforestation fires (*Ion,* 2005) and hemiacetal dimer from biogenic emissions (*Surratt,* 2006; *Carlton*, 2009). Thus isoprene is a potentially important SOA precursor.

1.4: Materials and Methods

A preliminary investigation of OH radical induced oxidation of isoprene was performed, resulting in the formation of its first-generation products, namely methacrolein (MAC) and methyl vinyl ketone (MVK). This experiment was carried out in a smog chamber at

room temperature and one atmosphere pressure. Products were analyzed by an ion-trap, time-of-flight mass spectrometer (IT-ToF MS).

Time-of-flight mass spectrometer is widely used to monitor gas phase reactions because ToF devices can rapidly measure an entire mass spectrum on every ionization pulse. This property of time-of-flight devices is particularly important in investigating fast chemical reactions such as for the oxidation of volatile organic compounds. Other advantage includes potentially high resolution that can be achieved with ToF devices.

A number of methods have been used, for example supersonic jet cooling (*Lubman*, 1985) or a reflectron (*T.Bergmann*, 1982), to achieve higher resolutions, using a variety of ionization sources including laser ionization and electron impact.

A major limitation of ToF devices is that there is no storage of ions in the acceleration region. Ion storage is particularly important in studies involving ion-molecule chemistry. Although there have been several attempts to store ions using dc fields, the ion storage time by this method is limited (*Boyle*, 1991). A better way of achieving ion storage is the combination of an ion-trap with a time of flight tube.

The ion-trap is a powerful tool for storage of ions over a wide mass range (*Paul*, 1990). The ion-trap has been used with several ionization sources including electron impact, chemical ionization and photo ionization which can create ions directly inside the trap. Here, chemical ionization was opted using O_2^+ ions, as chemical ionization reagents. The

radio frequency (*RF*) was also adjusted, for trapping of heavier masses inside the trap. Thus the performance of ion-trap, time-of-flight mass spectrometer was improved in terms of trapping of heavier masses and increasing of signal responses. The equipment was calibrated to determine the reliability (consistency) of the signal response.

Calibration spectra of isoprene and its oxidation products were generated, using a continuously stirred tank reactor (CSTR). The goal of generating these spectra was to determine the fragmentation pattern and to generate the alpha values of all the fragments belonging to any organic species.

Given that IPN (isopropyl nitrite) was used as an OH radical precursor during isoprene oxidation experiments, its calibration spectrum was also acquired. IPN was directly injected into the smog chamber (instead of the CSTR), because of its high volatility and unknown concentration.

During the isoprene oxidation reaction, the concentration of reactants and products were determined as a function of time and subsequently signal contributions were removed starting from reactants (isoprene and IPN), followed by the products (methacrolein and methyl vinyl ketone). Percentage yields of methacrolein and methyl vinyl ketone were also determined and the residual signals were reported for future reference.

1.5: Outline of Thesis

Chapter 2 gives a brief description of the instrument, followed by the experiments performed to optimize the operating conditions. Chapter 3 presents the instrumental calibration, along with calibration spectra of the reactants and products of isoprene oxidation. Chapter 4 provides a detailed account of the isoprene oxidation reaction. Then a summary of conclusions is provided in chapter 5. Chapter 6 contains a list of all the refrences quoted in this thesis. Finally an appendix provided at the end demonstrates total and residual ion counts from the isoprene oxidation experiment (chapter 4).

Chapter 2: Instrumentation

2.1: Instrumental Overview

An ion trap time-of-flight mass spectrometer is used for analysis, with all components purchased from Jordon ToF Products, Inc. It consists of a source chamber and a flight tube. The main portion of this source chamber is a quadrupole ion trap. Chemical ionization and ion storage occur inside the ion-trap, while mass analysis is performed by a time-of-flight (ToF) device. Figures 2.1 to 2.8, provided in this chapter, are courtesy of *March and Todd*, quadrupole ion trap mass spectrometry, 2nd edition, 2005.

2.2: Quadrupole Ion-Trap Storage Device

Electrodes

As a storage device, the ion trap is used for confinement of positively charged gaseous ions. This confining capacity arises from the formation of a trapping potential well, when appropriate potentials are applied to the electrodes of the ion trap. The confinement of gaseous ions permits the study of gas-phase ion chemistry and elucidation of ion structures (*March et al.*, 1997).

A quadrupole ion trap consists of three electrodes. Two of the three electrodes are virtually identical, and, while having hyperboloid geometry, resemble small inverted saucers. These saucers are called end-cap electrodes (*Jonscher et al.*, 1997).

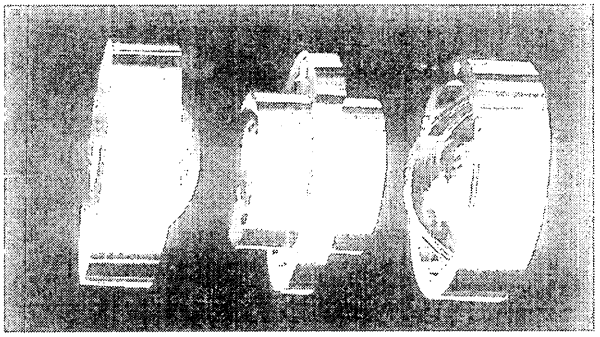

Figure 2.1: Ion-trap electrode assembly (*March*, 2005)

One end-cap electrode has a single small central aperture through which ions can be gated periodically into the ion trap. It is called the entrance end-cap. The other electrode is called the exit end-cap electrode. It has several small apertures arranged circularly through which ions are ejected into the flight tube. The third electrode is called the ring electrode, positioned symmetrically between the two end-cap electrodes.

Figure 2.2 shows cross-section of an ideal ion trap showing dimensions r_0 and z_0, wherein r_0 is the radius of the ring electrode in the central horizontal plane and $2z_0$ is the separation of the two end-cap electrodes measured along the axis of the ion trap (*March,* 1997).

Geometries of the electrodes are defined, so as to produce an ideal quadrupole field, which also produces a parabolic potential well for confinement of ions. The potential well is created from the field that exists when an *RF* potential is applied to the ring electrode and the two end-cap electrodes are grounded.

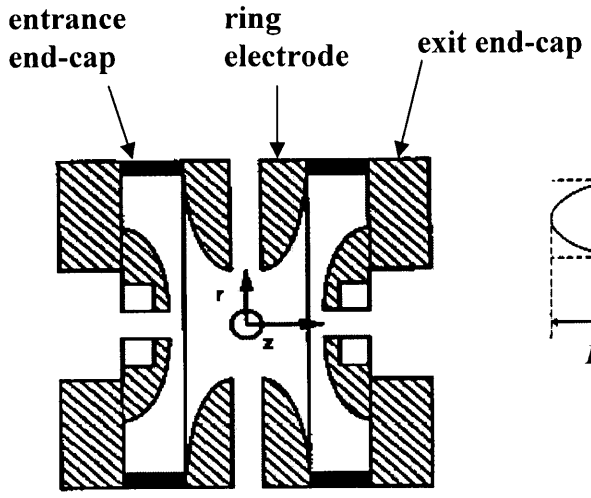

Figure 2.2: Cross-section top view (*March*, 2005)

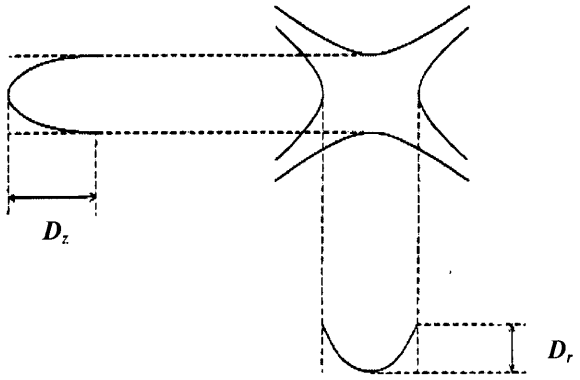

Figure 2.3: The parabolic potential well (*March*, 2005)

The potential well in the axial direction is of depth D_z, whereas in the radial direction, the depth is D_r. Value of D_z is about twice to that of D_r. For an ideal quadrupole field,

$$r_0^2 = 2 z_0^2 \qquad \text{Equation 2.1}$$

$$D_z = 2D_r \qquad \text{Equation 2.2}$$

Once the magnitude of r_0 is given, the sizes of all three electrodes and the electrode spacing are fixed.

Ion Trap Operation and Mathieu Equation

An ion in a quadrupole field experiences a strong restoring force, which drives the ion back towards the centre of device and increases as the ion deviates from the centre. A population of trapped ions is therefore observed to occupy only the space near the center of the trap due to the focusing effect of oscillating electric fields. The motion of ions in a

quadrupole field can be described mathematically by solutions to the second order linear differential equation, known as the Mathieu equation (equation 2.3).

$$(d^2u / d\zeta^2) + (a_u - 2q_u cos2\zeta)\, u = 0 \qquad \text{Equation 2.3}$$

Wherein u represents the coordinate axes x, y and z, ζ is a dimensionless parameter equal to $\Omega t/2$, Ω is the frequency, t is the time and a_u and q_u are additional dimensionless parameters known as trapping parameters.

Mathieu investigated the mathematics of vibrating stretched skins. He described solutions in terms of regions of stability and instability. These solutions and the ideas of stability and instability were applied to describe trajectories of ions confined in the quadrupole devices (*March*, 1997).

Mathieu used these dimensionless parameters, a_u and q_u to describe stability regions in a_u and q_u space and to explain confinement and limits of gaseous ions in the quadrupole devices. Mathieu's equation was further solved for a_z and q_z trapping parameters, (equation 2.4 (a) and (b)):

$$a_z = (-8eU) / (mr_0^2\Omega^2) \qquad \text{Equation 2.4 (a)}$$

$$q_z = (8eV/m)\,(r_0^2 + 2z_0^2)\Omega^2 \qquad \text{Equation 2.4 (b)}$$

Wherein a_z is proportional to the DC potential of the electrodes. Thus a_z is usually equal to zero, such that the most common mode of ion trap operation is said to correspond to

operation along the q_z axis. The expression for q_z contains mass-to-charge (m/e) ratio for a given ion, size of the ion trap (r_0 and z_0), amplitude (V) of the RF potential and radial frequency (Ω). Solutions to the Mathieu equation can be interpreted in terms of trajectory stability (and instability) in each of the x, y (or r) and z directions (*Jodie,* 1992).

Regions of Ion Trajectory Stability

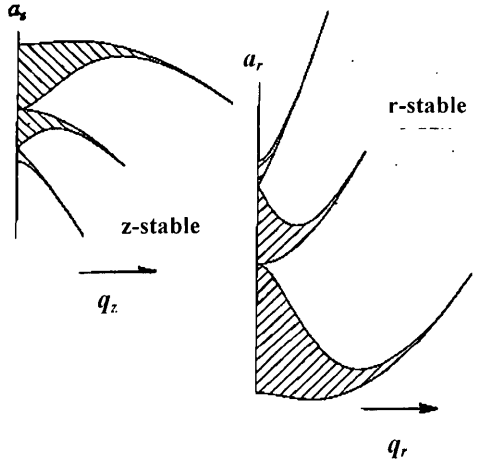

Figure 2.4: Mathieu stability regions for the three dimensional quadrupole field in a_z, q_z space (*March*, 2005)

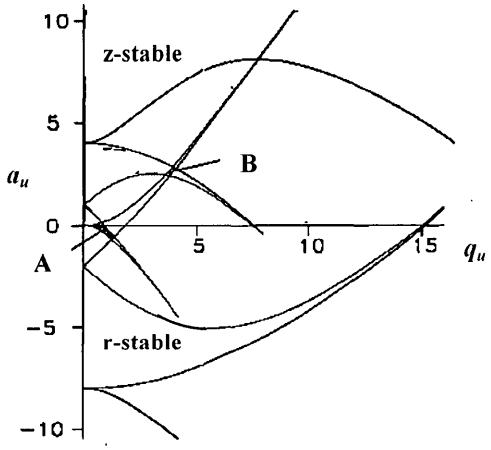

Figure 2.5: Stability regions A and B in center of the ion-trap (*March*, 2005)

In figure 2.4, stability regions corresponding to the stable solutions of the Mathieu's equation in the z direction are hatched and labeled as z-stable. Stability regions corresponding to stable solutions of the Mathieu's equation in r direction are shaded and labeled as r-stable. It is evident from figure 2.4 that the latter relative to the former are doubled in magnitude along the coordinates and inverted. These two stability regions overlap, as shown in figure 2.5. Ions can be stored in the ion trap provided their trajectories are stable in the r- and z-directions simultaneously. Such trajectory stability is

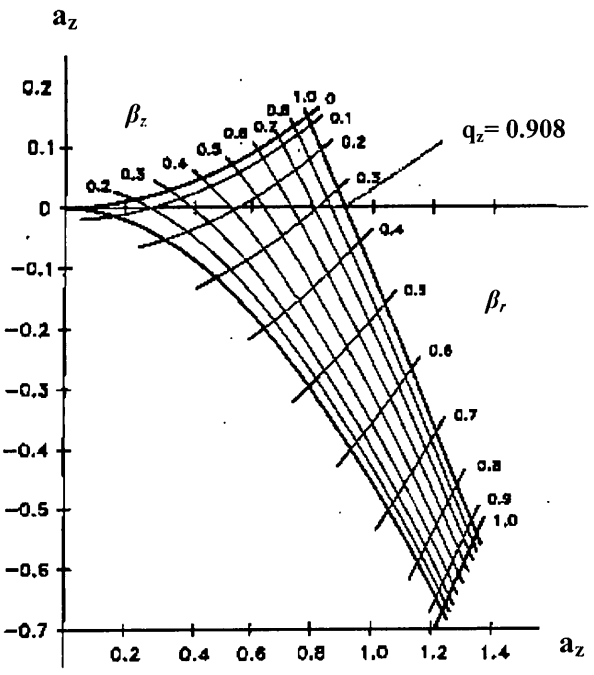

Figure 2.6: Stability region A inside the ion-trap (*March*, 2005)

obtained in the region closest to origin that is region A. Its expanded version is provided in figure 2.6, where a_u is plotted against q_u. Regions A and B are referred to as the stability regions. Region A is of the greatest importance at this time. As shown in figure 2.6, β_z =1 is the stability boundary that intersects with q_z axis at q_z = 0.908. This is the working point of the ion with lowest mass-to-charge ratio, that is, lower mass limit (LML) that can be stored in the ion trap. The trajectories of trapped ions become unstable, axially, such that ions with mass-to-charge ratio less than the LML cannot be stored (*March and Todd,* 2005).

Secular Frequencies

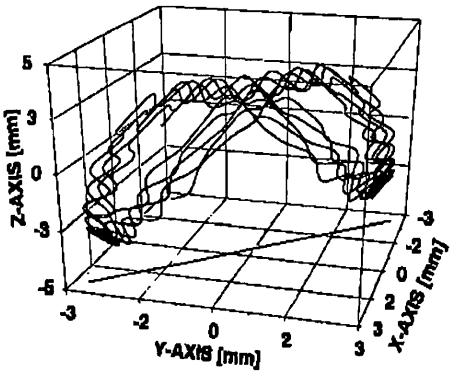

Figure 2.7: Trajectory of a trapped ion (m/z 105)

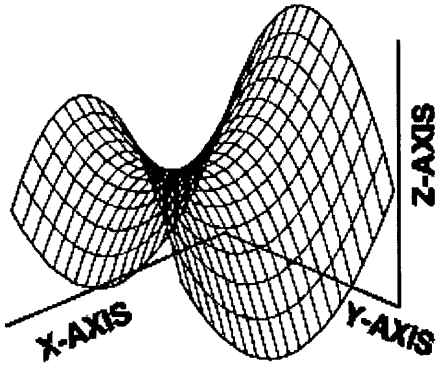

Figure 2.8: Pure quadrupole field or potential surface for a quadrupole ion trap

Figure 2.7 presents a projection of ionic motion, in three-dimensional space. The three-dimensional ion trajectory has the general appearance of a lissajous curve, composed of two fundamental frequency components, $\omega_{r,0}$ and $\omega_{z,0}$, of the secular motion.

Fundamental axial secular frequency $\omega_{z,0}$, is usually given in the units of hertz in literature and is referred to as ω_z. Resemblance of the simulated ion trajectory shown in figure 2.8 to a roller-coaster ride is due to the motion of an ion on the potential surface (*March,* 1997).

2.3: Instrumental Description

The instrument is divided into two sections, the source chamber and the flight tube.

2.3.1: Source Chamber

This is the first section of the instrument where ions are produced and stored prior to injection into the flight tube. It has an electron gun to produce primary electrons that ionize the oxygen molecules. The chamber also has a quadrupole ion-trap to store ions prior to injection into the flight tube, a leak valve to admit the sample gas and is vacuum enclosed. The vacuum is generated by a 550 L/s turbo molecular pump (Turbo550). The pressure inside the chamber is measured by means of an ion gauge. Figure 2.9 shows the schematic diagram of the source chamber.

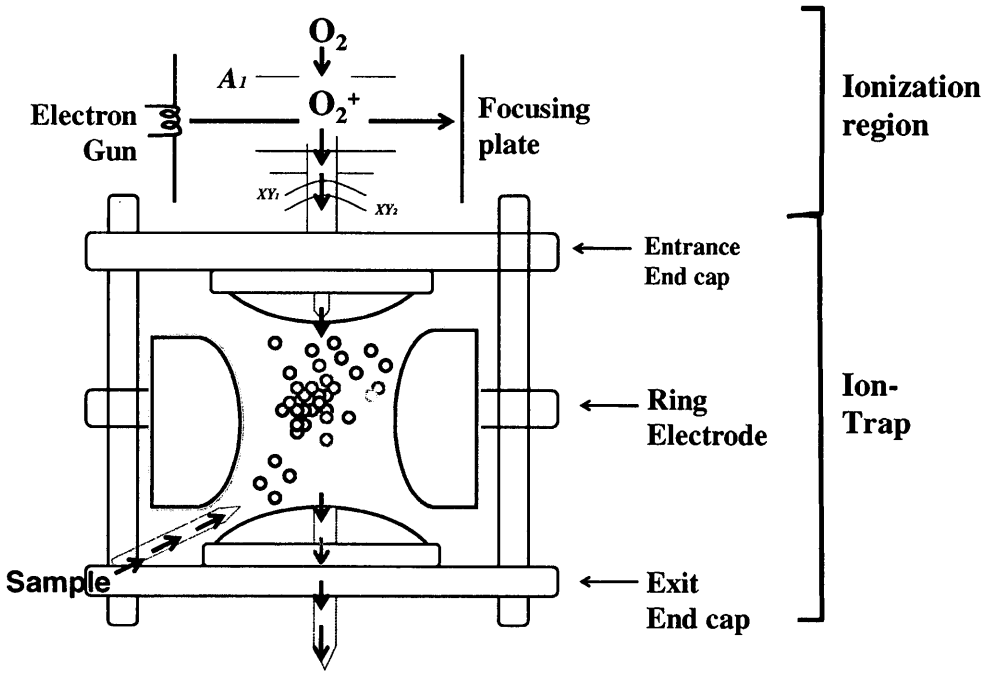

Figure 2.9: The source chamber

As shown in figure 2.9, ionization of oxygen gas is accomplished by electron impact ionization. An electron gun is aimed into the region above the ion trap, which emits primary electrons. A potential of 70 V is maintained between the filament and the focusing plate. The focusing plate directs these energetic electrons into collision with the air molecules. Impact with these primary electrons e^-_p promotes ground state O_2 molecules to excited state O_2^+ ions. The O_2^+ ions are the chemical ionization reagent.

2.3.2: Ion-trap

Gating of these O_2^+ ions into the trap is controlled by a high voltage pulse generator. The triggering process is explained in section 2.3.3. When ions are being gated into the ion-trap, A_1 (shown in figure 2.9) acts as a repeller plate and is set at +110 V. Deflectors and

Split lenses (XY_1 and XY_2) are set at negative potentials, to direct O_2^+ ions into the ion-trap.

A sample (for example hydrocarbons) enters into the trap by an inlet at the ring electrode (*Randall,* 2002). High pressure and collision of O_2^+ ions with the sample results in fragmentation of this sample. The pattern of fragmentation is dependent on the composition of the parent ion. Fragmentation and rearrangement have been observed inside the trap, producing positive ions that are relatively stable (*Michael,* 1992). These positive ions are stored in the form of an ion-packet in center of the trap, where their trajectories are stable.

Finally, when storage time ends, this ion-packet is accelerated using a DC voltage on the exit end cap of the trap to enter the flight tube.

2.3.3:Time of Flight (ToF) Tube

The second portion of the equipment is a time-of-flight (ToF) tube. A mass spectrum is obtained by measuring the time required for ions to travel down this flight tube. Ions enter the ToF tube via a 0.5-inch diameter orifice. Steering plates are added inside to counteract any spread in initial velocity of ions, from the axis of the ToF tube. A liner is used to create a uniform potential so that the drift tube is field-free. Pumping is also required to prevent ions from colliding with other molecules on their way to the detector

(*O'Hanlon,* 2003). Therefore, the flight tube is evacuated by a 250 L/s turbo molecular pump with pressure inside the flight tube approximately $\approx 10^{-4}$ Pa.

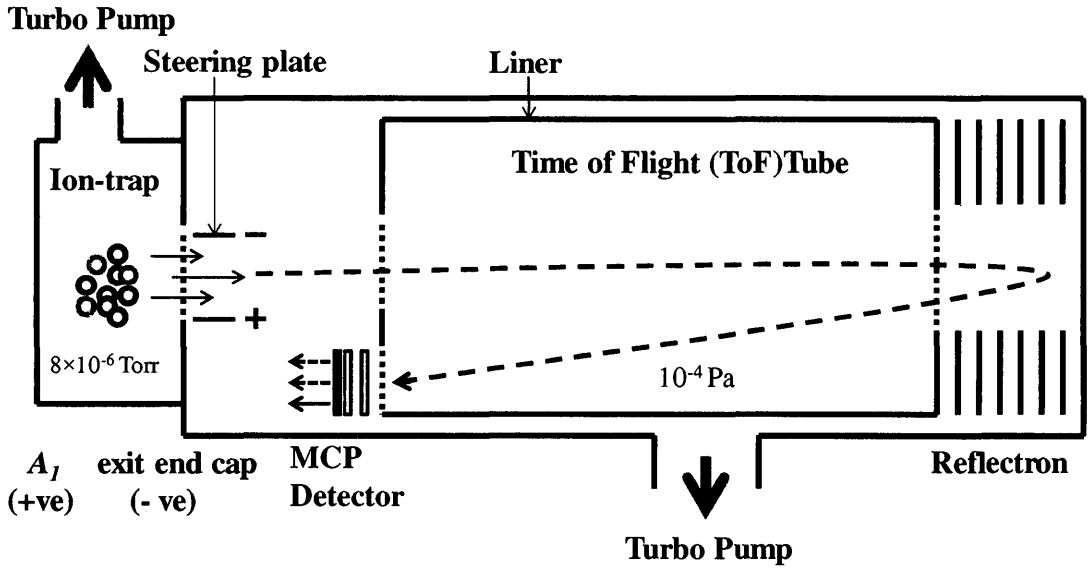

Figure 2.10: Schematic diagram of the ion-trap, time of flight mass spectrometer

The flight tube is equipped with a reflectron (or ion mirror) that extends the focal plane. After traversing the flight tube, ions enter a retarding field, defined by a series of grids, and are turned around and sent back through the flight tube. The principle of the reflectron is that an ion with higher energy will penetrate the retarding field more deeply and will require more time turning around, subsequently catching up with a slower ion. Consequently, ions with different masses are reflected from the reflectron and roughly hit the detector simultaneously.

The flight time is provided by equation 2.5 (*Cotter,* 1997) wherein t is the flight time over

a path of length L for an ion with a molar mass-to-charge ratio Mz, accelerated through a potential of V volts.

$$t = L \sqrt{(M_z/2F\,V)} \qquad \text{Equation 2.5}$$

where F is the Faraday's constant (9.648×10^4 C/mol), and V is the amplitude of the RF potential. The detector is a dual microchannel plate (MCP). It is designed to handle the fast ion pulses provided by the time of flight mass spectrometer. It provides high gain (10^6 to 10^7) with sub-nanosecond rise time.

2.3.4: Timing and triggering

It is important to explain the timing and triggering process, as it was adjusted to optimize the mass range. Measurements are recorded in a repetitive cycle, with successive measurements being averaged and stored by the computer. Each measurement begins by admitting ions into the ion-trap for certain period of time. The example of timing sequence is provided in figure 2.11. Gate pulses are separated by 100 milliseconds, with the width of the gate pulse determining the gate open time. In figure 2.11, the gate pulse width is adjusted at 95 milliseconds, meaning ions would enter into the trap for 95 milliseconds. Almost all chemical ionization occurs during this time. After 95 milliseconds, the gate pulse shuts off and the storage time begins. The duration of storage time is 4 milliseconds in figure 2.11. During the storage time O_2^+ decays rapidly. At the end of the storage time, the ion-trap RF field is shut off and an extraction pulse is sent to the exit end cap electrode to inject the ions into the flight tube; data acquisition begins at the same time. Acquisition of the ToF mass spectrum is performed by a Perkins-Elmer 9846 transient recorder mounted in the computer. This recorder can acquire data at 500

megahertz with 8-bits resolution. The external trigger signal, mentioned earlier, initiates data acquisition. This data is then transferred to the computer, where successive spectra are averaged.

When data acquisition is complete, the extraction pulse is shut off and the *RF* field is turned back on. Repetition of this cycle is controlled by pulses from a Hewlett-Packard function generator, with a typical pulse rate of 10-Hz. This trigger pulse from function generator provides trigger input to the ion trap power supply. The ungated trigger pulses are shown as dashed lines in figure 2.11.

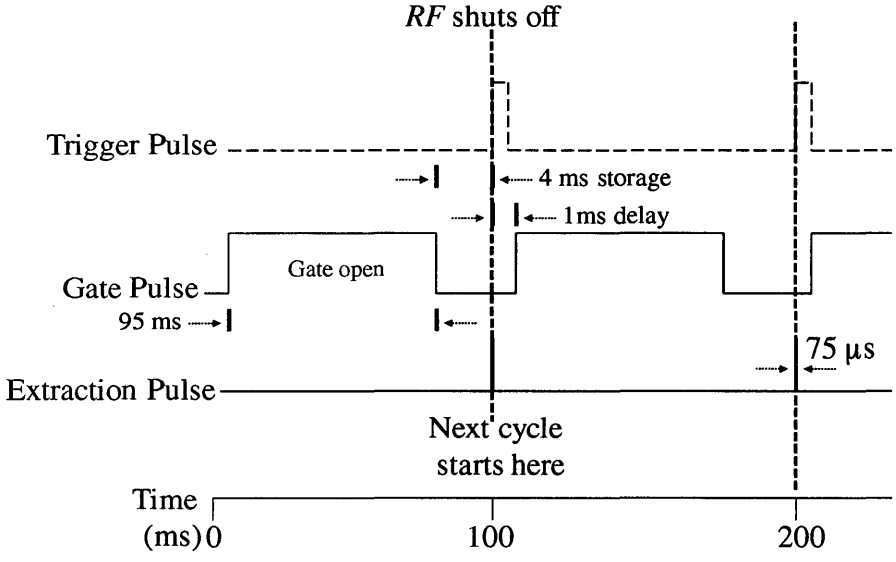

Figure 2.11: Outline of timing and triggering events

When *RF* shuts off, the ion trap power supply sends a trigger pulse to a Digital Delay Generator (DDG) and the data acquisition board. In turn, the DDG controls the extraction pulse from the ion-trap and gating of ions into the ion-trap. When shut off, the extraction pulse creates noise and baseline shifts in the ToF spectrum.

To prevent this from happening, it is kept at 75 microseconds, since its longer than the longest ion flight time recorded. The gate pulse has a delay of one millisecond to allow ion-trap *RF* to be fully restored. Vertical blue dashed lines in figure 2.11 represent one full cycle.

Error estimates in data provided in this thesis, were generated by IGOR, based on consistency of the baseline, sensitivity setting, baseline noise and height of the peaks in the spectra.

2.4: Optimizing Operating Conditions

Operating conditions of the mass spectrometer was optimized using β-pinene, a monoterpene consisting of two isoprene units, with molecular formula $C_{10}H_{16}$. It's molar mass is 136.23 g/mol and density is 0.87 g/mol. It was used for its wide range of fragmentation.

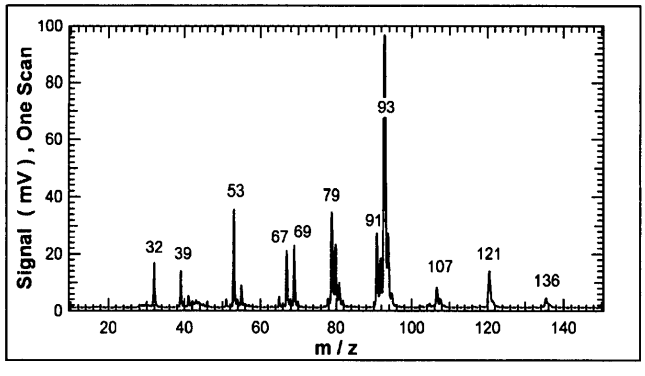

Figure 2.12: Mass Spectrum of β-pinene

As shown in figure 2.12, ions from m/z 39 to 136 were all β-pinene fragments. Four experiments were performed to optimize operating conditions and to enhance the overall signal response, using β-pinene. They are explained in details as follows.

2.4.1: Adjusting Mass Range

The first experiment was to adjust the mass range. It was found that changing the *RF* amplitude varied the mass-to-charge (m/z) range of ions that were stable within the trap. Thus *RF* potential was readjusted and its impact on various masses was observed. *RF* was converted into lower mass limit (LML), using equation 2.6 (*March 2nd ed.*, 2005):

$$\mathbf{LML} = [FV] / [0.908\, z_0^2\, (2\pi f_{RF})^2] \qquad \text{Equation 2.6}$$

$$= (0.0538 \text{ g /mol. volt})\, V$$

Where F is the Faraday's constant (9.648×10^4 coul/mol), V is the peak-to-peak *RF* amplitude, z_0 is the trap dimension equal to 0.707 cm and f_{RF} is the *RF* frequency equal to 1.0 MHz. The lower stability limit of trap corresponds to $q_z = 0.908$. Different β-pinene fragments were then plotted against lower mass limit, as shown in figure 2.13.

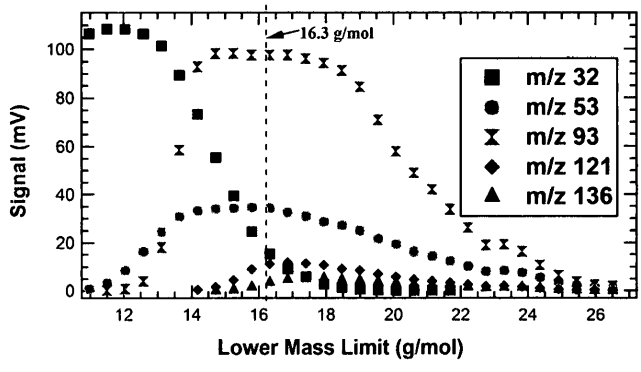

Figure 2.13: Variation in signal response with changing lower mass limit

Data was collected after every one minute at chamber pressure of 8×10^{-6} torr. The goal was to select an appropriate *RF* amplitude that would result in trapping of higher masses without compromising the O_2^+ signal inside the ion-trap. It was found that lower mass limit of 15.5 to 17.0 g/mol was an optimum condition. Before this range, heavier masses were being lost, and after this range, lighter masses were disappearing. For future work, it was decided to operate the mass spectrometer at LML of 16.3 g/mol.

2.4.2: Variation in Gate Open Time

Ions are gated into the trap for a certain period of time, determined by the width of the gate pulse. Once the gate pulse shuts off, the storage time begins and no more ions can enter into the trap. Chemical ionization takes place, resulting in consumption of O_2^+ ions. In this experiment, the width of the gate pulse was varied and observations were plotted in figure 2.14. Here lines with markers are used to highlight the few data points incorporated into analysis.

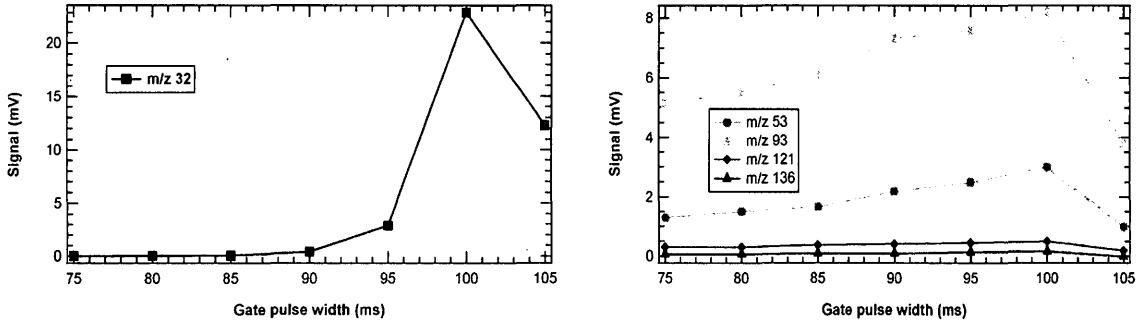

Figure 2.14: Variation of signal response with change in gate open time

Figure 2.14 showed that the highest signal was obtained at maximum time allowed for entrance of ions into the ion-trap and minimum time allowed for their storage. For future work, width of this gate pulse should be kept at 95 milliseconds.

2.4.3: Electron Gun Current Adjustment

Electron gun current is controlled by the ion-trap power supply. It corresponds to the extent of electron ionization taking place in the ionization region. Thus, increasing the electron gun current should increase the O_2^+ production. With more O_2^+ ions, chemical ionization should increase, resulting the increase of overall signal.

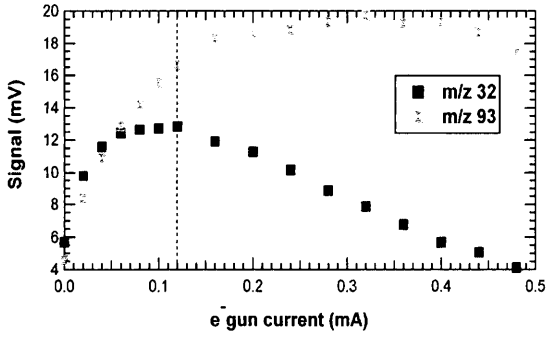

Figure 2.15: Variation in m/z 32 with changing e^- gun current

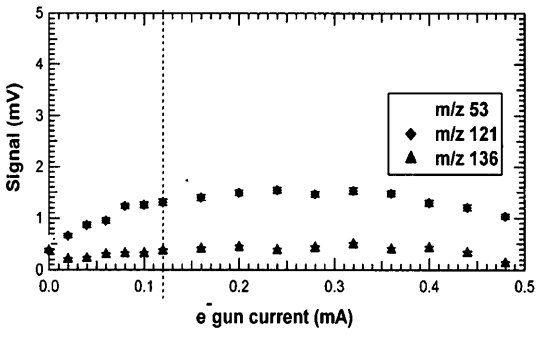

Figure 2.16: Signal variation of β-pinene fragments with changing e^- gun current

However, figure 2.15 revealed that m/z 32 went down after 0.12 milliampere, followed by analytic fragments (m/z 53, 93, 121 and 136), after 0.3 milliampere (figure 2.16). It is possible that O_2^+ was reacting more efficiently with an increased electron gun current and decaying faster.

2.4.4: Steady State Experiment

Time scale for the width of gate pulse is from 0 to 100 milliseconds, and then the next cycle begins. The highest signal was observed at 100 milliseconds (figure 2.14), that is, when no time was allowed for storage of ions. Therefore, an experiment was performed allowing ions to enter into the trap continuously, instead of being gated periodically. This condition is called steady state.

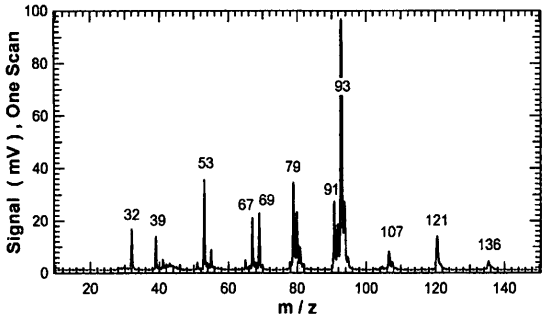

Figure 2.17: Signal response at Gate-able Condition

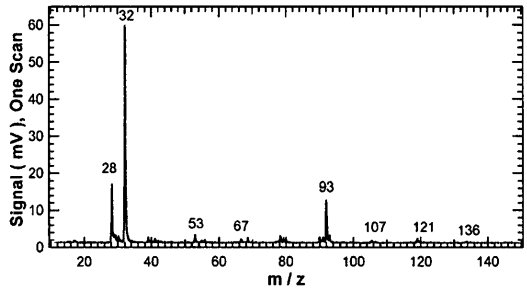

Figure 2.18: Signal response at Steady State

Higher signals were expected at steady state. Signal at m/z 32 (O_2^+ ions) was high, but the analyte sample was compromised (see figure 2.18). Smaller masses were perhaps moving faster than heavier masses and were blinding the detector. Thus, signal at m/z 32 needed to be decreased, as compared to the sample fragments. *RF* potential and electron gun current was readjusted for this purpose. However, both proved ineffective.

2.4.5: Trapping Potential at Steady State

During this experiment, gates were opened permanently at the entrance end-cap electrode and the lower mass limit was changed from 14 to 26 g/mol.

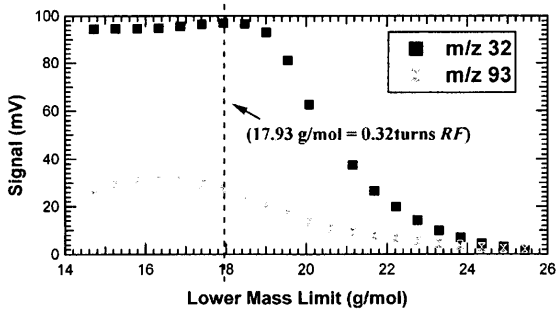

Figure 2.19: Response of m/z 32 to changing of LML at steady state

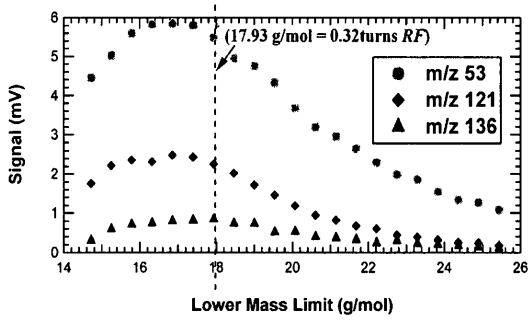

Figure 2.20: Response of β-pinene fragments to changing of LML at steady state

Maximum signal was observed around 17.9 g/mol, followed by loss in intensity for m/z 32 and the sample fragments.

2.4.6: Electron Gun Current adjustment at Steady State

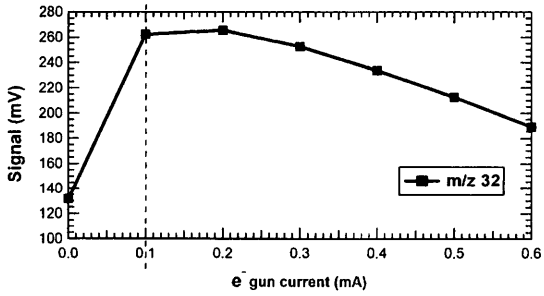

Figure 2.21: Response of m/z 32 to changing of electron gun current at steady state

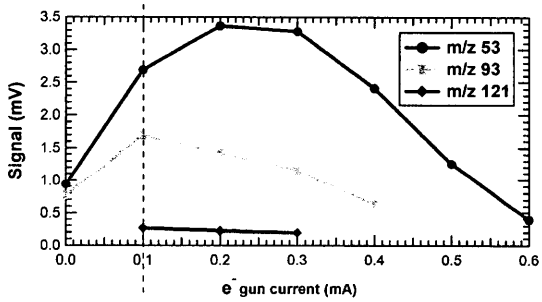

Figure 2.22: Response of β-pinene fragments to changing of electron gun current at steady state

Increasing electron gun current would increase production of primary electrons in collision with the ground state oxygen molecules, thus increasing production of O_2^+ ions (m/z 32). Since m/z 32 had higher signal as compared to sample fragments, electron gun current was lowered to see its effect on signal response of sample fragments. However, reagent and sample fragments responded almost similar to the changing of electron gun current, as shown in figures 2.21 and 2.22. Few points were incorporated in analysis, so lines with makers are used to present the results more clearly. The molecular ion peak at m/z 136 was also not observed during this experiment.

Expectation for readjusting the lower mass limit (LML) and electron gun current was that the signal of heavier masses would be increased and response from lighter masses would

be lowered. However, lighter and heavier masses showed similar responses in both experiments.

There was a need to remove excess of O_2^+ ions from the ion-trap. Therefore resonance ejection of O_2^+ ions was carried out as a next step. This would enable us to see the sample fragments, in preparation of ToF-MS experiments.

2.4.7: Resonant Ejection

Resonant ejection is used for selective ejection of ions from the ion-trap. During this technique a small auxiliary potential is applied across the end cap electrodes, at a particular frequency, in resonance to the secular frequency of the target ion. This results in increasing the amplitude of axial motion leading to the ejection of ions from the trap. Resonance ejection would improve performance by reducing space charge effects and would protect the detector from an excess of ion flux.

A waveform generator was used for resonance excitation to eject excess O_2^+ ions, prior to injection into the flight tube. This waveform generator was a multifunction sweep synthesizer, which produced sine waves, with a limit maximum of 200 kilohertz frequency and amplitude from 0-1000 millivolts. The pulse would arrive shortly before end of the scan, for a period of $\approx$ 4 milliseconds (which is the storage time). Frequency of this pulse was adjusted to resonate with the secular frequency of the O_2^+ ions. A rough

estimate was obtained by calculating the expected resonance frequency value calculated from equation 2.7.

An oscillating potential is generated by fundamental radio frequency *RF*, applied to the ring electrode. This oscillating potential forces the ions in the form of ion packets towards the center of the trap. An ion will be stably trapped depending upon the values for the mass and charge of that ion, the size of the ion-trap (r_0 and z_0), and the amplitude of the voltage on the ring electrode (V). The dependence of ion motion on these parameters is described by the dimensionless parameter q_z, calculated from equation 2.4(b) (*March*, 1997).

During resonance ejection, AC voltage was applied to the end cap electrode and the q_z value of O_2^+ ions was changed until the axial secular frequency of O_2^+ ions matched the frequency of the applied AC voltage. In theory, when resonance would occur, the amplitudes of O_2^+ ion trajectories would linearly increase with time. A high-amplitude AC voltage will cause resonance ejection and the frequency at which this resonance ejection would take place will be called the resonance frequency (ν).

$$\nu = [q_z f_{RF}] / [2 \sqrt{(2 - q_z^2)}] \qquad \text{Equation 2.7 (March, 2nd ed. 2005)}$$

For O_2^+ ions, the calculated value of resonance frequency was determined to be 184 kilohertz. Axial secular frequency was varied around the calculated value at steady state, to find the exact resonance ejection frequency, which when applied to end-cap electrode would excite and eject O_2^+ ions from the ion-trap.

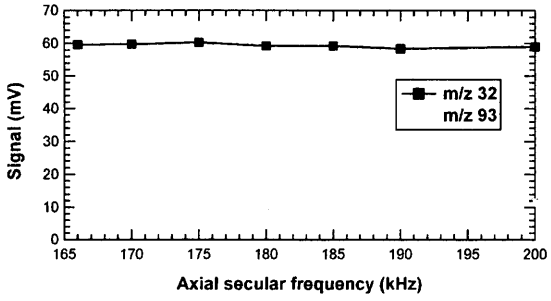

Figure 2.23: Showing resonant excitation of O_2^+ was not observed

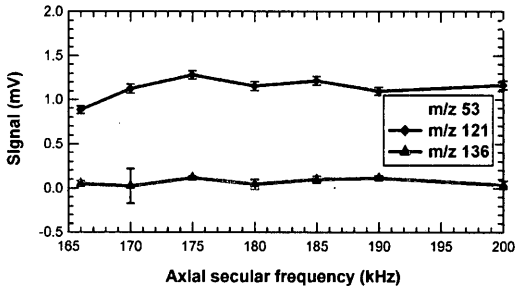

Figure 2.24: Showing slight increase in signal response for heavier masses at 175 kHz

However, resonance frequency could not be achieved, where oxygen was ejected out of the trap and its signal intensity decreased. Lighter ions have higher secular frequencies. The ejection frequency may have been more than 200 kilohertz and the waveform generator could not produce a frequency wave higher than that.

2.5: The Smog Chamber

A diagram of smog chamber is provided in figure 2.25. This chamber is an $8m^3$ flexible bag, made of 125 mm thick Teflon, operated at atmospheric pressure and room temperature. The bag is suspended in wooden enclosure. Two inlets and one outlet made of stainless steel and Teflon, allow easy installation of additional inputs and sampling lines. Two exhaust lines are also provided.

One inlet is for liquid hydrocarbon (isoprene or IPN), flushed with 10-15 mL/min of purified air into the chamber. This purified air is supplied by an AADCO (737-250 series, AADCO Instruments, Inc., USA) pure air generation system. The second inlet is used for

nitrogen dioxide (NO) injection, which is admitted into the smog chamber through a mass flow controller (MFC).

Between each experiment, the chamber is continually flushed through the exhaust lines with purified air, resulting in low background contamination, which allows for high quality data at low concentrations. Twelve pairs of UV tube lights are directed along the Teflon bag wall to photochemically generate OH radicals. These ultraviolet lights have a wavelength of 350-400 nm (Philips F40BL, 40 Watt) and smog chamber can be operated with 2 to 24 UV lights and at various NO flow rates.

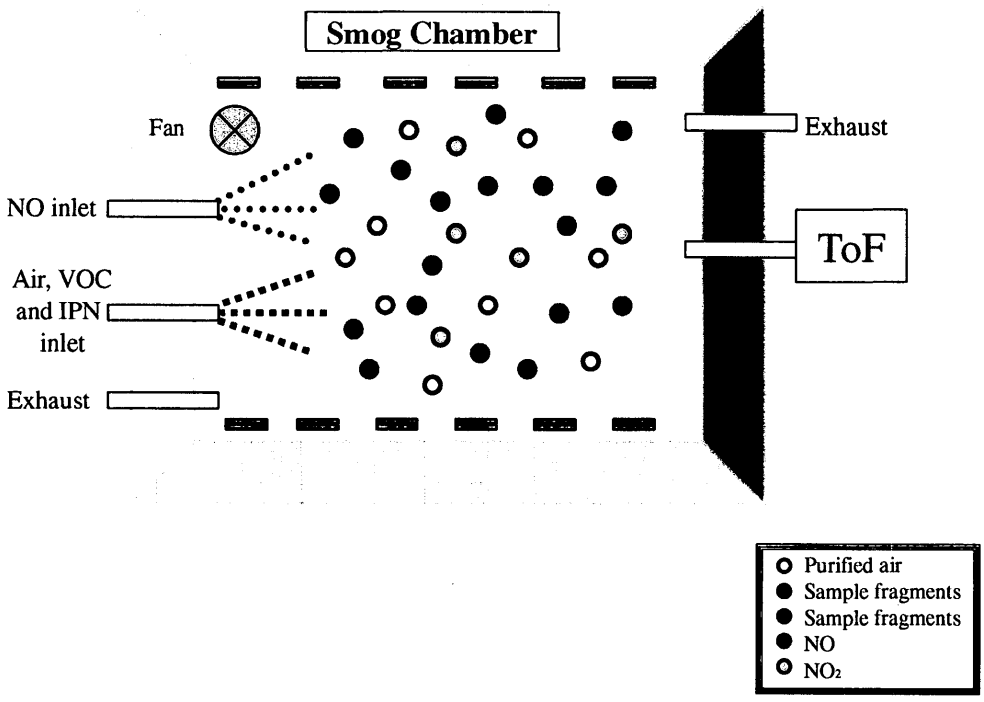

Figure 2.25: Apparatus sketch for Smog chamber experiments (IPN photolysis and isoprene oxidation)

Smog chamber experiments included the following steps:

1. Flushing chamber with clean air, at a flow rate of 20 L/min, for at least 24 hours before each experiment, then exhaust lines are closed.
2. Input of nitrogen oxide gas.
3. Input of volatile organic compounds.
4. Allowing this mixture to mix for one hour and ten minutes, before lights are turned back on.

Chapter 3: Instrumental Calibration

3.1: Introduction

The concept of CSTR calibration spectra is provided in this chapter. The goals of calibration spectra were to determine the fragmentation patterns of reactant and products of isoprene oxidation, to determine the sensitivity of the mass spectrometer and to check for linear behavior over a wide range of concentrations, so as to make sure that there were no secondary chemistry or saturation effects or to characterize them if there were any.

A three-necked round bottom flask, named the Continuously Stirred Tank Reactor (CSTR), was used to perform calibration experiments for organic compounds that were suspected to be present in OH-radical initiated oxidation of isoprene. Calibration spectra were generated for isoprene and its products methyl vinyl ketone (MVK) and methacrolein (MAC). Calibration spectra were also generated for isopropyl nitrite (IPN) and its degradation product acetone. IPN was prepared in the laboratory and its concentration was unknown. Therefore its direct calibration was not possible and it was injected into the smog chamber, instead of the CSTR.

Linear correlation analysis was also studied to check for secondary ion formation. Hypothetically, if any fragment had a good linear relation with the most stable fragment, then both were generated at the same time and were primary fragments. A secondary fragment would not show a linear correlation to the most stable ion. The slope of each

linearly correlated line would later be compared with the slope values obtained during linear correlation analysis, in the isoprene oxidation experiment. Based on fit quality, similar slope values would mean similar alpha values. However, the first step was to determine if the signal coming from mass spectrometer was reliable (consistent) or not.

3.2: Calibration of Ion-Trap, Time of Flight Mass Spectrometer (IT-ToF MS)

Procedure

To keep track of its sensitivity, the mass spectrometer was calibrated using a syringe pump. Toluene was used as a reference material, injected by a syringe of 1 μL capacity. Calibrated gas flows were drawn into the instrument via mass flow controllers, which made it easy to calculate moles of air at all times; using equation 3.1. The moles of toluene injected could also be calculated by equation 3.2. Volume in equation 3.2 is the amount of toluene being injected, in micro liters per hour. When moles of air and moles of toluene were known, the mixing ratio of toluene in air could also be determined, using equation 3.3. Thus, carefully selecting different syringe flows and gas flows, covering all possible ranges, a measured flow was injected into the ToF.

$$n = PV / RT \qquad \text{Equation 3.1}$$

$$\textbf{Moles of toluene} = \textbf{Density} \times \textbf{volume} / \textbf{Mol. Wt.} \qquad \text{Equation 3.2}$$

$$\textbf{Mixing ratio of toluene in air} = \textbf{Moles of toluene} / \textbf{Moles of air} \qquad \text{Equation 3.3}$$

The time response was very slow (see figure 3.1). It was suspected that the droplet formed at the tip of the syringe might be taking longer time to build up and it needed to be checked. First, the radius (a) of this droplet was calculated using equation 3.4.

$$\Phi = 4\pi aD\,[P_{vap}\,(Mol.\ wt.\ /\ RT)] \qquad \text{Equation 3.4}$$

Where, Φ was the evaporation rate equal to mass per unit volume and liquid flow rate. D was the diffusion coefficient of vapor (droplet formed at the tip of the syringe) in air at 20 ^{0}C and was roughly equal to 0.1 cm^2/s. Standard conditions were applied for other parameters. Vapor pressure (P_{vap}) was 5.4 kPa, ρ was 0.8669 g/mol, gas constant (R) was 8.314 L.kPa / K and T was 295.15 K.

Table 3.1 presents the radius of each droplet formed, at different syringe flows. The next step was to calculate the time response at different syringe flows. This time response should be equal to the volume of the drop divided by liquid flow rate. The liquid flow replaces what is evaporating, so at steady state the flow rate should be equal to the rate of evaporation.

$$t = (4/3 * \pi * a^3) / Q_L \qquad \text{Equation 3.5}$$

Table 3.1. Calculating droplet radius and the approximate time it would take to stabilize

Syringe Flow (μL/hr)	*a (μm)*	*t (sec)*
0.90	7.80	8.21
0.80	7.70	8.02
0.70	6.64	6.32
0.40	3.80	2.13
0.30	2.84	1.21
0.10	0.94	0.13

Table 3.1 confirmed that at lower syringe flows, less time was required for the droplet to build up, but at higher syringe flows, volume changed tremendously and the droplet took some time to build up. Therefore, the droplet equilibrium time was important. In addition

to that, the sample was also evaporating from the tip of the syringe, as the syringe opening was 0.152 mm across. Thus, it was concluded that the slow time response was associated with the time taken by the droplet formation, on the tip of the syringe and the syringe flows were tried in sequence to check this theory and it was found that the response was quicker than before (figure 3.1).

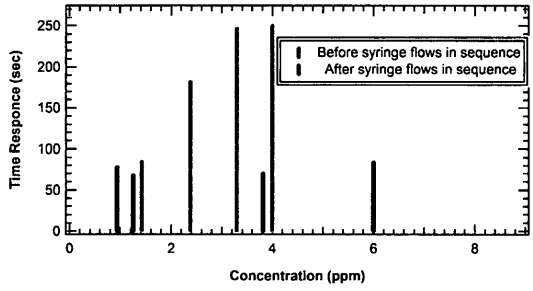

Figure 3.1: Before and after syringe flows tried in sequence

Finally, toluene was injected constantly and different dilutions (concentrations) were made by changing the air flows only. The new apparatus sketch is provided in figure 3.2.

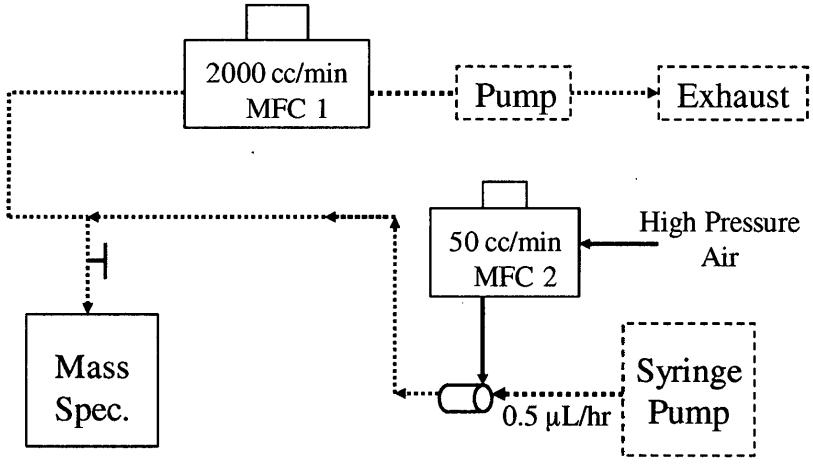

Figure 3.2: Apparatus Sketch for calibrating IT-ToF MS

In figure 3.2, black lines indicate purified air and dark blue dashed line is for pure toluene being injected by the syringe pump. The dashed light blue lines indicate mixing of

sample with air. 50 cc/min mass flow controller (MFC 2) was used to draw a constant air flow through the sample injection septum.

A constant syringe flow of 0.5 μL/hr was injected, using a syringe pump. Different concentrations were obtained by changing air flows through a 2000 cc/min mass flow controller (MFC 1).

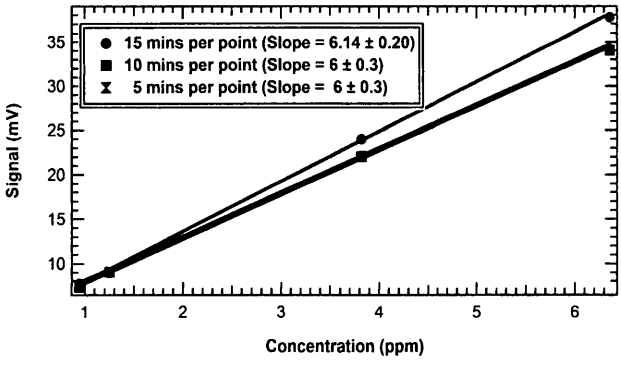

Figure 3.3: Four different air flows at a constant syringe flow

Four different concentrations were selected and time between each concentration change was 15 mins. Then the same procedure was repeated with time taken between each concentration being 10 mins and finally 5 mins (figure 3.3). A line fit was generated for each data set and slope of these line fits provided sensitivity of the equipment. These data sets were reproducible, therefore a good calibration procedure was achieved which could be performed in roughly 2 hours. A brief summary of these results is provided in figure 3.4, which presents the overall trends (in sensitivity) from February to November 2010. Sensitivity

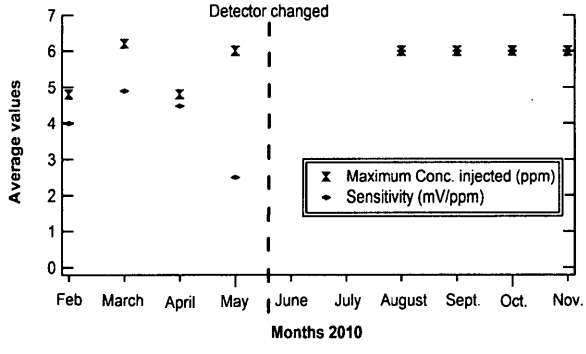

Figure 3.4: Sensitivity trends from February to November 2010

fluctuated, until it dropped in May. So the detector was changed and sensitivity was found to be consistent for the later experiments, which are around 6mV/ppm for the most stable fragment of toluene.

3.3: Calibration Spectra of Isoprene and its Oxidation Products

3.3.1: Introduction

The calibration spectra of isoprene and its oxidation products were generated to determine the fragmentation patterns and to generate the alpha values of all fragments of these organic species. The alpha value is the actual response (or signal) at any mass-to-charge ratio, in units of mV/ppm that remains constant provided the sensitivity of the mass spectrometer remains the same.

Calibration of mass spectrometer revealed that the signal was consistent and we could rely on these alpha values, to calculate the concentration of each fragment as a function of time during the isoprene oxidation experiment.

In determining the alpha value, it was important to keep in mind that any signal used must vary linearly with concentration. Thus, care must be taken to be sure that the signal used was unaffected by secondary chemistry. Linear correlation analysis would be performed to make sure that no secondary ion formation took place.

Also, we need to make sure that there is no depletion of reagent ions due to excessively high analyte concentrations. It requires that, while collecting data, the sensitivity be regularly changed to a scale on which the reagent ion concentration can be measured;

then one can ensure that the reagent ion concentration is reasonably constant over the course of the experiment.

However, rapid injection of a fixed volume of liquid in a known gas flow results in an excessively large initial concentration and uncertainty as to the exact time from which the decay begins. To avoid these problems a fixed volume of liquid analyte is injected by a syringe, into an exponential dilution flask, named the Continuously Stirred Tank Reactor (CSTR). In this way analyte concentration is kept low enough so as to prevent saturation of the instrument. As volume of the CSTR is known, it is also be possible to determine the total analyte being injected.

3.3.2: Experimental Equipment

The basic experimental setup consists of several components: a continuous stirred tank reactor (CSTR), three mass flow controllers (MFC 1, 2 and 3), two valves (A and B), a one microliter capacity syringe and a mass spectrometer.

For this experiment a three-necked round bottom flask with an approximate volume of three liters was used as a continuous stirred tank reactor (CSTR). The liquid sample was injected by one microliter syringe through one of the three necks of the CSTR. A magnetic stirrer was used to enhance turbulent flow to produce uniform mixing and to prevent the formation of dead zones.

The liquid sample or analyte was diluted in the volume of air present inside the CSTR. After a certain period of time (10 minutes in this case), this diluted analyte was allowed

to exit through another neck of the CSTR and the effluent was collected for analysis, by the mass spectrometer. A constant temperature was maintained throughout the process. Figure 3.5 presents the apparatus sketch to acquire calibration spectra.

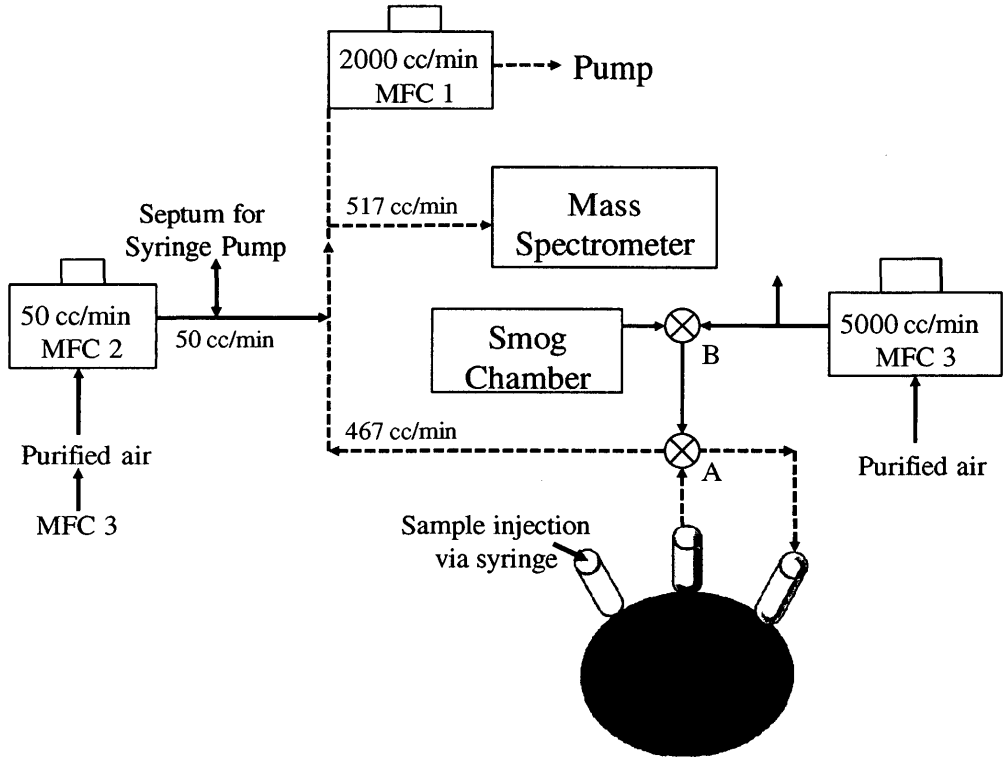

Figure 3.5: Apparatus sketch to acquire calibration spectra

Three mass flow controllers (MFCs) were used to send gas at a calibrated flow rate, towards the mass spectrometer. Mass flow controllers 1 and 2 were calibrated while the uncalibrated MFC3 was used to supply purified air. The purified air was driven into the mass spectrometer by mass flow controller 1 (MFC1), present upstream. The MFC1 was adjusted so as to draw a constant flow rate of 517cc/min of purified air or sample+purified air through the mass spectrometer at all times.

Air flowing through MFC 2 was previously used to retrieve samples from the syringe pump septum (during instrumental calibration experiment). However, 50 cc/min coming from MFC2 added to the total calibrated gas flowing in this experiment; that is 467 cc/min coming from MFC3 and 50 cc/min coming from MFC2. Solid black lines, in figure 3.5, symbolize purified air coming from the mass flow controllers 2 and 3.

Two valves (A and B) are shown in figure 3.5. The three port valve B could be adjusted to bring air from MFC3 or from the smog chamber. For smog chamber experiments it was adjusted to bring samples from the smog chamber. But for now the valve B was adjusted to bring purified air from MFC3. This purified air flowing through valve B was driven in by a pump upstream and was controlled by the MFC 1. Air coming from valve B then passed through the four ports valve A, which sent air flowing either through the CSTR or bypassing it.

3.3.3: Experimental Method

Initially, the position of the valve A was kept such that air coming from MFC 3 flushed the CSTR completely and blank readings were recorded for about half an hour to establish a base line. Then valve A was switched to its other position, where no more air entered or left the CSTR. This was a zero flow state.

Measured volume of liquid sample was directly injected into the CSTR via syringe. It is presented by a solid dark blue arrow, pointing towards one of the three necks of the CSTR (see figure 3.5). The sample evaporated and was allowed to mix well, into the

volume of air present inside. This was the initial mixing ratio (C_0) of sample in air. Dashed dark blue lines in figure 3.5 present this initial mixing ratio of sample flowing back and forth from CSTR, in Teflon tubing attached to valve A, at zero flow state. This initial mixing ratio (C_0) could be calculated using equation 3.6.

$$C_0 = V_{SA} / V \qquad \text{Equation 3.6}$$

Here V_{SA} is the initial gas volume of the analyte (nRT/P), where n is the moles of analyte, R = 8.314 KJ/mol, P = 1 atmospheric pressure and T = 293 K. After 10 mins mixing time at $t = t_0$, the valve A was switched to flow-through state, presented by dashed light blue lines in figure 3.5. A calibrated gas flow Q (from MFC 1 and 2 both) took this diluted sample, from CSTR to the mass spectrometer.

Sample flow concentration in the gas exiting the valve A jumped abruptly from 0 to C_0 and approached to a maximum value and then it started decaying exponentially, as contents of the CSTR were diluted.

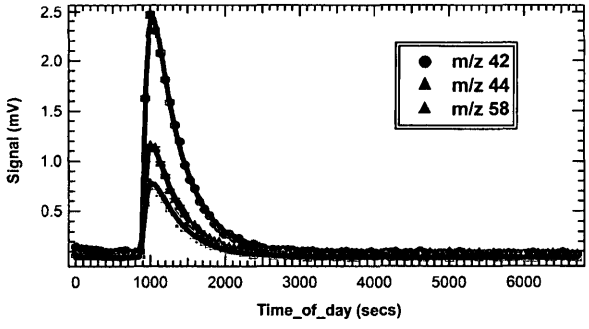

Figure 3.6: Acetone fragments, fitted through CSTR fitting

A data acquisition program, produced a mass spectrum after every one minute; as signal versus time of flight in nanoseconds. This data was collected and translated into mass to charge ratio (m/z) using a fitting procedure in IGOR. A ToF processing template run in IGOR was equipped with macros that were used to extract all significant peaks present. Then variation in signal response

of each ion was studied using a fitting procedure created in IGOR. It was named as "CSTR fits". An example of sample fragments fitted using the CSTR fits is provided in figure 3.6. The derivation of CSTR fitting equation 3.14 is explained briefly, as follows.

3.3.4: Derivation of CSTR Fitting Equation

We assume that the CSTR is perfectly mixed. It is initially prepared in the zero-flow state, by injecting n moles of the species to be studied and allowing sufficient time for complete mixing. Then at time $t = t_0$, CSTR is switched to the flow through state and sample flow concentration coming out of the CSTR, the C_{out}, jumps abruptly from 0 to C_0 in flow exiting the CSTR. Then C_{out} starts to decrease as contents of the flask are diluted. Thus for $t < t_0$

$$C_{out} = 0 \qquad \text{Equation 3.7a}$$

Assume the system operates at a steady-state and a single, irreversible reaction takes place. The exponential form of the expression for the first order reaction, at $t \geq t_0$ is

$$C_{out} = C_0 \ exp\ [-(t - t_0) / \tau_D] \qquad \text{Equation 3.7b}$$

It gives the concentration of diluted sample in the outlet stream at any time $t \geq t_0$. Here τ_D is the average amount of time a molecule spends inside the CSTR. It is called the residence time or the dilution time constant.

$$\tau_D \equiv V/Q \qquad \text{Equation 3.8}$$

Now diluted analyte is sampled into the ionization region of the mass spectrometer with a resident time constant τ_I. Time variation of concentration C_I in the ionization region is given by

$$d C_I / dt = (C_{out} - C_I) / \tau_I \qquad \text{Equation 3.9}$$

C_I either increases or decreases until it is equal to C_{out}.

For $t < t_0$, $$C_I = 0 \qquad \text{Equation 3.10}$$

For $t \geq t_0$, time variation of C_I is going to be:

$$C_I = [(C_0 \tau_D) / (\tau_D - \tau_I)] \{[exp - (t - t_0) / (\tau_D] - [exp - (t - t_0) / (\tau_I)]\} \qquad \text{Equation 3.11}$$

Thus equation 3.11 provides us with the time dependence of concentration in the ionization region.

In the absence of saturation effects, the measured signal should be a linear function of the analyte concentration. Thus, we assume that mass spectrometer signal S is given by

$$S = S_0 + \alpha C_I \qquad \text{Equation 3.12}$$

Where α is an unknown response factor that must be determined and S_0 is a possible non-zero background when no analyte is present. Expressing S in terms of Q and τ is preferable since these quantities can be accurately measured, but V is not accurately known. The determination of α is the objective of this procedure.

Measured signal is averaged over some time interval, say Δt. If t refers to the time at the beginning of the averaging interval, then the time, t_2, at the end of the interval is $t_2 = t + \Delta t$. Taking the average of equation 3.11 yields

$$\langle C_I \rangle = [(C_0\,\tau_D) / (\Delta t)\,(\tau_D - \tau_I)]\,[\,f(t, t_0, t_2, \tau_D) - f(t, t_0, t_2, \tau_I)] \qquad \text{Equation 3.13(a)}$$

where $$f(t, t_0, t_2, \tau) = \tau\,\{exp\,[-(t - t_0) / (\tau)] - exp\,[-(t_2 - t_0) / (\tau)]\} \qquad \text{Equation 3.13(b)}$$

If $t_2 \leq t_0$, we have $\langle C_I \rangle = 0$ since $C_I = 0$ at all times during the averaging interval. If $t \geq t_0$, then equation 3.13(b) applies as written above. Independent averaging of C_I^2 would be carried out, to include the quadratic term in equation 3.12. It is simpler and perhaps adequate to use the square of $\square C_I \square$, this gives the approximate expression

$$S = S_0 + \alpha\,\square C_I \square \qquad \text{Equation 3.14}$$

Thus the parameters required for the above equation are V_{SA}, Q, Δt, V, t_0, τ_I (or τ_{aul}), S_0 and α. With the first three fixed at their calculated values and the other five are determined by CSTR fitting procedure written in IGOR.

3.3.5: Acquiring Data through CSTR Fits

This section is provided as an example. CSTR data for acetone fragments was acquired in the following manner. Starting from one peak at a time, the signal of molecular ion peak at m/z 58 was fitted first. First 3 parameters V_{SA}, Q and Δt were calculated and fixed, as shown in table 3.2, ± 0.0 indicates a fixed value.

V_{SA} was calculated using equation 3.6. Q was determined from the calibrated air flowing through MFC 1 and 2, in units of cc/sec. t_{avg} of a measured signal was an average over time interval Δt (usually this would be the time interval between successive data points).

Errors limits in table 3.2 indicate the standard errors in the slope values; these are the uncertainty in the slope values resulting from the statistical scatter in the measurements.

For unfixed parameters initial guesses were manually inserted and conditions were relaxed. These guesses were taken from information available; for example volume of the CSTR was expected to be around 3000 mL. Time switched to ToF should be around 600 seconds. Instrumental time constant always come out to be a little over than 60 seconds (instrumental calibrations revealed this information). The background signal could be guessed from the signal response. Alpha value could be calculated by dividing signal with initial mixing ratio (C_0).

Once the signal at m/z 58 was fitted, the resulting values are provided in table 3.2, as coefficient values ± standard errors. Thes e values are obtained using the non-linear regression procedures in Igor.

The same procedure was repeated for other acetone fragments as well, again provided in the table 3.2. Chi square values indicate how good the individual lines were fitted. It is important to note here that when fitting multiple signals, from a single experiment the parameters V, t_0, and τ_I from all fits should agree to within the experimental error.

Table 3.2. CSTR fitting data for all acetone fragment ions

Mass	*units*	*42*	*43*	*44*	*58*
Initial gas volume of acetone (V_{SA})	μL	32.8 ± 0.0	32.8 ± 0.0	32.8 ± 0.0	32.8 ± 0.0
gas flow rate (Q)	cc / sec	8.61 ± 0.00	8.61 ± 0.00	8.61 ± 0.00	8.61 ± 0.00
Averaging interval (t_{avg})	Sec	66.0 ± 0.0	66.0 ± 0.0	66.0 ± 0.0	66.0 ± 0.0
Volume of the flask (V)	mL	3220.0 ± 1.0	3210.0 ± 1.0	3240.0 ± 2.0	3260.0 ± 2.0
Time switched sample to ToF (t_0)	sec	924.0 ± 1.0	924.0 ± 0.2	924.0 ± 1.0	924.0 ± 1.0
Instrumental time constant (τ_I)	sec	61.0 ± 2.0	60.0 ± 1.0	60.0 ± 2.0	60.0 ± 1.5
Background signal (S_0)	mV	0.080 ± 0.001	0.750 ± 0.002	0.080 ± 0.001	0.038 ± 0.001
Signal / concentration (α)	mV/ ppm	0.28 ± 0.01	3.40 ± 0.02	0.16 ± 0.01	0.10 ± 0.01
Chi sq.		280	340	328	316
No of data points fitted (V_ npnts)		103	103	103	103

3.3.6: Conclusions

3.3.6.1: CSTR Fitting Data for Isoprene and its Oxidation Products

Table 3.3. Weighted averages of values obtained from CSTR fittings

CSTR parameters	*units*	*Isoprene*	*Methacrolein*	*MVK*
Volume of the flask (V)	mL	3120.0 ± 3.0	3220.0 ± 3.0	3220.0 ± 3.0
Instrumental time constant (tau_I)	Sec	85.0 ± 2.0	103.0 ± 3.0	105.0 ± 2.0

Overall, volume of the flask obtained in each experiment was a little more than expected. There was agreement between various results except for isoprene, a small difference in inferred flask volumes (approx. 2.5%) was observed perhaps due to a small error in the gas flow rate.

3.3.6.2: Response Factor

Table 3.4 provides the alpha values or response factors obtained at different fragments of isoprene and its oxidation products.

Table 3.4. Response factor (α) values obtained for fragments of isoprene and its oxidation products

Ions (m/z)	*α (mV / ppm)*			
	Isoprene	MACR	MVK	Acetone
39	0.4049 ± 0.0001	1.0710 ± 0.0021	0.3580 ± 0.0002	
40	0.0340 ± 0.0001	0.0620 ± 0.0011		
41	0.0821 ± 0.0001	0.3300 ± 0.0011	0.1760 ± 0.0001	
42		0.2540 ± 0.0014	0.2280 ± 0.0002	0.2800 ± 0.0002
43			1.0142 ± 0.0003	5.0571 ± 0.0001
44				0.1347 ± 0.0001
50	0.0269 ± 0.0001			
51	0.2153 ± 0.0002			
53	1.2366 ± 0.0003	0.4500 ± 0.0021	0.1380 ± 0.0001	
54	0.0628 ± 0.0003			
55			5.6530 ± 0.0002	
56			0.1896 ± 0.0001	
57	0.0412 ± 0.0001			
58				0. 1380 ± 0.0001
65	0.1596 ± 0.0001			
66	0.0571 ± 0.0001			
67	4.1000 ± 0.0001			
68	1.0186 ± 0.0003			
69		0.4700 ± 0.0023		
70		1.0290 ± 0.0034	0.3490 ± 0.0003	
71		0.1400 ± 0.0012		
85		0.3624 ± 0.0023		

The alpha values from table 3.4 were plotted against their respective fragments, to generate calibration spectra. They are presented as follows.

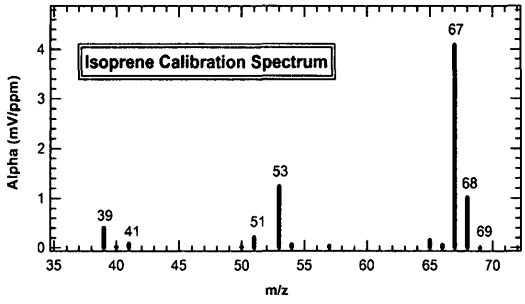

Figure 3.7: Calibration spectrum for isoprene

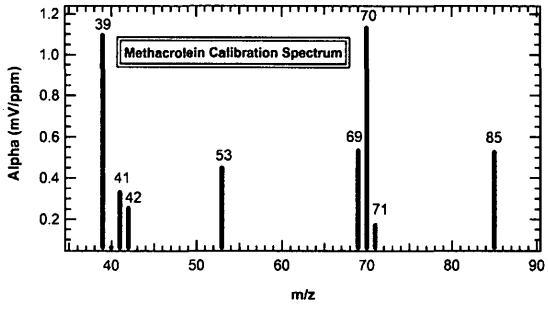

Figure 3.8: Calibration spectrum for methacrolein

The first compound to be analyzed was isoprene (C_5H_8) and molecular weight 68.12 g/mol. All significant signals, with signal-to-noise ratio 3:1, were extracted and studied. M/z 67 was found to be the most stable fragment. Figure 3.7 presents the isoprene calibration spectrum, generated by plotting alpha values, from table 3.4 against the respective isoprene fragments.

Figure 3.8 presents the calibration spectrum of methacrolein (MAC) or 2-methylprop-2-enal, (C_4H_6O) and molecular weight 70.09 g/mol. The most stable fragment of methacrolein was observed at m/z 70. The heavier fragment at m/z 85, in figure 3.8, is generated by the ionization reaction of m/z 70 (the molecular ion peak of MAC) with O_2^+ ions.

$$\underset{\text{m/z } \mathbf{70}}{C_4H_6O} + O_2^+ \longrightarrow \underset{\text{m/z } \mathbf{85}}{C_4H_5O_2^+} + OH \qquad \text{reaction 3.1}$$

Some supporting evidence of m/z 85 was obtained from previously published literature (*Winter*, 2002); however its heat of formation is unknown.

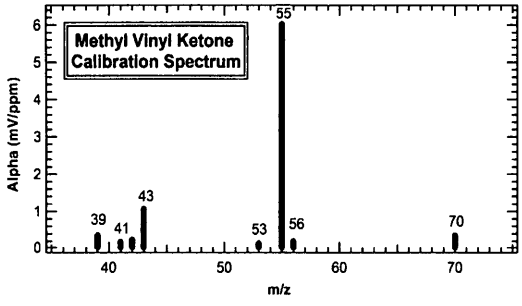

Figure 3.9: Calibration spectrum for Methyl Vinyl Ketone

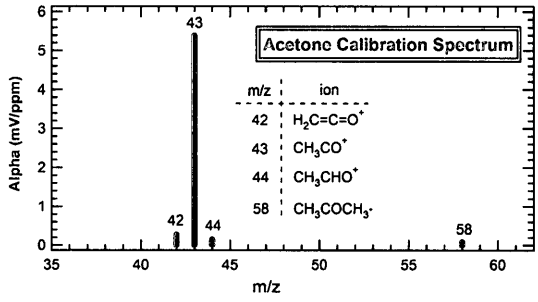

Figure 3.10: Calibration spectrum for acetone

Alpha values of all methyl vinyl ketone (MVK) fragments are plotted in figure 3.9. Methyl vinyl ketone or but-3-en-2-one has the same chemical formula and molecular weight as of methacrolein. As shown is figure 3.9, the most stable MVK fragment was observed at m/z 55.

Acetone was generated during IPN photolysis and photochemical production of OH-radicals. Figure 3.10 presents the calibration spectrum of acetone (CH_3COCH_3) and molecular weight is 58.09 g/mol. M/z 43 was found to be the most stable fragment, while other fragments obtained were m/z 42, 44 and 58. Data from figure 3.10 would be compared with the data obtained during IPN photolysis experiment.

3.4: Statistical tool, to Check for Secondary Ion Formation

Secondary ions could be generated by the reaction between primary fragments; therefore all fragments were compared by their linear relationship with the molecular ion peak or the most stable primary fragment. Linear correlation was analyzed using linear fit routines as described by *Press,* (1996). Two data sets, x and y, from two different fragments, were fitted using a chi square (χ^2) fit to a straight line y = i + sx (linear

correlation analysis of *Press 1996*) with errors in both variables, x and y. Here y is the independent variable (the most stable sample fragment), while x is the dependant variable (the other possible sample fragment). i represents the intercept, while s is the slope of the linear fit. For a best fit result, the chi square (χ^2) value should be comparable to the number of data points being fitted. This would be an indication that scatter agrees with the estimated errors. Low values of χ^2 are likely due to overestimated errors in x and y, while the opposite can be the result of an inappropriate straight line model or an underestimation of the errors in x and y; furthermore, a tail of outliers will lower the χ^2 value.

A measure of an acceptable size of the errors in x and y are the χ^2 values (*Press, 1996*). These will determine whether the fit result and its errors are acceptable. For each of our fits we will report the resulting error limits for slopes based on our estimated data variability and the correlation of the two data samples (fragments) is evaluated by linear correlation analysis (the routines of *Press,* 1996). All results of the statistical analysis, which will be discussed, are summarized in tables 3.5-3.8.

Validity of this linear assumption would also be confirmed if the slope values generated from linear correlation graphs agreed with the ratios of alpha values from table 3.4.

Toluene will be presented as an example of secondary ion formation. The data presented on toluene fragments is not a part of this thesis. Toluene has been shown to fragment under electron impact by the sequence shown in reaction 3.2 (*Coggon,* 1968). M/z 92 is

the parent ion; this value indicates the molecular weight of toluene. The parent ion disintegrates into several fragments. The most intense peak by far is obtained at m/z 91, which further disintegrated to form m/z 65 and other fragments. Few of these fragments are plotted against m/z 92, in figures 3.11 (a) and (b).

In figure 3.11 (a), m/z 91 and 65 showed linear dependence on m/z 92. Thus these three fragments generated at the same time and were primary fragments of toluene. In figure 3.11 (b) the outcome or dependence was non-linear, thus m/z 78 and 105 resulted from some secondary reaction (see reaction 3.3).

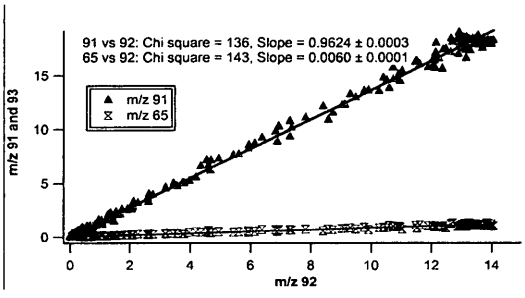

Figure 3.11(a): Linear correlation between m/z 92 and toluene fragments m/z 91 and 93

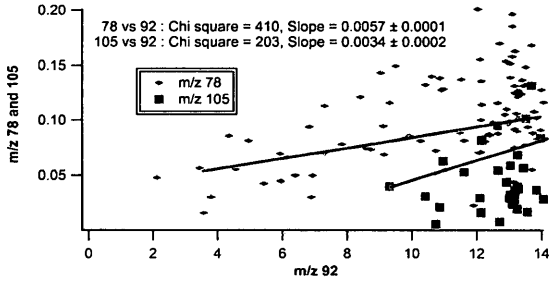

Figure 3.11(b): Non-linear correlation between m/z 92 and toluene fragments at m/z 78 and 105

Also in figure 3.11(a), chi square values were comparable to the number of data points being fitted that is 140. However, in figure 3.11(b) the data points for m/z 78 and 105 were 100 and 40 respectively and chi square values were high. Thus linear correlation analysis revealed that m/z 91 and 65 were primary fragments, while m/z 78 and 105 were secondary fragments of toluene. Possible reactions would be:

$$\underset{\text{m/z } \mathbf{92}}{C_7H_8} \xrightarrow{-e^-} \underset{\text{m/z } \mathbf{92}}{C_7H_8^+} \xrightarrow{-H^\cdot} \underset{\text{m/z } \mathbf{91}}{C_7H_7^+} \xrightarrow{-C_2H_2} \underset{\text{m/z } \mathbf{65}}{C_5H_5^+} \qquad \text{reaction 3.2}$$

$$\underset{\text{m/z } \mathbf{91}}{C_7H_7^+} + \underset{\text{m/z } \mathbf{92}}{C_7H_8} \longrightarrow \underset{\text{m/z } \mathbf{105}}{C_8H_9^+} + \underset{\text{m/z } \mathbf{78}}{C_6H_6} \qquad \text{reaction 3.3}$$

Linear correlation analysis for isoprene and its oxidation products, are provided as follows:

3.4.1: Isoprene

Isoprene fragmented into ions with m/z 40, 41, 50, 51, 54, 57, 65 and 66. The linear correlation analysis was performed between the most dominant fragment at m/z 67 and the other isoprene fragments. A summary of slope and chi square values generated from linear correlation graphs is presented in table 3.5. The chi square values generated from the linear correlation fits, show if the scatter in data sets agrees with the estimated errors.

Table 3.5. Slope and Chi square values for isoprene fragments

Species		*Linear Fit - Linear Correlation*		**From table 3.4**
m/z	*No. of data points*	*Chi squares (χ^2)*	*Slope (versus m/z 67)*	*Ratios of alpha values with α_{67}*
39		170	0.0981 ± 0.0002	0.0987 ± 0.0001
40		90	0.0085 ± 0.0001	0.0083 ± 0.0001
41		236	0.0205 ± 0.0001	0.0200 ± 0.0001
50		311	0.0064 ± 0.0001	0.0065 ± 0.0001
51	144	208	0.0518 ± 0.0001	0.0525 ± 0.0002
53		167	0.3003 ± 0.0010	0.3016 ± 0.0003
54		223	0.0149 ± 0.0001	0.0153 ± 0.0003
57		158	0.0101 ± 0.0001	0.0101 ± 0.0001
65		210	0.0386 ± 0.0002	0.0389 ± 0.0001
66		219	0.0146 ± 0.0001	0.0140 ± 0.0001
68		187	0.2480 ± 0.0010	0.2484 ± 0.0003

As shown in table 3.5, the chi square values are acceptable and comparable to the number of data points being fitted (n = 144). Thus scatter agrees with the estimated errors. Ratios of alpha values with alpha at m/z 67, the α_{67}, from table 3.4, are also provided. Comparison of slope values with these ratios is also acceptable within ± 2%, indicating the reliability of the linear correlation analysis. These slope values from table 3.5 would

be compared with slope values generated during isoprene oxidation experiment. If slopes agreed, based on graph and fit quality, then the alpha values would also agree. Thus alphas from table 3.4 could be used in calculating concentration of isoprene as a function of time, in the isoprene smog chamber experiment.

3.4.2: Methacrolein (MAC)

Summary of the linear correlation analysis of methacrolein fragments versus m/z 70 is provided in table 3.6. The linear correlation study revealed no secondary ion formation.

Table 3.6. Slope and Chi square values for methacrolein fragments

Species		*Linear Fit - Linear Correlation*		**From table 3.4**
m/z	*No. of data points*	*Chi squares (χ^2)*	*Slope (versus m/z 70)*	*Ratios of alpha values with α_{70}*
39		186	1.0382 ± 0.0031	1.0408 ± 0.0021
40		121	0.0571 ± 0.0014	0.0602 ± 0.0011
41		198	0.3154 ± 0.0012	0.3206 ± 0.0011
42	155	159	0.2591 ± 0.0013	0.2468 ± 0.0014
53		148	0.4323 ± 0.0021	0.4378 ± 0.0021
69		146	0.4551 ± 0.0023	0.4567 ± 0.0023
71		168	0.1332 ± 0.0012	0.1360 ± 0.0012
85		135	0.3541 ± 0.0021	0.3521 ± 0.0023

Chi square values are comparable to number of data points being fitted. Also, agreement of the slope value with ratios from table 3.4 is not bad, within an acceptable range of roughly ± 4%. Thus the slope values from table 3.6 are valid and would be compared with slopes generated during isoprene oxidation experiment.

3.4.3: Methyl Vinyl Ketone (MVK)

M/z 55 was the dominant fragment for MVK. Slopes and chi square values from linear correlation analysis between m/z 55 and other MVK fragments is provided in table 3.7.

Table 3.7. Slope and Chi square values for methyl vinyl ketone fragments

Species	*Linear Fit - Linear Correlation*			**From table 3.4**
m/z	*No. of data points*	*Chi squares (χ^2)*	*Slope (versus m/z 55)*	*Ratios of alpha values with α_{70}*
39	60	75	0.0640 ± 0.0002	0.0633 ± 0.0002
41		53	0.0310 ± 0.0002	0.0311 ± 0.0001
42		66	0.0401 ± 0.0002	0.0403 ± 0.0002
43		67	0.1791 ± 0.0004	0.1794 ± 0.0003
53		56	0.0251 ± 0.0001	0.0244 ± 0.0001
56		52	0.0333 ± 0.0002	0.0335 ± 0.0001
70		67	0.0631 ± 0.0003	0.0617 ± 0.0003

The linear correlation analysis revealed straight lines, indicating no secondary ion formation. In table 3.7, chi squares are comparable to number of data points being fitted and slopes agree with the ratios from table 3.4, within ± 2.5 %. Thus slope values from table 3.7 are acceptable.

3.4.4: Acetone

For acetone, linear correlation was studied between the most stable fragment at m/z 43 against the other acetone fragments at m/z 42, 44 and 58. Results are provided in table 3.8. The linear correlation study indicated no secondary ion formation.

Table 3.8. Slope and Chi square values for acetone fragments

Species	*Linear Fit - Linear Correlation*			**From table 3.4**
m/z	*No. of data points*	*Chi squares (χ^2)*	*Slope (versus m/z 43)*	*Ratios of alpha values with α_{70}*
42	121	138	0.0553 ± 0.0002	0.0553 ± 0.0002
44		131	0.0261 ± 0.0001	0.0266 ± 0.0001
58		123	0.0271 ± 0.0001	0.0272 ± 0.0001

3.5: IPN Photolysis in the Smog Chamber

3.5.1: Introduction

During isoprene oxidation, isopropyl nitrite (IPN) was used as a source of OH radicals; therefore we needed a calibration spectrum for IPN as well. This would help us to account for all the fragment ions belonging to IPN, during isoprene smog chamber experiment. However, direct calibration of IPN was not possible as purity of this compound could be poor.

Thus, photochemical degradation of IPN was studied in the absence of NO or any hydrocarbons. The first order decay of IPN in air was monitored to generate a calibration spectrum of IPN for comparison with isoprene oxidation experiment. The possible reactions are also provided.

The chemical formula for IPN is $C_3H_7NO_2$ and its molecular weight is 89.09 g/mol. We expected to observe two groups of fragments, in this experiment. The first group of fragments would belong to IPN itself which would be consumed by photolysis and the second group would belong to acetone, which is the main primary product of this reaction.

3.5.2:Procedure

Before starting the experiment, air was drawn from the smog chamber into the mass spectrometer and blank readings were taken for half an hour to establish a base line. Then 22.0 μL of freshly prepared isopropyl nitrite (IPN) was admitted into the chamber through the injection port and allowed to mix well with air for about 70 minutes, with UV

lights off. Turning on the UV lights initiated the photochemical degradation of IPN and production of OH radicals. The reaction was allowed to proceed for three hours with one full scan mass spectrum obtained every one minute. After three hours the lights were turned off. Data obtained were analyzed to generate time profiles for each of the masses collected throughout the process.

General Time Profile of IPN Photolysis

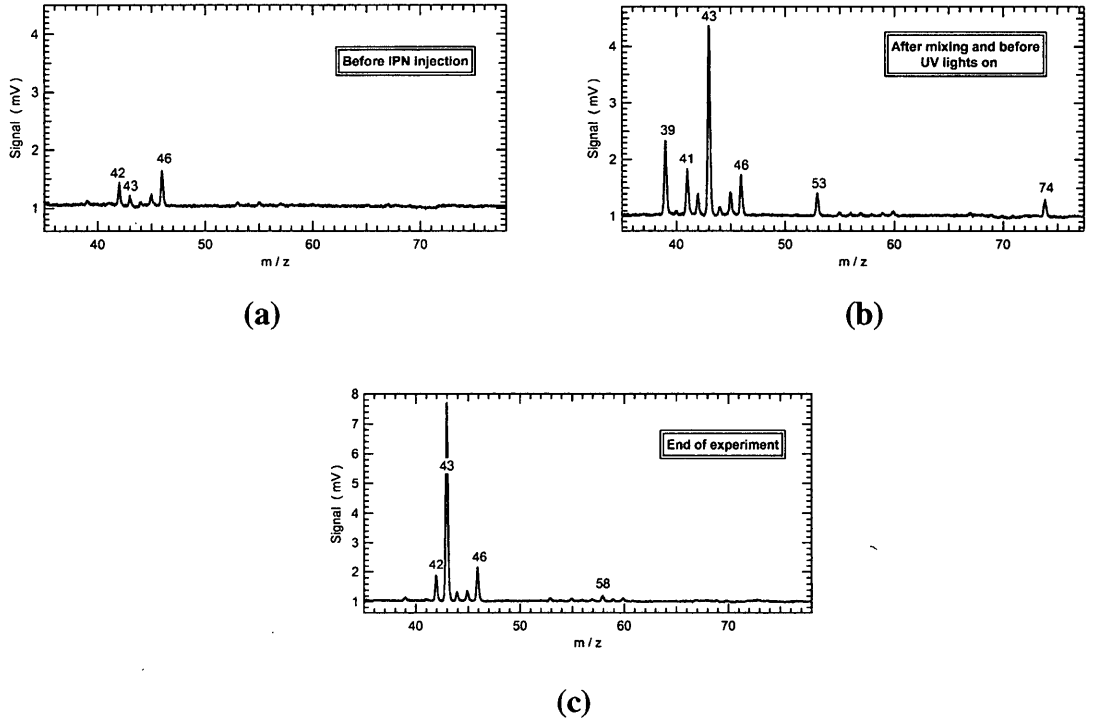

Figure 3.12: Overall signal trend starting from base line till the end of experiment

We observed three groups of analytic fragments. Before injection some background signal was already present. Then right after injection, IPN fragments were obtained and when UV lights were turned on, the IPN was consumed by photolysis. The third set of fragments belonged to acetone, which were produced soon after turning the UV lights on. Figure 3.12 (a) presents a mass spectrum before injecting IPN. Thus m/z 42, 43, 44, 45 and 46 were already present before injecting any IPN. Extremely low signals at m/z 39

and 53 were also observed. All these appeared to be a constant background before IPN injection and after the end of the experiment (see figure 3.12 c).

Figure 3.12 (b) presents a mass spectrum after analyte mixing and before the UV lights on. Acetone fragments at m/z 42 and 44 were already present and there was a slight increase in their signal intensity after IPN injection. Signal at m/z 45 was also increased, while m/z 46 remained unaffected. M/z 43 had a tremendous increase in signal intensity. M/z 74 was obtained by removal of one methyl group from IPN. Thus it was expected to be an IPN fragment only.

Figure 3.12 (c) presents a mass spectrum after IPN photolysis at end of the experiment. All IPN was gone by this time and essentially all the signal present should be acetone except for m/z 46 which is nitrogen dioxide (NO_2).

Time Profile of IPN during Photolysis

Figure 3.12 shows the possible IPN fragments which started decaying once UV lights were switched on. M/z 41 had good signal intensity and was generated as an IPN fragment only, so was used to study linear correlation with other IPN fragments at m/z 39, 53 and 74. All of these seemed to correlate, as shown in figure 3.13. Before injection signal was treated as a constant background and was subtracted from all spectra, this resulted in zero intercepts during correlation study in figure 3.13.

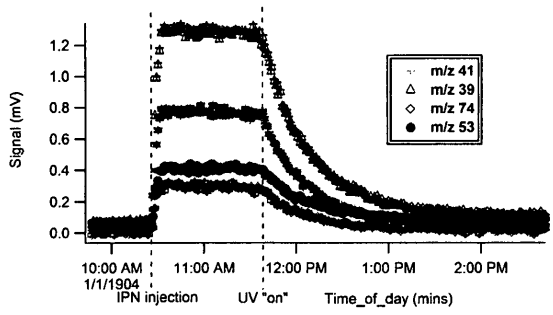

Figure 3.13: Time profile of IPN fragments

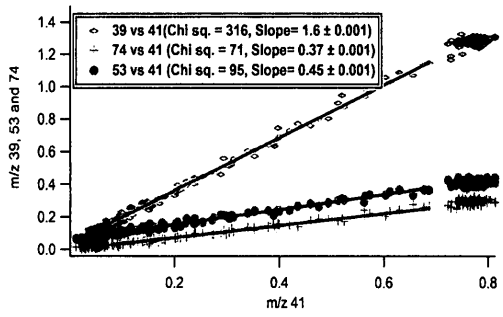

Figure 3.14: Linear correlation plot of IPN fragments versus m/z 41

A small portion of m/z 43 seemed to have a linear correlation with m/z 41(the IPN fragment). So another linear correlation was studied between m/z 43 and m/z 58 (the molecular ion peak of acetone). Both masses correlated when the UV lights were turned on (figure 3.15 b). Thus m/z 43 was contributed by IPN and acetone. While m/z 39, 41, 53 and 74 were contributed by IPN only. Figure 3.13 also revealed that all IPN was lost by the end of the experiment.

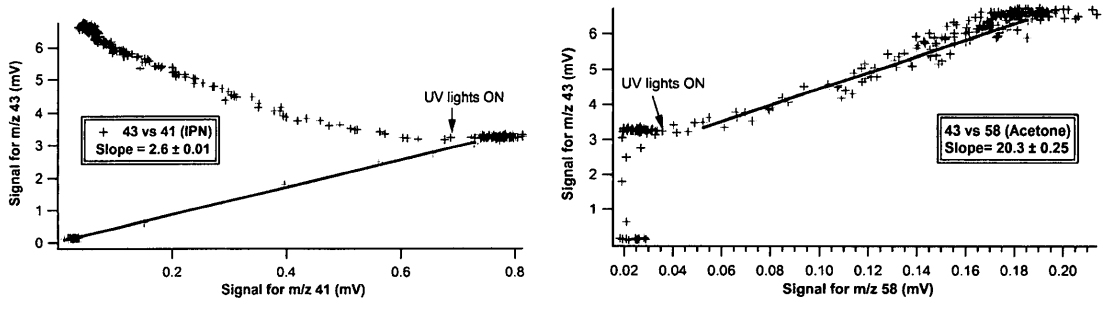

(a) **(b)**

Figure 3.15: Studying correlation of m/z 43 with (a) IPN and (b) acetone

From figure 3.15 it seemed that with UV lights off m/z 43 belonged to IPN and acetone. And with UV lights on, there was an abrupt increase in its signal intensity due to acetone production. Thus we needed to separate acetone and IPN contributions for m/z 43.

Time Profile of Acetone during Photolysis

Information obtained through acetone calibration spectrum was used to identify possible acetone fragments. These were m/z 42, 43, 44 and 58. They were plotted as a function of time in figure 3.16, except for m/z 43.

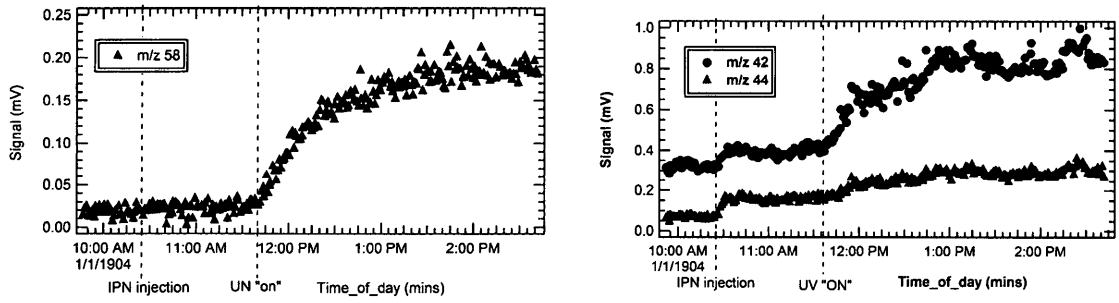

(a) **(b)**

Figure 3.16: Time profile of acetone fragments

If a small fraction of acetone was present before IPN injection, as compared to the acetone produced in the end; then for practical purposes we could assume that there is no acetone in IPN.

Figure 3.16 revealed that a small concentration of acetone fragments (m/z 42 and 43) was already present before IPN injection. This is reasonable since these fragments might be due to acetone contamination or because IPN produces the same fragments.

However, m/z 58 seemed to be unaffected, which suggested that it was contributed only by acetone. But, the system was not very sensitive and we couldn't tell if there was any signal at m/z 58 (the S_{58}), before UV lights were turned on. Therefore, investigation was required to confirm that m/z 58 was a pure acetone fragment. For this purpose, all data

points at m/z 58 before and after IPN injection were averaged, to get standard deviation and root mean square value of uncertainty.

For every data point there was a value y_i and a error estimate σ_i. The σ_i is the estimate of standard deviation in the measured data point y_i and is given by equation 3.15.

$$(\sigma^2)^{1/2}_{error} = (1/N \Sigma_i \sigma_i^2)^{1/2} \quad \text{Equation 3.15}$$

$$(\sigma^2)^{1/2}_{sample} = (1/N \Sigma_i (y_i - \langle y \rangle)^2)^{1/2} \quad \text{Equation 3.16}$$

Where

$$\langle y \rangle = 1/N \Sigma_i y_i \quad \text{Equation 3.17}$$

$(\sigma^2)^{1/2}_{sample}$ is the sample standard deviation computed from all data points y_i, while $\langle y \rangle$ is the average of all the data points. All calculations are provided in table 3.9 where the difference between the square roots of σ_{error} and σ_{sample} was found to be very small, therefore the standard error of the mean was calculated as a next step, using equation 3.18. All values are provided again in table 3.9.

$$\textbf{Standard error} = \textbf{Standard deviation} / \sqrt{N} = (\sigma^2)^{1/2}_{error} / \sqrt{N} \quad \text{Equation 3.18}$$

Table 3.9. Calculations to determine consistency of noise with error

	Units	*Before injecting IPN*	*After Injecting IPN*	*End of experiment (all IPN consumed)*
$(\sigma^2)^{1/2}_{error}$		8.80	9.00	9.86
$(\sigma^2)^{1/2}_{sample}$		7.10	7.80	10.20
$\langle y \rangle$	μV	17.4	20.4	191.0
No. of points averaged for $\langle y \rangle$		35.0	65.0	35.0
Standard error		1.5	1.1	1.6

The average values <y> before IPN injection was 17.4 μV and after IPN injection was 20.4 μV and the change was around 3.0 μV. The total standard error was calculated using equation 3.19.

$$(\Delta \sigma)^2 = (\sigma_{before})^2 + (\sigma_{after})^2 \qquad \text{Equation 3.19}$$

so $$\Delta \sigma = \sqrt{(1.5)^2 + (1.1)^2} = 1.9\ \mu V$$

95% confidence intervals are roughly twice the standard error. So the lower limit was 0.0 and the upper limit was 6.8 μV. This increase could be due to IPN contributing at m/z 58, but that was not likely since that m/z was not easy to make from IPN. So this concluded that a small amount of acetone was present in IPN. Final signal at m/z 58 was 191 μV. So the best estimate (from 100 × 3.0 / 191) was 1.6% of acetone in the IPN. It was small enough to assume that initial acetone was essentially zero. Next step was to figure out the response factor of m/z 58. Figure 3.12 revealed that by the end of IPN photolysis, all IPN was consumed and we were left with the products only. So linear correlation analysis was performed between m/z 43 and 58, in last hour of the experiment, as shown in figure 3.17. Based on fit quality, the slope value of the linear fit was found to be similar to the slope value generated during linear correlation analysis between m/z 43 and 58 in acetone calibration experiment (table 3.8). A similar slope value meant a similar alpha value or response factor.

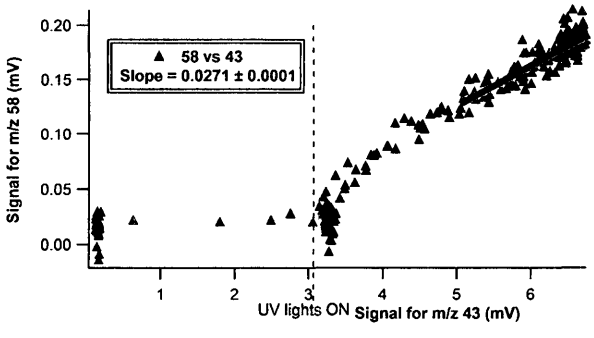

Figure 3.17: Linear correlation analysis of acetone fragments versus m/z 43

The signal of m/z 58 changing with time, the S_{58}, was known and the response factor at m/z 58, the $\alpha_{(58,\ acet)}$, was also known from acetone calibration spectrum. Therefore, concentration of acetone changing with time could be calculated, using equation 3.20.

$$S_{58} = C_{(t),\ acet} \times \alpha_{(58,\ acet)} \qquad \text{Equation 3.20}$$

Where $C_{(t),\ acet}$ is the concentration of acetone as a function of time. Figure 3.18 is the graphical presentation of $C_{(t),\ acet}$ changing with time.

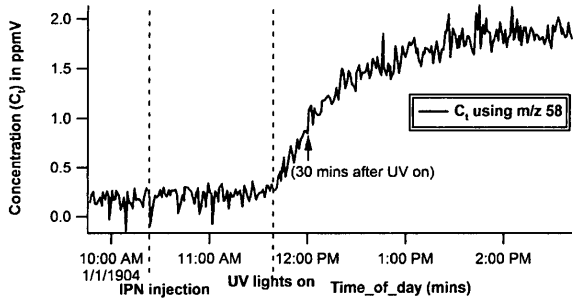

Figure 3.18: Concentration of acetone ($C_{(t),acet}$) changing with time

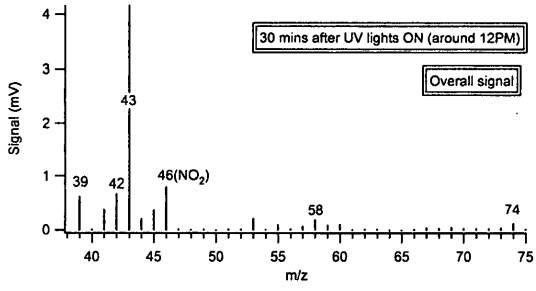

Figure 3.19: An example spectrum at 30 mins after UV lights on

An example spectrum of overall signal is provided in figure 3.19, at 30 mins after UV lights on where both reactants and products can be seen. The next step was to remove the acetone contribution from the overall signal. Starting from m/z 43, the acetone contribution in m/z 43, the $S_{43,\ acet}$, was calculated using equation 3.21. Similarly, the acetone contribution at m/z 42, 44 and 58 was calculated. The alpha values were used from the acetone calibration experiment.

$$S_{43,\ acet} = C_{(t),\ acet} \times \alpha_{43} \qquad \text{Equation 3.21}$$

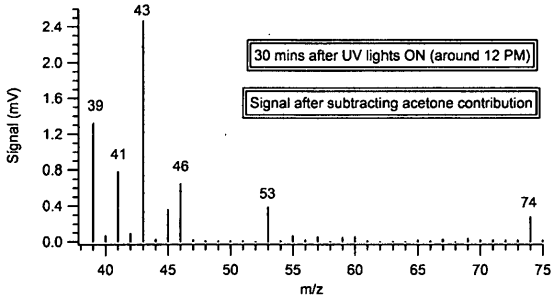

Figure 3.20: Signal after removing acetone contribution from overall signal at 30 mins after UV "ON"

This acetone contribution was then removed from the overall signal. An example spectrum of the remaining signal is presented in figure 3.20, at 30 minutes after UV lights on. It can be compared with figure 3.19.

The IPN contribution at m/z 43, the $S_{43,\,IPN}$, was calculated using equation 3.22. Figure 3.21 presents the IPN and acetone contributions separated at m/z 43.

$$S_{43,\,IPN} = S_{43} - S_{43,\,acet} \qquad \text{Equation 3.22}$$

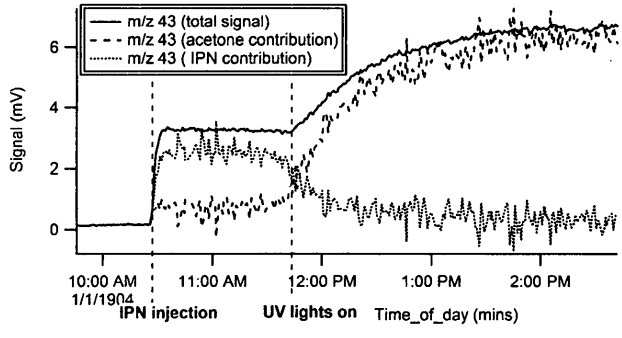

Figure 3.21: Separating signal contributions of acetone and IPN at m/z 43

3.5.3: IPN Calibration Spectrum

Activating UV lamps resulted in photo chemical degradation of IPN and production of acetone and OH radicals.

$$\underset{\text{IPN}}{(CH_3)_2HCONO} + h\nu \rightarrow \underset{\text{m/z } \mathbf{69}}{(CH_3)_2HCO^{\cdot}} + NO \qquad \text{reaction 3.4}$$

$$(CH_3)_2HCO^{\cdot} + O_2 \rightarrow \underset{\text{m/z } \mathbf{58}}{(CH_3)_2CO} + HO^{\cdot}_2 \qquad \text{reaction 3.5}$$

$$HO^{\cdot}_2 + NO_{(g)} \rightarrow OH^{\cdot} + NO_2 \quad \text{(m/z 46)} \qquad \text{reaction 3.6}$$

For every one mole of IPN consumed, one mole of acetone was generated (reaction 3.4 and 3.5). Thus if acetone concentration was zero in start and IPN concentration was zero in the end, then

$$C_{(t),\,IPN,\,initial} = C_{(t),acet,\,final} \qquad \text{Equation 3.23}$$

or better

$$C_{(t),\,IPN} = C_{(t),\,acet,\,final} - C_{(t),\,acet,} \qquad \text{Equation 3.24}$$

Thus if concentration of acetone was known as a function of time, concentration of IPN could also be calculated as a function of time, using equation 3.24. 1.6% of acetone in the injected IPN was removed first, prior to calculating for $C_{(t),\,IPN}$. Figure 3.22 is the graphical presentation of IPN concentration changing with time.

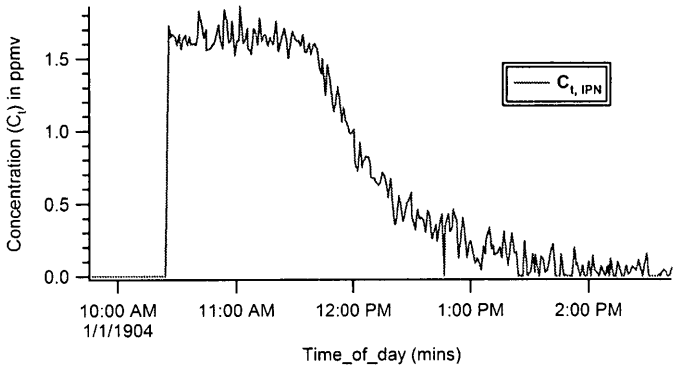

Figure 3.22: Concentration of IPN ($C_{(t),\,IPN}$) changing with time

The maximum concentration obtained from equation 3.20, could be compared to the one calculated from 22.0 μL of IPN injected, as follows:

Moles of IPN = density × volume / mol. Wt. = 0.87 g/cm^3 × 22.0 μL / 89.09 g/mol

= 214.83 × 10^{-6} mol

$$V_{SA} = \text{moles of IPN} \times [R\ T] / [P] \times 10^6 \text{ ppm}$$

$$= 5233.26 \text{ cm}^3.\text{ ppm}$$

$$C_0 = V_{SA} / V = 1.635 \text{ ppm}$$

So $C_{(t),IPN,\ initial}$ was estimated to be around 1.635 ppm and in figure 3.22 it is 1.6 ppm.

By now, all acetone and background signals were subtracted and any left over signals must be IPN only. These remaining signals were plotted against $C_{(t),IPN}$ in figure 3.23. They had linear correlation with IPN. Slopes of these line fits were the response factors or alpha values.

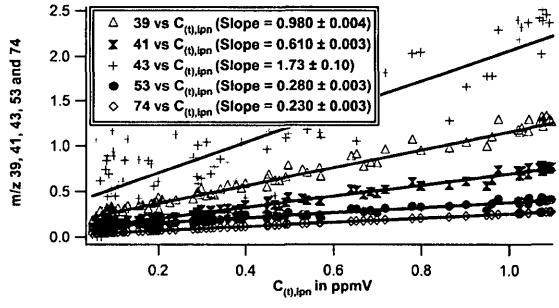

Figure 3.23: Linear correlation analysis of IPN fragments versus $C_{(t),\ IPN}$

These response factors are provided in table 3.10, along with the standard deviations in slope values.

Table 3.10. Alpha values for IPN fragments

m/z	*α (mV/ppm)*
39	0.980 ± 0.004
41	0.610 ± 0.003
43	1.730 ± 0.100
53	0.280 ± 0.003
74	0.230 ± 0.003

A linear correlation analysis was also performed between S_{74} and other IPN fragments, as

shown in figure 3.24. The slope values generated from figure 3.24 would be compared with the slope values obtained in isoprene oxidation experiment. IPN calibration spectrum is also provided in figure 3.25; it was obtained by plotting alpha values against the respective IPN fragments.

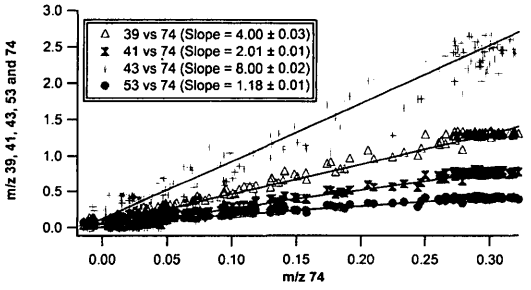

Figure 3.24: Linear correlation analysis of IPN fragments versus m/z 74

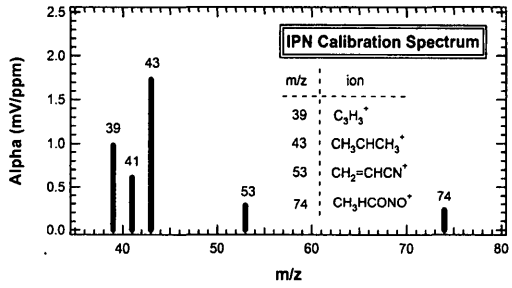

Figure 3.25: Calibration spectrum for IPN

The IPN fragments might be generated as follows:

$(CH_3)_2HCONO^+ \rightarrow CH_2{=}CH\text{-}C{\equiv}N^+ + 2H_2O$ reaction 3.7

IPN m/z **53**

$(CH_3)_2HCONO^+ \rightarrow C_3H_3^+ + H_2O + HNO + H$ reaction 3.8

IPN m/z **39**

$(CH_3)_2HCONO^+ \rightarrow CH_3HCONO^+ + CH_3$ reaction 3.9

IPN m/z **74**

$(CH_3)_2HCONO^+ \rightarrow CH_3CH\,CH_3^+ + NO_2$ reaction 3.10

IPN m/z **43**

Unusual fragmentations have been observed in the ion-trap previously, therefore m/z 53 and 39 are assumed to be these two species indicated above.

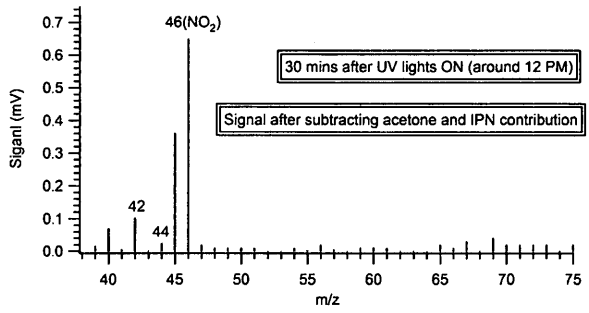

Figure 3.26: Signal after subtracting acetone and IPN contributions from overall signal

The IPN contribution from the overall signal was then removed. Figure 3.26 shows an example spectrum of anything left after subtracting acetone and IPN contributions from the overall signal, at 30 mins after UV lights on. It can be compared with figure 3.20, where the acetone contribution is removed only. The scale along y-axis is different in both figures.

Chapter 4: Isoprene oxidation

4.1: Introduction

OH radical initiated oxidation of isoprene was monitored in the smog chamber and peaks that demonstrated a significant change throughout the course of this reaction were examined. Information obtained by calibration spectra was used to identify and separate the fragment ions belonging to reactants or products.

4.2: Procedure

Purified air (300 cc/min) was admitted into the smog chamber and blank readings were taken for about 30 minutes. Then with 10 minute intervals between each injection, 150.0 μL of isoprene (a mixing ratio of 3.0 ppm), 150.0 μL of IPN (a mixing ratio of 2.9 ppm) and NO (a mixing ratio of 9.3 ppm) was admitted directly into the smog chamber. Everything was allowed to mix well with air for about 1hr and 10 mins, with UV lights off. Then turning on the UV lights resulted in photochemical production of OH radicals. OH radicals reacted with isoprene resulting in formation of methyl vinyl ketone and methacrolein; see section 4.10 for possible reactions.

Half of the UV lights were kept on and reaction was allowed to proceed for six hours, with one full scan mass spectrum obtained every minute. Then data collected was analyzed to generate time profiles of each of the fragments obtained, throughout the process. This would help us to identify the first generation products formed.

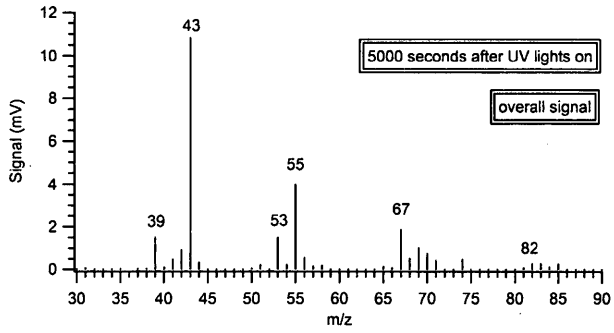

Figure 4.1: An example spectrum at 5000 seconds after UV lights on

Figure 4.1 provides an example spectrum of over all signals at one point that is 5000 seconds after UV lights on. Both reactants and products could be seen at this point.

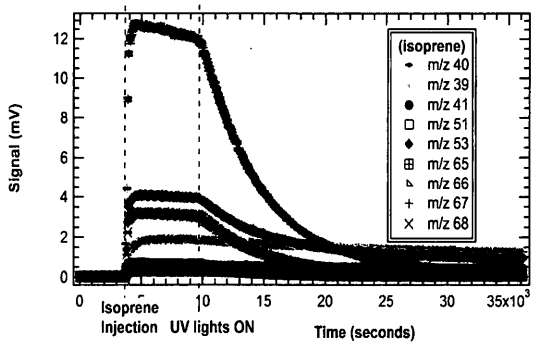

Figure 4.2: Time profiles of isoprene fragments

4.3: Time Profile of Isoprene Fragments

Isoprene fragments were identified from information obtained through isoprene calibration spectrum and plotted as a function of time in figure 4.2. M/z 67 had the highest signal intensity among all isoprene fragments. Thus a linear correlation analysis was performed between m/z 67 and other isoprene fragments, as shown in figure 4.3. Some of the fragments correlated with m/z 67, with zero intercepts. Those were m/z 50, 65, 66 and 68. M/z 51 also correlated with m/z 67, but with a non-zero intercept (0.03). Slope values generated from these correlations agreed with the slope values generated through the isoprene calibration spectrum.

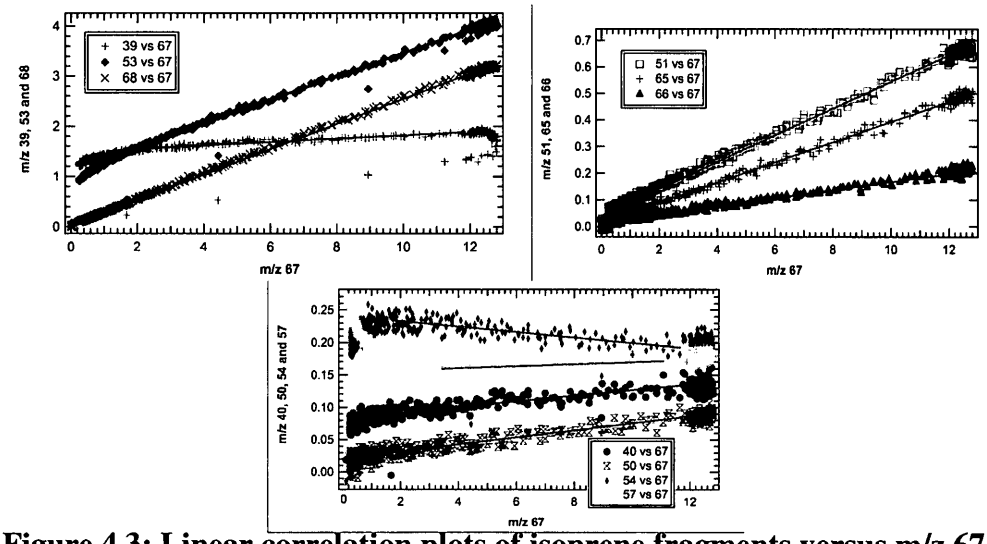

Figure 4.3: Linear correlation plots of isoprene fragments versus m/z 67

Slope values from figure 4.3 were then compared to the slope values obtained during the isoprene calibration experiment. Results are provided in table 4.1.

Table 4.1: Comparing slope values of linear correlation analysis of isoprene fragments

m /z	***Slopes (calibration spectrum) Base peak: m/z 67***	***Slopes (isoprene oxidation) Base peak: m/z 67***	***Comparison Result***	
39	0.0981 ± 0.0002	0.3410 ± 0.0004	Not straight line	Different
40	0.0085 ± 0.0001	0.0094 ± 0.0005	Not all points along fit of the line	Different
50	0.0064 ± 0.0001	0.0064 ± 0.0000	Straight line	Similar
51	0.0518 ± 0.0001	0.0518 ± 0.0001	Straight line	Similar
53	0.3003 ± 0.0010	0.5370 ± 0.0003	Not straight line	Different
54	0.0149 ± 0.0001	-0.0042 ± 0.0000	Not all points along fit of the line	Different
57	0.0101 ± 0.0001	0.0011 ± 0.0000	Not all points along fit of the line	Different
65	0.0386 ± 0.0002	0.0386 ± 0.0003	Straight line	Similar
66	0.0146 ± 0.0001	0.0146 ± 0.0000	Straight line	Similar
68	0.2480 ± 0.0010	0.2480 ± 0.0003	Straight line	Similar

M/z 39 and 53 were behaving differently when plotted against m/z 67. Data points were non-linear at these masses and correlated in small portions with m/z 67. Slope values were also large as compared to isoprene calibration experiment (table 4.1), an evidence of multiple species contributing at m/z 39 and 53.

M/z 40, 54 and 57 did not have all data points lying along the fit. M/z 57 correlated with m/z 67 only after UV lights were switched on, while m/z 54 had a negative correlation with m/z 67.

Slope values of multiple fragments agreed, based on fit quality, with the slope values from isoprene calibration experiment. Two of these were picked: m/z 67 and 68, one being the most stable fragment and the other being the molecular fragment of isoprene, respectively. Ratios of these fragments also agreed with ratios from isoprene calibration spectrum, thus m/z 67 and 68 belonged to isoprene only and they were used to calculate the concentration of isoprene changing with time, the $C_{(t),\ isop}$, using the formula:

$$S_{67,isop} = C_{(t),\ isop} \times \alpha_{(67,isop)} \qquad \text{Equation 4.1}$$

Where $\alpha_{(67,isop)}$ was the alpha value of m/z 67 generated through isoprene calibration experiment and $S_{67,isop}$ was the signal at m/z 67 changing with time. $C_{(t),isop}$ was again calculated using the signal at m/z 68, the $S_{68,isop}$ and an alpha value at m/z 68, the $\alpha_{(68,isop)}$. Concentrations of isoprene calculated from m/z 67 and 68 agreed (figure 4.4).

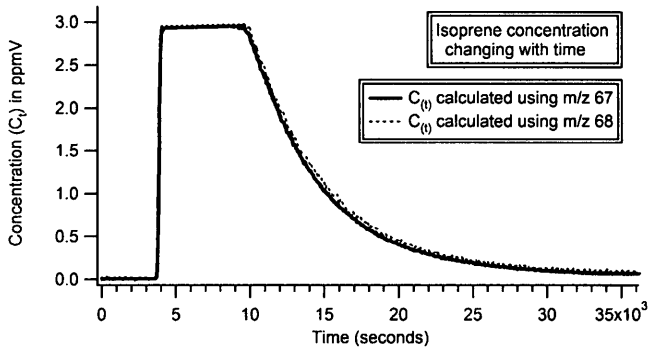

Figure 4.4: Concentration of isoprene ($C_{(t),\ isop}$) changing with time

The next step was to remove the isoprene contribution from the overall signal. Starting from m/z 39, the signal contribution of isoprene at m/z 39, the $S_{39,\ isop}$, was calculated using equation 4.2.

$$S_{39,\ isop} = C_{(t),\ isop} \times \alpha_{(39,\ isop)} \qquad \text{Equation 4.2}$$

Where $\alpha_{(39,isop)}$ is the response factor at m/z 39, from the isoprene calibration experiment. The $S_{39,\ isop}$ was then removed from overall signal of m/z 39, the S_{39}.

$$S_{39\text{-}isop} = S_{39} - S_{39,\ isop} \qquad \text{Equation 4.3}$$

Where, $S_{39\text{-}isop}$ is the left over signal, after removing the isoprene contribution. Repeating the same procedure, signal contributions of all other isoprene fragment were also removed. Figure 4.5 shows an example spectrum at 5000 seconds after UV lights on, having subtracted all the isoprene signal contribution. It can be compared with figure 4.1, which presents the overall signal at the same point.

Masses suspected to be contributed by isoprene only i.e. m/z 40, 50, 51, 65, 67 and 68 had nearly zero signals, at all times, after subtraction. Signal at m/z 40 was almost zero after subtraction. It was also an expected methacrolein fragment, from the MAC calibration experiment (see table 4.2); however a very low signal was left at m/z 40 after the isoprene contribution was removed from it. The appendix provides graphical presentation of before-and-after subtraction of isoprene contribution at m/z 40.

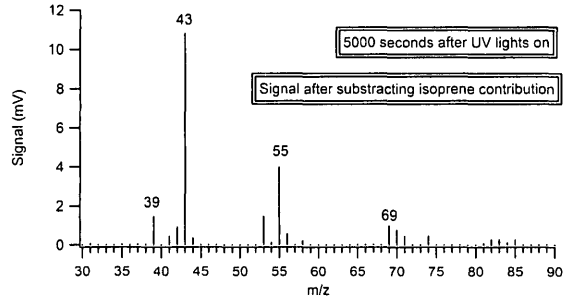

Figure 4.5: Signal after subtracting isoprene contribution from overall signal

4.4: Time Profiles of IPN

Previously, the IPN photolysis experiment had revealed that once the UV lights would turn on, all IPN fragments would be consumed by photolysis, while the signal for acetone fragments would increase gradually. Calibration spectra also revealed that m/z 74 was generated by IPN only. The other expected IPN fragments were m/z 39, 41, 43 and 53. They had substantial contributions from other compounds as well. Table 4.1 presents all the possible fragments of different species from calibration spectra.

Table 4.1. Possible fragments contributed by organic reactants and products of isoprene oxidation. Ions contributed solely by single species, are highlighted in bold text.

Organic specie	*Fragments contributed (m/z)*
Isoprene	39,40,41,**50**,**51**,53,54,57,**65**,**66**,**67**,**68**
IPN	39,41,43,53,**74**
Acetone	42,43,**44**,**58**
Methacrolein	39,40,41,42,53,**69**,70,**71**,**85**
Methyl vinyl ketone	39,41,42,43,53,**55**,**56**,70

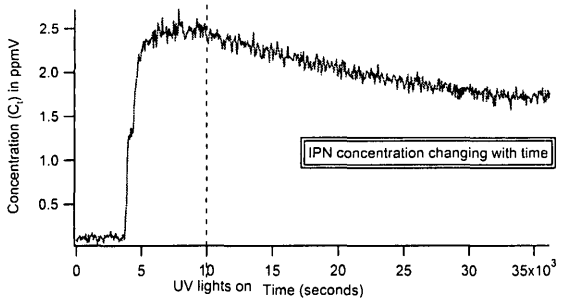

Figure 4.6: Concentration of IPN ($C_{(t),IPN}$) changing with time

Here we can see that m/z 74 was contributed by IPN only, so it was used to calculate $C_{(t),\,IPN}$, the concentration of IPN changing with time. It is presented in figure 4.6. The scale along x-axis presents time is seconds, as reaction was allowed to proceed for 9 hours and 44 minutes (35000 seconds). 2.9 ppm of IPN was injected from syringe; the maximum signal is approximately 2.65 ppm.

Using alpha values from the IPN calibration experiment, the signal contribution of IPN was determined and plotted as a function of time (figure 4.7). IPN fragments were not consumed completely and were still present at the end of the reaction. Figure 4.8 presents an example spectrum, at 5000 seconds after UV lights on, where IPN contribution is removed from the remaining overall signal. Figure 4.8 can be compared with figure 4.5. Figure 4.5 presents the overall signal, while figure 4.8 presents the signal remaining, after subtracting isoprene and IPN contributions from the overall signal. M/z 39, 41, 53 and 74 were almost gone.

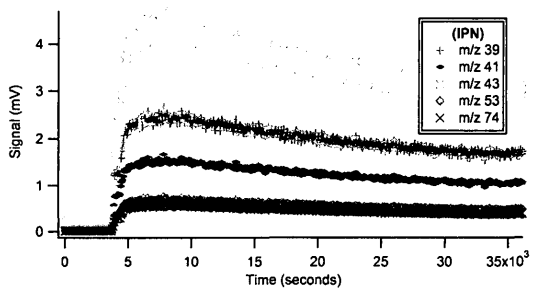

Figure 4.7: Time profile of IPN fragments

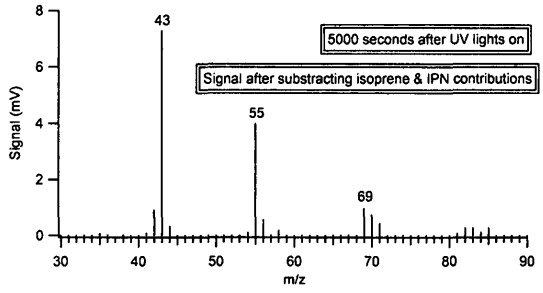

Figure 4.8: Signal after subtracting isoprene and IPN contributions from overall signal

M/z 39, 41 and 53 were supposed to be contributed by methacrolein and MVK as well (table 4.2). But when IPN contribution was removed from m/z 39 and 53, very small signals were left, as shown in appendix and anything left at m/z 41 was clearly being consumed. However, m/z 43 was still present, which might be contributed by products of this reaction.

4.5: Time Profile of Acetone

For acetone two fragments, m/z 44 and 58, were expected to be generated by acetone only. The ratio of these two fragments was found to be similar to what it was in the acetone calibration spectrum. It was a good indication that these fragments were from acetone only and they could be used to calculate concentrations of acetone, the $C_{(t),acet}$, using equation 4.1 and plotted as a function of time; in figure 4.9. Figure 4.9 revealed that concentration from m/z 44 and 58 agreed at all times. For subtraction of acetone contribution from the overall signal, the $C_{(t),acet}$ value obtained from m/z 58 was used.

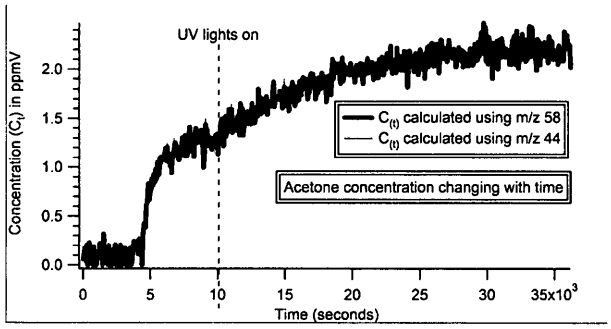

Figure 4.9: Concentration of acetone ($C_{(t),acet}$) changing with time

IPN consumed was plotted versus acetone produced after UV lights went on (figure 4.10).

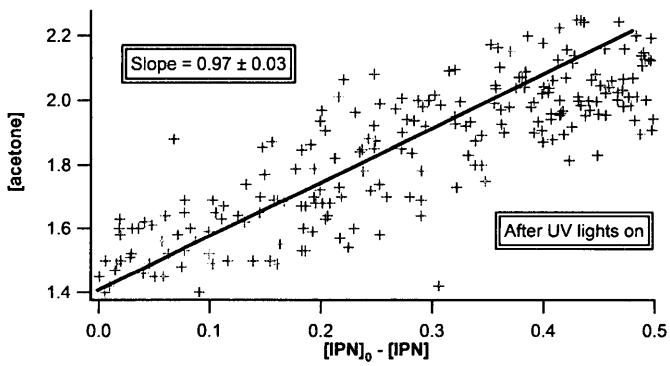

Figure 4.10: Acetone versus IPN consumed

The slope came out to be one, indicating that the analysis was done correctly. Alpha values of acetone fragments were obtained from the acetone calibration experiment and acetone contribution in the signal was plotted as a function of time (figure 4.11). This acetone contribution was then removed from the remaining overall signal.

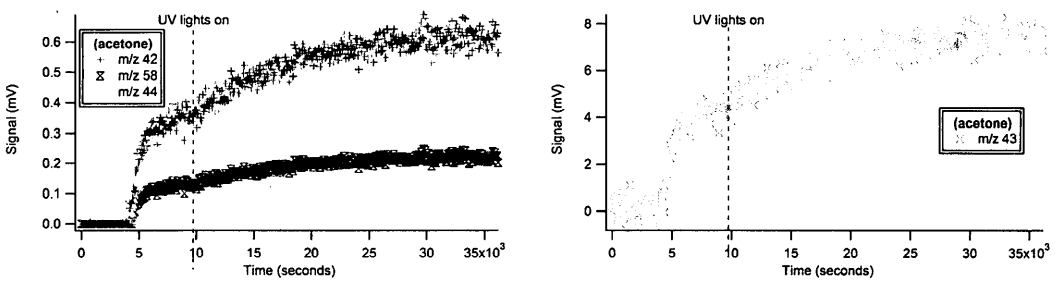

Figure 4.11: Time profile of acetone fragments

An example spectrum is provided in figure 4.12, at 5000 seconds after UV lights on. Signals at m/z 44 and 58 were completely removed after subtraction. However m/z 42 and 43 were still present. They might have contributions from other products of this reaction. It must be noted that now the scale along y-axis is much smaller than in the case of figure 4.8.

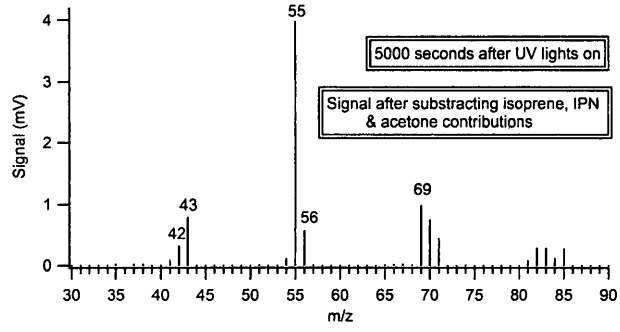

Figure 4.12: Signal after subtracting isoprene, IPN and acetone contributions from the overall signal

4.6: Time Profile of Methacrolein

Figure 4.13 shows the time profile of methacrolein fragments. Isoprene, IPN and acetone contributions from the overall signal had already been removed. A molecular ion peak at m/z 70 was formed rapidly after UV lights were turned on, as was m/z 85.

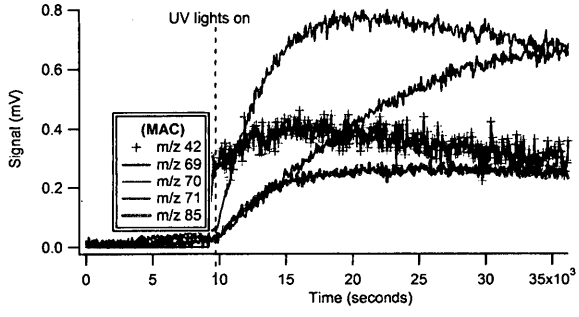

Figure 4.13: Time profile of Methacrolein fragments

Signal at m/z 70 was contributed by two species that is methacrolein and methyl vinyl ketone. However, there were two strong methacrolein fragments that were not contributed by MVK, m/z 69 and 85.

M/z 69 might have some isoprene contribution, but that had already been removed. The ratio of m/z 69 to 85 was found to be similar to the ratio of these two fragments from the methacrolein calibration spectrum. This was a good indication that both fragments were contributed by methacrolein only. M/z 69 and 85 were then used to calculate concentrations of methacrolein changing with time, the $C_{(t),\,MAC}$ (figure 4.14).

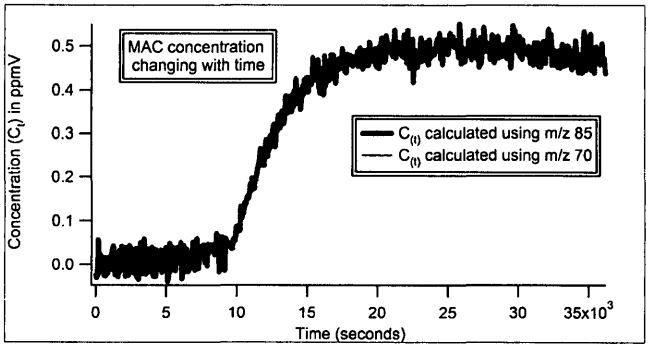

Figure 4.14: Concentration of MAC ($C_{(t),MAC}$) changing with time

Using alpha values from the MAC calibration spectrum, the signal contribution of methacrolein fragments was calculated and removed from the remaining overall signal. An example spectrum is provided in figure 4.15, at 5000 seconds after UV lights on.

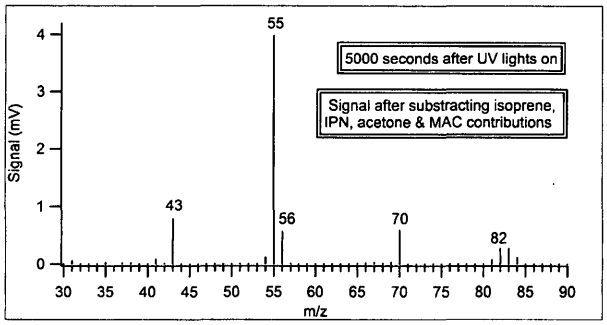

Figure 4.15: Signal after subtracting isoprene, IPN, acetone and MAC contributions from overall signal

Figure 4.14 can be compared with figure 4.5 (showing overall signal). Fragments suspected to be from methacrolein only i.e. m/z 69, 71 and 85 had essentially zero signals after subtraction.

4.7: Time Profile of Methyl Vinyl Ketone

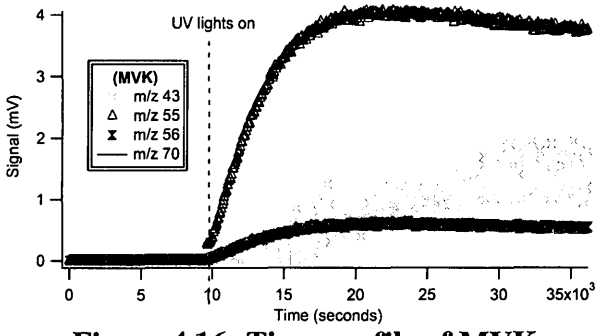

Figure 4.16: Time profile of MVK fragments

The expected MVK fragments from MVK calibration spectrum were m/z 39, 41, 42, 43, 53, 55, 56 and 70. Removing isoprene, IPN, acetone and methacrolein contributions, at these fragments, resulted in significant signals remaining at m/z 43, 55, 56 and 70. Signals at m/z 39 and 53 were very weak (as provided in appendix) and were not incorporated in the analysis. Time profile of MVK fragments is provided in figure 4.16. M/z 55 was the strongest signal. Linear correlation between m/z 55 and expected MVK fragments was analyzed, as shown in figure 4.17.

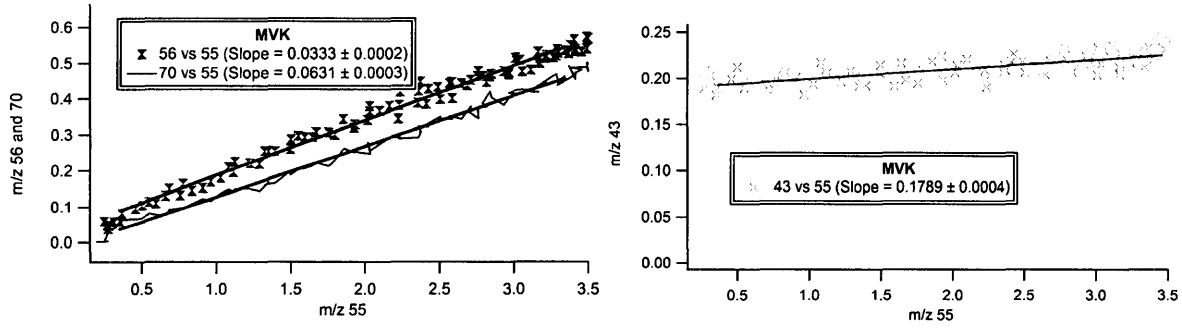

Figure 4.17: Linear correlation plots of expected MVK fragments versus m/z 55

Slope values obtained from this linear correlation analysis, were compared with the ones obtained in MVK calibration spectrum.

M/z 56 and 70 had similar slope values based on fit quality, while m/z 43 had different slope. The ratio between S_{56} and S_{55} was calculated and found to agree with the ratio from

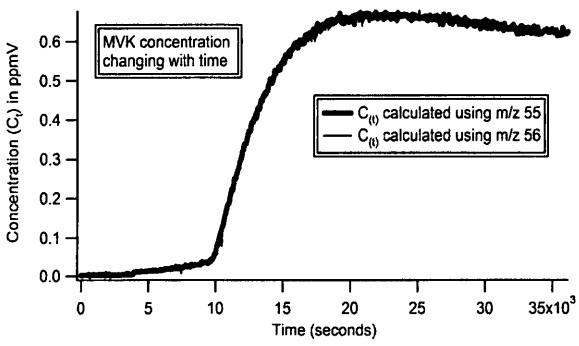

Figure 4.18: Concentration of MVK ($C_{(t),MVK}$) changing with time

the MVK calibration spectrum. From similar ratios and slope values it was concluded that both lines were contributed by MVK and both could be used to calculate concentration of MVK, as a function of time, provided in figure 4.18. Using $C_{(t),MVK}$ from figure 4.17 and alpha values from the MVK calibration experiment, the MVK signal contribution was calculated and removed from the remaining overall signal. Figure 4.19 shows an example spectrum, at 5000 seconds after UV lights on. It can be compared with figure 4.5 (indicating overall signal at 5000 seconds after UV on). Signal at m/z 55 and 56 were essentially zero after subtraction. A very low signal at m/z 70 was still present.

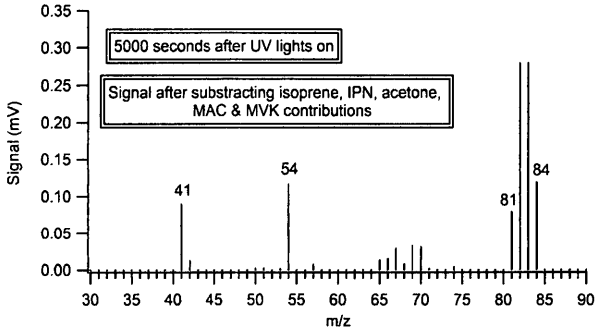

Figure 4.19: Signal after subtracting isoprene, IPN, acetone, MAC and MVK contributions from the overall signal

4.8: Time Profiles of left over Signals

Left over significant signals were observed at m/z 81, 82, 83 and 84. They are provided in figure 4.20. A linear correlation analysis was performed between these fragments. M/z 81 was

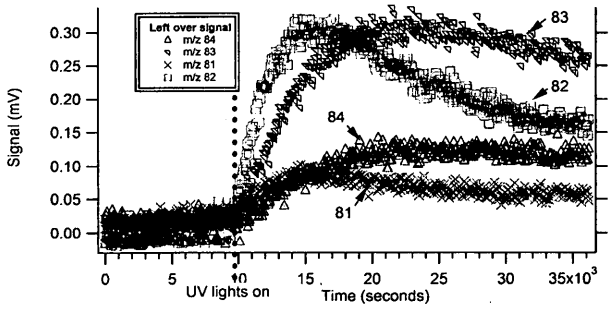

Figure 4.20: Time series of any signals left, after subtracting all known species

linearly correlated with m/z 82, while m/z 83 was linearly correlated with m/z 84 (figure 4.21). M/z 81 and 82 however showed poor linear correlation with m/z 83 and 84. All these appeared to be first generation fragments, as they were formed approximately at the same time as other first generation fragments were formed; that is, soon after the UV lights were turned on.

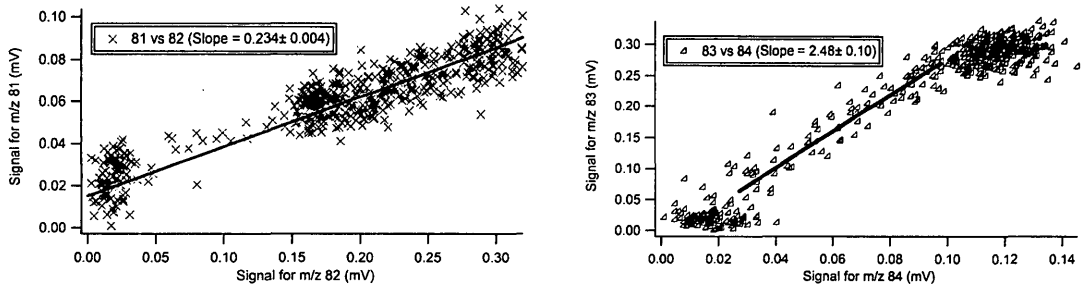

Figure 4.21: Linear correlation plots of left over signals

4.9: Time Profile of NO_2

Nitrogen dioxide was observed at m/z 46. It is evident from figure 4.22, that the signal at m/z 46 was low in IPN photolysis experiment, because NO was not injected and 1.3 ppm of IPN was admitted into the smog chamber. In isoprene oxidation experiment, 9.3 ppm of NO was admitted along with 3 ppm of IPN. Thus the amount of NO_2 generated was higher.

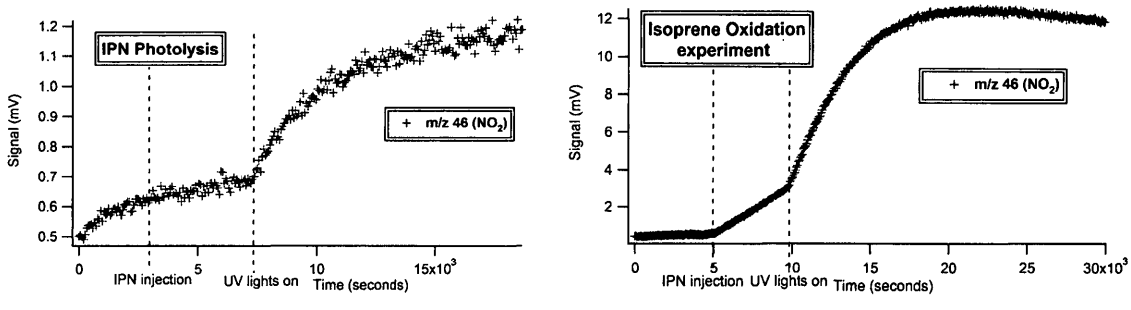

Figure 4.22: Time profile of NO_2 from IPN photolysis and isoprene oxidation

4.10: Overall Reactions

OH-radical can add to one of the four positions in isoprene, resulting in the formation of four possible hydroxyl alkyl radicals (called the allylic radicals). The next step in the oxidation process is O_2 addition to the carbon centers, either β or δ to the OH group, forming eight isomeric hydroxyl alkyl peroxy radicals ($RO_2^{\cdot}$).

These peroxy radicals ($RO_2^{\cdot}$) react with NO to form NO_2 and a variety of products, such as methyl vinyl ketone (MVK), methacrolein (MAC), formaldehyde (CH_2O) and ($HO_2^{\cdot}$) usually termed as either a hydroperoxyl radical or perhydroxyl radical.

Other reported first generation products of isoprene oxidation (not studied here) are 3-methyl furan, C_4-hydrocarbonyl, C_5-hydroxycarbonyl, hydroxynitrate and C_5-carbonyls (*Paulson*, 1992; *Miyoshi*, 1994; *Suzanne*, 1992; *Biesenthal*, 1997; *Lars*, 1999; *Jun*, 2003; *Woojin*, 2005; *Jesse*, 2006; *Paulot*, 2009; *Kourtchev*, 2005; *Richard*, 2006; *Magda*, 2006).

Formation of MVK

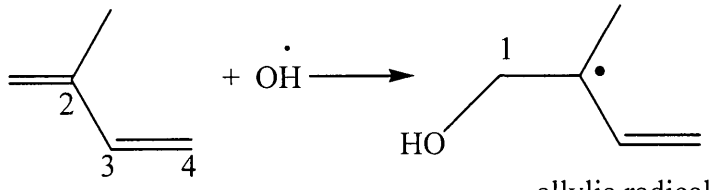

allylic radical

reaction 4.1

m/z **68**

2-methyl-1, 3-butadiene

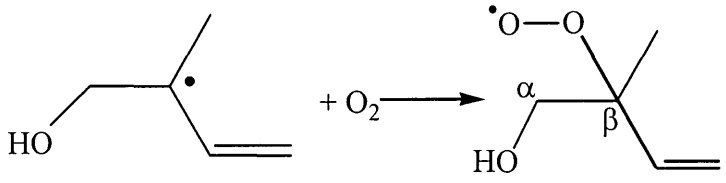

reaction 4.2

m/z **117** (RO_2)

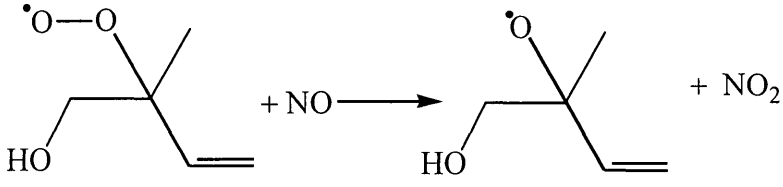

reaction 4.3

m/z **30** m/z **46**

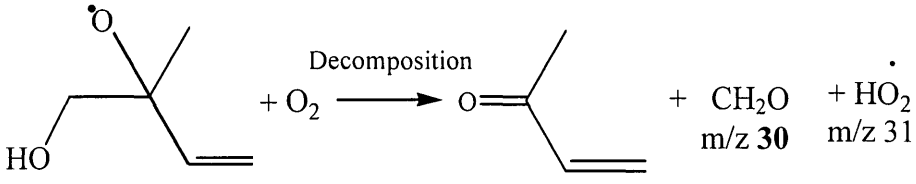

reaction 4.4

m/z **101** (RO) m/z **70** (MVK) m/z **30** Formaldehyde m/z 31 Perhydroxyl radical

Formation of Methacrolein

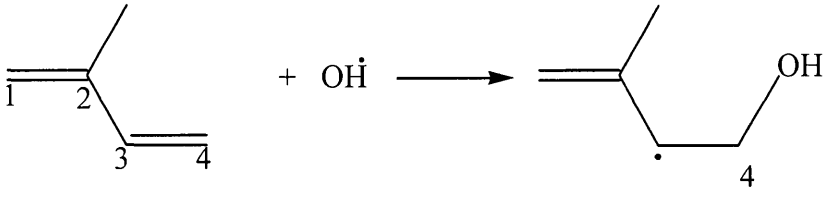

reaction 4.5

Isoprene m/z **68**

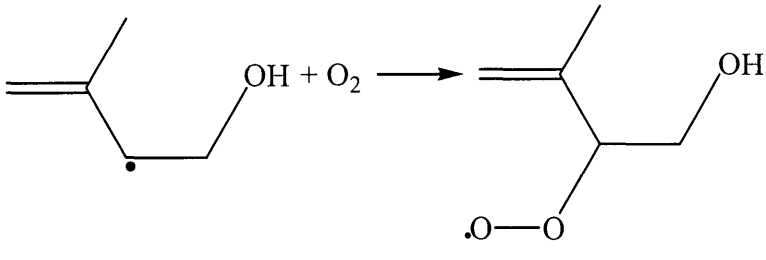

reaction 4.6

Hydroxyl alkyl radical Hydroxyl alkyl peroxy radical (RO_2)

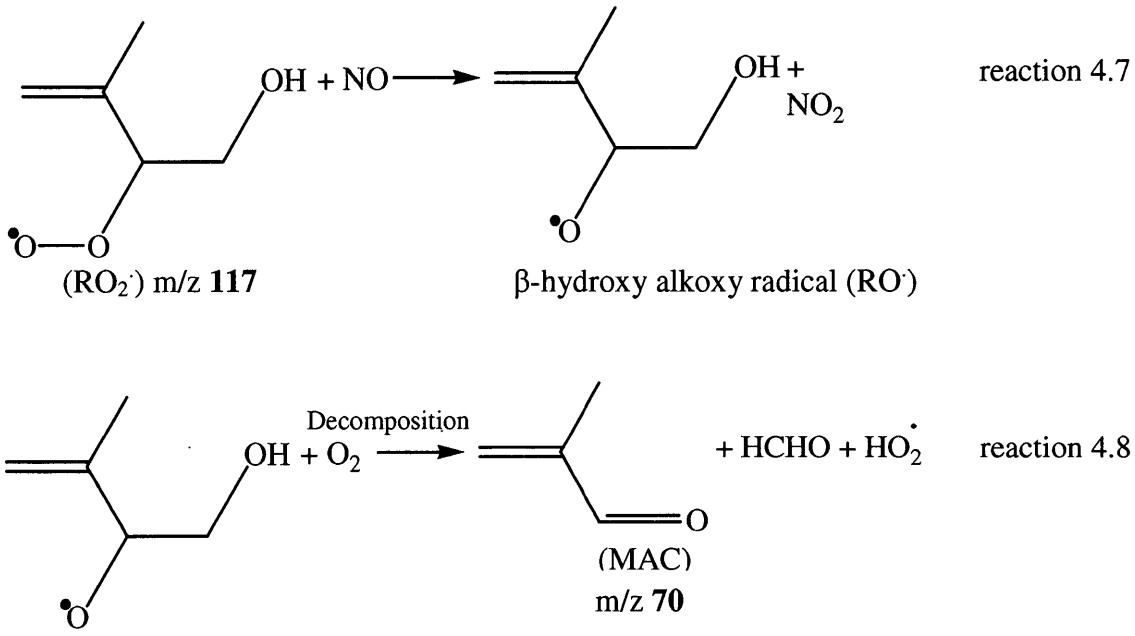

4.11: % yields of Methyl Vinyl Ketone and Methacrolein

With all concentrations known, percentage yields could also be calculated. MVK and MAC concentrations were plotted against the amount of isoprene consumed in figures 4.23 and 4.24, respectively.

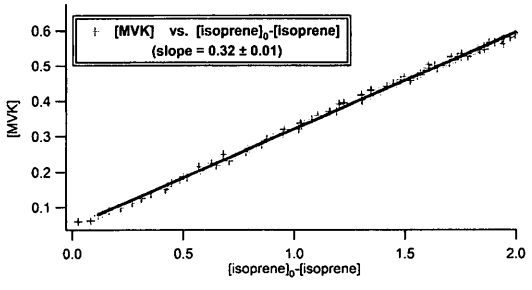

Figure 4.23: Plotting concentration of MVK against amount of isoprene consumed

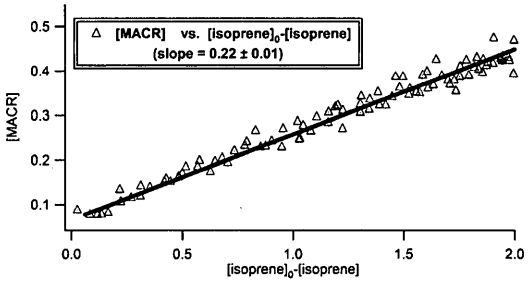

Figure 4.24: Plotting concentration of MAC against amount of isoprene consumed

In figures 4.23 and 4.24, the initial portion of the linear correlation (soon after the UV lights were turned on) was fitted and slope of this line fit when multiplied with 100, giving the percentage yields. Percentage yields for MVK and methacrolein were found to be 32% and 22% respectively. They were compared with previous studies, conducted under similar experimental conditions, in table 4.2.

Table 4.2. % yield from OH-radical initiated oxidation of isoprene measured during this work and reported in the literature, at high NO_x concentration

Product	*This work*	*Park et al. (2004)*	*Donahue et al. (2002)*	*Rupert et al. (2000)*	*Jenkins et al. (1998)*	*Miyoshi et al. (1994)*	*Paulson et al. (1992)*	*Tuazon et al. (1990)*
MAC	22	25.5	28	20	22.2	22	25	22
MVK	32	35.7	44	31	33.1	32	36	32

Percentage yields were in excellent agreement with several previous studies (*Jenkins, Miyoshi and Tuazon*). Results that differ are discussed briefly as follows.

Park et. al. (2004) reported different yields of MVK and MAC. They studied kinetics of isoprene-OH/OD reaction in the presence of O_2 and NO using laser photolysis/laser-induced fluorescence. Pressure and temperature-dependant rate constants for the addition of OH/OD to isoprene were found to be in good agreement with previous studies. However, percentage yield of MVK came out to be more than expected, from previously published literature. It was proposed that difference in yields resulted from OH-radical attachment to the internal carbon atoms of isoprene (instead of terminal ones). It leads to prompt $HO_2^{\cdot}$ production via ring cyclization, to produce hydroxy alkyl radicals ($RO^{\cdot}$). While other references provided in table 4.2, including this work, propose HO_2

production from OH-radical addition to the terminal carbon atoms of isoprene, which requires several intermediate steps (reactions are provided in section 4.10).

Donahue et al. (2002), reported oxidation mechanisms of isoprene initiated by OH-radical in the presence of NO under ''wall-less'' flowing conditions, with products observed a few seconds after reaction, by infrared spectroscopy. Experiments were conducted at room temperature (297 ± 3 K) at 750 torr pressure. Reaction mechanisms explained were similar to the previous studies, but higher yields were reported. These experiments were conducted in the high pressure flow reaction zone. Isoprene was introduced to the carrier gas flow (Ar) upstream of the reaction zone to assure a uniform concentration profile. OH-radicals were created using an H_2 microwave discharge followed by subsequent reaction of H with O_2. High levels of HO_2 were expected from this source; however, NO rapidly converted this HO_2 to OH-radical. As isoprene oxidation also produces HO_2, which regenerates the OH-radical via NO reaction, many molecules of isoprene were oxidized for each initial H atom. It was purposed that the higher oxidation resulted in the higher product yield.

Rupert et al. (2000), studied yields of methacrolein and MVK, from OH-radical initiated oxidation of isoprene at 180mbar (18000 Pa) partial pressure of oxygen. The other references provided in table 4.10, including this work, used standard conditions (one atmospheric pressure equal to 10^5 Pa) to study isoprene oxidation.

Paulson et al. (1992), studied OH-radical reaction with isoprene. Experiments were carried out in an outdoor smog chamber in an attempt to identify as completely as possible OH isoprene product distribution. A Tenax-based cryo-trap thermal desorber was used to trap, concentrate and dry chamber samples for identification on a GC/MS. Analysis of the products revealed that $O(^3P)$ can form in reaction systems designed to study OH-radical reactions that include high concentrations of NO and consequently NO_X. The reported yields were low because of the contribution of $O(^3P)$ atom reactions in the system used.

Chapter 5: Conclusion

The purpose of this research was to study the oxidation of isoprene and to determine percentage yields of its major first generation products. This required measuring low concentrations of reactants and products of isoprene oxidation in the smog chamber. However some of the heavier masses that we expected to see failed to show up or to have an expected intensity and clearly we couldn't trap heavier masses, especially m/z > 100. Therefore operating conditions were optimized, which resulted in extending the mass range that could be stored in the ion-trap from m/z 100 to m/z 140. Experiments performed to adjust for mass range proved that among all the ion-trap operating parameters, the *RF* potential seemed to have the greatest impact in trapping of heavier masses. Signal intensities were highest when gates were opened for a maximum period of time and minimum time was allowed for ion storage. In general, trapping of heavier masses compromised storage of lighter ones.

Calibration of equipment provided us with a reliable procedure which would help to track the sensitivity of mass spectrometer in future. For most stable fragments, sensitivity for toluene is 6mV/ppm (from figure 3.3). The sensitivity for isoprene is 4.1mV/ppm, for methacrolein it is 1.13mV/ppm, for methyl vinyl ketone it is 6mV/ppm and for acetone 5.4mV/ppm (from table 3.4). For IPN, sensitivity is 1.73mV/ppm (table 3.10). The detection limit for all these organic species is roughly 5 to 6 parts per billion (*v/v*) ranges.

To test limitations and capabilities of the mass spectrometer, the isoprene oxidation reaction was investigated. During the isoprene oxidation experiment, reactants injected in the smog chamber were isoprene, IPN, NO and O_2. The major first generation products obtained were methyl vinyl ketone and methacrolein.

In order to achieve quantitative results, calibration spectra were generated for isoprene and its oxidation products methacrolein and methyl vinyl ketone, providing us with reliable calculations of alpha values. IPN was used as an OH radical precursor. IPN photolysis was performed to generate calibration spectrum of IPN. These spectra revealed a large number of fragmentations by reactants and products.

For isoprene the most stable fragment was obtained at m/z 67. Other ions belonging to isoprene were m/z 50, 51, 65, 66, 67 and 68. No contribution of any other reactant and product of isoprene oxidation was observed at these fragments, making it easy to remove isoprene contribution from overall signal at these mass-to-charge ratios. Fragments at m/z 39, 40, 41, 53, 54 and 57 were contributed either by IPN or products of this reaction.

Fragmentation of methyl vinyl ketone revealed m/z 55 to be the most stable fragment. M/z 56 was also contributed by methyl vinyl ketone only, while m/z 39, 41, 42, 43, 53 and 70 being the expected methyl vinyl ketone fragments had contributions from reactants and other products of this reaction.

Similarly for methacrolein, m/z 69, 71 and 85 were contributed by methacrolein. The most stable fragment was obtained at m/z 70 and 39. However m/z 70 was also contributed by methyl vinyl ketone and m/z 39 was contributed by isoprene, IPN and methyl vinyl ketone, as well. All these signal contributions were removed from overall signals at any mass-to-charge ratios, using alpha values acquired through calibration spectra.

Identity of these m/z compounds could be addressed in future experiments. Alpha values or response factors generated through CSTR fitting of individual masses (in units of mV/ppm) helped to determine concentration of isoprene and its products as a function of time, during the oxidation process. Once the concentrations were known, signal contributions of both reactants and products were separated successfully. Time series of any signals left after subtracting all known species were also reported in section 4.8, for further investigation.

In the isoprene oxidation reaction, OH radicals reacted with isoprene in the presence of O_2 molecules to yield 32% of methyl vinyl ketone and 22% of methacrolein. The ratio of these two products was found to be consistent with previously published literature (table 4.2). This illustrated that instrument could be used both qualitatively and quantitatively to investigate kinetics of different reactions.

Future directions consist of additional measurements of other first generation products of isoprene oxidation, under different atmospheric conditions. A preliminary investigation

of second generation products and aerosol formation from isoprene oxidation would also be explored. As for sensitivity of the equipment, although much progress can be seen, it is low for masses above m/z 70, demonstrating a need of using other types of mass analyzers.

Chapter 6: References

Atkinson R., Gas-phase troposphere chemistry of organic compounds. *J. Phys. Chem. Ref. Data, 2*, 1994.

Atkinson R., Gas-phase troposphere chemistry of volatile organic compounds, alkanes and alkenes, *J. Phys. Chem. Ref. Data, 26*, 215-290,1997.

Apel E. C., D. D. Riemer, A. Hills and C. D. Geron, Measurement and interpretation of isoprene fluxes and isoprene, methacrolein and methyl vinyl ketone mixing ratios at the PROPHET site during the 1998 Intensive, *J. Geophys. Res., 107*, 4034, doi:10. 1029/2000 JD000225, 2002.

Armentrout P.B., Fundamentals of ion-molecule chemistry, *J. Anal. At. Spectrom. 19*, 571-580, 2004.

Arthur Fontijin and alberto J. Sabadell, Homogeneous Chemiluminescent measurement of nitric oxide with ozone, *Anal. Chem., 42,* 6, May 1970.

Barnard J.A., *Proc. R. Soc. London Ser. A, 279*, 236-248, 1964.

Benkelberg H., Seuwen, R., Product distribution of OH radical-induced oxidation of but-1-ene, methyl-substituted but-1-enes and isoprene in NOx free air. *Phys. Chem.* 4029-4039, 2000.

B. Rajakumara, Tomasz Gierczaka, Jonathan E. Flada, A.R. Ravishankaraa and James B. Burkholdera, The CH_3CO quantum yield in the 248 nm photolysis of acetone, methyl ethyl ketone and biacetyl B, *J. PhotoChem., 10*, 1060, 2008.

Brodbelt J.S., J.N. Louris and R.G. Cooks, Chemical ionization in an ion trap mass spectrometer, *Anal. Chem., 59*, 1278-1285, 1987.

Biesenthal T.A., J. W. Bottenheim and B. P. Shepson, The chemistry of biogenic hydrocarbons at the rural site in the Lower Fraser Valley. BC. *Atmospheric Environment 31*, 2049-2058, 1998.

Buddhadeb G., B. Alejandro, T. C. Brian and W. N. Simon, Isomer-Selective Study of the OH-Initiated Oxidation of Isoprene in the Presence of O_2 and NO: 2. The Major OH Addition Channel, *J. Phys. Chem. A, 114,* 2553–2560, 2010.

Carlton A. G., C. Wiedinmyer and J. H. Kroll, A review of Secondary Organic Aerosol (SOA) formation from isoprene, *Atmos. Chem. Phys., 9*, 4987–5005, 2009.

Chambers A., *Modern Vacuum Physics*, CRC Press, Boca Raton, FL, Especially chapters

1-3; sections 4.4 & 4.5; chapter 5; sections 6.1, 6.2.1, 6.3.1, 6.3.2, 6.3.3, 7.1, 7.3, 7.5, 2005.

Chambers D.M., L.I. Grace and B.D. Andersen, Development of an ion trap store/time-of-flight mass spectrometer for the analysis of volatile compounds in air, *Anal. Chem., 69*, 3780-3790, 1997.

Campuzano-Jost P. and M. B. Williams, Kinetics of the OH-initiated oxidation of isoprene, *Geophys. Res. Lett., 27*, 693-696, 2000.

Chen X., D. Hulbert, and P. B. Shepson, Measurement of the organic nitrate yield from OH reaction with isoprene, *J. Geophys.,103*, 25, 563–25,568, 1998.

Chien B.M., S.M. Michael and D.M. Lubman, The design and performance of an ion trap storage reflectron time-of-flight mass spectrometer, *Int. J. Mass. Spectrom. Ion Processes, 131*, 149-179, 1994.

Claeys M., W. Wang, A.C. Ion, I. Kourtchev, A. Gelencser and W. Maenhaut, Formation of secondary organic aerosols from isoprene and its gas-phase oxidation products through reaction with hydrogen peroxide, *Atmos. Environ., 38*, 4093–4098, 2004 (a).

Claeys M., Formation of secondary organic aerosols through photo oxidation of isoprene, *Science, 303*, 1173–1176, 2004 (b).

Coggon P., A. T. McPhail, G. A. Sim, A Randomly Labeled Tropylium Ion in the Mass Spectrum of Toluene-α, 1-$^{13}C_2^1$, *Journal of the American Chemical Society*, May 22, 1968.

Cotter R. J., *Time-of-Flight Mass Spectrometry: Instrumentation and Applications in Biological Research*, ACS, Washington, Chapters 1-3., 1997.

Daven K. Henze and John H. Seinfeld, Global secondary organic aerosol from isoprene oxidation, *geophysical research letters*, vol. 33, L09812, 2006.

Ding X., M. Zheng, L. P. Yu, X. L. Zhang, R. J. Weber, B. Yan, A. G. Russell, E. S. Edgerton and Wang, X. M., Spatial and seasonal trends in biogenic secondary organic aerosol tracers and water-soluble organic carbon in the southeastern United States, *Environ. Sci. Technol., 42*, 5171–5176, 2008.

Edney E. O., T. E. Kleindienst, M. Jaoui, M. Lewandowski, Offenberg, W. Wang and Claeys, Formation of 2-methyl tetrols and 2-methylglyceric acid in secondary organic aerosol from laboratory irradiated isoprene/NOx/SO_2/air mixtures and their detection in ambient PM 2.5 samples collected in the eastern United States, *Atmos. Environ., 39*, 5281–5289, 2005.

Eldering A. and G. R. Cass, Source-oriented model for air pollutant effects on visibility, *J. Geophys. Res., 101(D14)*, 19, 343-369, 1996.

Fehsenfeld, F., J. Calvert and Fall, R., Golden, Emissions of volatile organic compounds from vegetation and the implications for atmospheric chemistry, *Global Biogeochemical Cycles 6,* 389-430, 1992.

G.C. Stafford and Jr. P.E. Kelley, Recent improvements in and analytical applications of advanced ion-trap technology, *Int. J. Mass. Spectrom. Ion Processes, 60*, 85-98, 1984.

Ghan S. J. and S. E. Schwartz, Aerosol properties and processes, a path from field and laboratory measurements to global climate models, *AMS*, 1059-1083, 2007.

G´omez-Gonz´alez, Y. Surratt, J. D. Cuyckens, F. Szmigielski, R. Vermeylen, R. Jaoui, M. Lewandowski, M. Offenberg, J. H. Kleindienst, T. E. Edney, E. O. Blockhuys, F. Van Alsenoy, C. Maenhaut and W. Claeys, M. Characterization of organosulfates from the photo oxidation of isoprene and unsaturated fatty acids in ambient aerosol using liquid chromatography/(-)electrospray ionization mass spectrometry, *J. Mass Spectrom., 43*, 371–383, 2008.

Griffin R. J., D. R. Cocker, R. C. Flagan and J. H. Seinfeld, Organic aerosol formation from the oxidation of biogenic hydrocarbons, *J. Geophys. Res.*, *104*, 3555–3567, 1999 (a).

Griffin R.J., D.R Cocker, J. H. Seinfeld and Dabdub, Estimate of global atmospheric organic aerosol from oxidation of biogenic hydrocarbons, *Geophys. Res.Lett.*, *26*, 2721–2724, 1999 (b).

Guenther A., C.N. Hewitt, D. Erickson, R. Fall, C. Geron, T. Graedel, P. Harley, L. Klinger, M. Lerdau, T. Pierce., B. Scholes, R. Steinbrecher, R. Tallamraju, Taylor and Zimmerman, A global model of natural organic compound emissions. *J. Geophys. 100*, 8873-8892, 1995.

Guenther A., A global-model of natural volatile organic compound emissions,*J.Geophys. Res.*, *100*, 8873–8892, 1995.

Guenther A., T. Karl, P. Harley, C. Wiedinmyer, P.I. Palmer and Geron, Estimates of global terrestrial isoprene emissions using MEGAN (Model of Emissions of Gases and Aerosols from Nature), *Atmos. Chem. Phys. Discuss.*, *6*, 107–173, 2006.

Hagerman L. M., A.P. Aneja and W. A. Lonneman, Characterization of non-methane hydrocarbons in the rural southeast United states. *Atmospheric Environment 31*, 4017-4038, 1997.

Heald C. L., D. J. Jacob, R. J. Park, L. Russell, B. J. Huebert, J.H. Seinfeld, Liao and R. J. Weber, A large organic aerosol source in the free troposphere missing from current models, *Geophys. Res. Lett.*, *32,* 2005.

Henze D. K. and J.H. Seinfeld, global secondary organic aerosol from isoprene oxidation, *Geophys. Res.* Lett., 33 L09812, doi:10. 1029/2006 GL025976, 2006.

Holzinger R., A. Lee, K.T. Paw and A.H. Goldstein, Observations of oxidation products above the forest imply biogenic emissions of very reactive compounds, *Atmospheric chemistry and Physics* 5, 67-75, 2005.

Ho Jinlim and C. Annmarieg, Isoprene Forms Secondary Organic Aerosol through Cloud Processing: Model Simulations, *Environ. Sci. Technol., 39,* 4441-4446, 2005.

Ion, A. C., R. Vermeylen, I. Kourtchev, J. Cafmeyer, X. Chi, A. Gelencs´er, Maenhaut and M. Claeys, Polar organic compounds in rural PM 2.5 aerosols from K-puszta, Hungary, during a 2003 summer field campaign: Sources and diel variations, *Atmos. Chem. Phys., 5,* 1805–1814, 2005.

Inman R. C. and Jr. E. Voigtman, Calibration curve preparation of analytes in liquids solutions by means of exponential dilution flask, Department of chemistry, university of Florida, *Applied spec,* 36, 2, 1982.

Jiho Park, Candice G. Jongsma, Renyi Zhang and Simon W. North, OH/OD Initiated oxidation of Isoprene in the Presence of O_2 and NO, *J. Phys. Chem. A, 108,* 10688-10697, 2004.

Jonscher K.R. and John R. Yates, the Quadrupole Ion Trap Mass Spectrometer A Small Solution to a Big Challenge, *Anal. Biochem. 244,* 1–15, 1997.

Jordan ToF products, Inc. TOF fundamentals tutorial, *www.rmjordan.com,* 990 Golden Gate Terrace, CA.

Jodie V. Johnson, Randall E. Peddeer, Richard A. Yost and R. E. March, the stretched quadrupole ion trap: Implications for the Mathieu a_u and q_u parameters and experimental mapping of the stability diagram, *Wiley Interscience*; New York, 6, 760-764, 1992.

Jun Zhao, Renyi Zhang and Simon W. North, Quantification of hydroxycarbonyl from OH-isoprene reactions, *J. AM. Chem. Soc. 126,* 2686-2687, 2004.

Kebarle P., Gas phase ion chemistry based on ion-equilibria: From the ionosphere to the reactive centers of enzymes, *Int. J. Mass Spectrom., 200,* 313-330, 2000.

Khayamian T., M.Tabrizchi and N.Taj, Direct determination of ultra-trace amounts of acetone by corona-discharge ion mobility spectrometer, *J Anal Chem, 370,* 1114-1116, 2001.

Kleindienst T. E., Edney, J.H. Offenberg and M. Jaoui, Secondary organic carbon and aerosol yields from the irradiations of isoprene and pinene in the presence of NOx

and SO_2, *Environ. Sci. Technol., 40*, 3807–3812, 2006.

Kleindienst T. E., M. Jaoui, M. Lewandowski and Edney, Estimates of the contributions of biogenic and anthropogenic hydrocarbons to secondary organic aerosol at a southeastern US location, *Atmos. Environ., 41*, 8288-8300, 2007a.

Kleindienst T. E., M. Lewandowski, J. H. Offenberg and E. O Edney, Ozone-isoprene Reaction, Re-examination of the formation of secondary organic aerosol, *Geophys. Res. Lett., 34*, L01805, doi: 10.1029/2006GL027485, 2007b.

Kroll J. H., N. L. Ng, S. M. Murphy, R. C. Flagan and J. H. Seinfeld, Secondary organic aerosol formation from isoprene photooxidation under high-NO*x* conditions, *J. Geophys.Res. Lett., 32*, L18808, doi:10.1029/2005GL023637, 2005.

Kroll J. H., N. L. Ng, S. M. Murphy, R. C. Flagan and J. H. Seinfeld, Secondary organic aerosol formation from isoprene photo oxidation, *Environ. Sci. Technol., 40*, 1869–1877, doi:10.1021/es0524301, 2006.

Kwok E. S. C., R. Atkinson and J. Arey, Observation of hydroxycarbonyls from the OH radical-initiated reaction of isoprene, *Environ. Sci. Technol., 29(9)*, 2467–2469, 1995.

Lamb B., D. Gay, Westberg and H., Pierce, A biogenic hydrocarbon emission inventory for the USA using a simple forest canopy model, *Atmospheric Environment 27A*, 1673-1690, 1993.

Lars Rupert and Karl H. Becker, A product study of the OH radical-initiated oxidation of isoprene: formation of C_5-unsaturated diols, *Atmospheric Environment 34*, 1529-1542, 2000.

Lee L.M., Baasandorj and P. S. Stevens, Monitoring OH-initiated oxidation kinetics of isoprene and its products using online mass spectrometry, *Environ. Sci. Technol., 39*, 1030-1036, 2005.

Lindner E., Gyurcsányi and R. Buck, Tailored transport through ion selective membrane for improved detection limits and selectivity coefficients, *Wiley Interscience*; Electro analysis, 1999.

March R.E., An introduction to quadrupole mass spectrometry, *J. Mass. Spectrom., 32*, 351-169, 1997.

March R.E., R.J. Hughes and J.F.J. Todd, Quadrupole Storage Mass Spectrometry, *Wiley Interscience*; New York, 1989.

March R.E. and J.F. Todd, Quadrupole Ion Trap Mass Spectrometry, 2nd ed., *Wiley Interscience*; New York, 2005.

Matsunaga S., M. Mochida and K. Kawamura, Growth of organic aerosols by biogenic

semi-volatile carbonyls in the forestal atmosphere, *Atmos. Environ.*, *37*, 2045–2050, 2003.

McKeen S. A., Photochemical modeling of hydroxyl and its relationship to other species during the Tropospheric OH Photochemistry Experiment, *J. Geophys., 102*, 6467–6493, 1997.

Michael S.M., M. Chien and D.M. Lubman, An ion trap storage/time-of-flight mass spectrometer, *Rev. Sci. Instrum., 63*, 4277-4284, 1992.

Miyoshi A. and S. Hatakeyama, OH radical-initiated photo oxidation of isoprene: An estimate of global CO production, *J. Geophys, Res., 99*, 18, 779-18, 787, 1994.

Müller J.F., Geographical distribution and seasonal variation of surface emissions and deposition velocities of atmospheric trace gases. *Journal of Geophysical Research 97*, 3787-3804, 1992.

Neil Donahue and James Anderson, Product analysis of the OH oxidation of isoprene and 1,3-butadiene in the presence of NO, *Geophys. Res.*, *107*, D15, 4268, doi: 10.1029/ 2001JD000716, 2002.

Ng N. L., A. J. Kwan, J. D. Surratt, A. Chan, P. S. Chhabra, Sorooshian, J. D. Crounse and Seinfeld J. H., Secondary organic aerosol (SOA) formation from reaction of isoprene with nitrate radicals (NO_3), *Atmos. Chem. Phys., 8,* 4117–4140, 2008.

O'Hanlon, *A User's Guide to Vacuum Technology*, 3rd ed., Wiley, 2003.

Ontario, Air quality in Ontario: 2002 Report. Ministry of the Environment, Toronto, 2002.

Operando, FTIR study of the photocatalytic oxidation of acetone in air over TiO_2–ZrO_2, *Thin films catalysis today, 143* (3-4), pg. 364-373, May 2009.

Paulson S. E. and R. C. Flagon, Atmospheric photo oxidation of isoprene part I: The hydroxyl radical and ground state atomic oxygen reactions, *Int. J. Chem., 24*, 79-101, 1992.

Plewka A., T. Gnauk, E. Bruggemann and H. Herrmann, Biogenic contributions to the chemical composition of airborne particles in a coniferous forest in Germany, *Atmos. Environ., 40*, 103–115, 2006.

Press W. H., S. A. Teukolskwy, T. Vetterlinga and B. P. Flannery, Numerical recipes in Fortran 77, The Art of Scientific Computing, *Cambridge Univ. Press*, *1*, 1996.

Randall E. Pedder, Practical Quadrupole Theory: Graphical Theory, *ABB Inc., Analytical-QMS Extrel Quadrupole Mass Spectrometry*, 575 Epsilon Drive, Pittsburgh, PA 15238.

Richard Iannone and J. Rudolph, $^{12}C/^{13}C$ kinetic isotope effects of the gas-phase reactions of isoprene, methacrolein, and methyl vinyl ketone with OH radicals, 2009.

Robert Bereczki, Boglarka takacs and Jan Lansmaier, How to assess the limits of ion-selective electrodes: Methods for the determination of the ultimate span, response range, and selectivity coefficients of neutral carrier-based cation selective electrodes, *Anal. chem., 78*, 942-950, 2006.

Roberts J. M. and J. Williams, Measurements of PAN, PPN, and MPAN made during the 1994 and 1995 Nashville intensives of the Southern Oxidant Study: implications for regional ozone production from biogenic hydrocarbons. *Journal of Geophysical Research 103*, 22473-22490, 1998.

Ritter J. J. and N. K. Adams, Exponential Dilution as a Calibration Technique, *Inorganic Chemistry Section*, National Bureau of Standards, Washington, D.C. 20234

Schlesinger R. B. and F. Cassee, Atmospheric secondary inorganic particulate matter: The toxicological perspective as a basis for health effects risk assessment, *Inhalation Toxicology, 15*, 3, 197-235, 2003.

Schoon N., C. Amelynck, L. Vereecken, H. Coeckelberghs and E. Arijs, A selected ion flow tube study of the reactions of H_3O^+, O_2^+ and NO^+ with some monoterpene oxidation products, *Int. J. Mass Spectrom., 239*, 7-16, 2004.

Staffelbach T., A. Neftel, A. Blatter, A. Gut, M. Fahrni, J. Stahelin, A. Prevot, A. Hering and Lehning, Photochemical oxidant formation over southern Switzerland. Results from summer 1994, *Journal of Geophysical Research 102*, 23345-23362,1997.

Starn T.K., P. B. Shepson and Bertman, Observations of isoprene chemistry and its role in ozone production at a semirural site during 1995 Southern Oxidants Study. *Journal of Geophysical Research 103*, 22425-22435, 1998.

Suzanne E. Paulson and John H. Seinfield, Development and evaluation of a Photo oxidation mechanism for isoprene, *Journal of geophysical research*, vol 97, 703-715, 1992.

Surratt J. D., S. M Murphy, J. H. Kroll, L. Ng Sorooshian, A. Szmigielski, R. Vermeylen, M. Claeys and J. H. Seinfeld, Chemical composition of secondary organic aerosol formed from the photooxidation of isoprene, *J. Phys. Chem. A, 110*, 9665–9690, 2006.

Surratt J. D., J. H. Kroll, Kleindienst, Edney, E. O. Claeys, M. Sorooshian, A. Ng, N. L. Offenberg, J. H. Lewandowski, M. Jaoui, M. Flagan and J. H. Seinfeld, Evidence for organosulfates in secondary organic aerosol, *Environ. Sci. Technol., 41*, 517–527,

2007a.

Surratt J. D., M. Lewandowski, J. H. Offenberg, M. Jaoui, Kleindienst, E. O. Edney, and J. H. Seinfeld, Effect of acidity on secondary organic aerosol formation from isoprene, *Environ. Sci. Technol., 41*, 5363–5369, 2007 b.

Tuazon E. C. and R. Atkinson, A product study of the gas-phase reaction of isoprene with the OH radical in the presence of NOx, *Int. J. Chem. Kinet., 22*, 1221-1236, 1990.

Volkamar R., L.T Molina, M.J. Molina, T. Shirley and Brune, DOAS measurement of glyoxal as an indicator for fast VOC chemistry in urban air, *Geophys. Res. Lett., 32*, 2005.

Wang T., P. Spanel and D. Smith, Selected ion flow tube, SIFT, studies of the reactions of H_3O^+, O_2^+ and NO^+ with eleven $C_{10}H_{16}$ monoterpenes, *Int. J. Mass Spectrom., 228*, 117-126, 2003.

Wang W., I. Kourtchev, B. Graham, J. Cafmeyer and M. Claeys, Characterization of oxygenated derivatives of isoprene related to 2-methyltetrols in Amazonian aerosols using trimethylsilylation and gas chromatography/ion trap mass spectrometry, Rapid Commun. *Mass Sp., 19*, 1343–1351, 2005.

Wilson P.F., C.G. Freeman and M.J. McEwan, Reactions of small hydrocarbons with H_3O^+, O_2^+ and NO^+ ions, *Int. J. Mass Spectrom., 229*, 143-149, 2003.

Winter R and P. G. Nixon, Perflurinated polymer surfaces comprising SF_5-terminated long chain perfluoroacrylate. *J. Fluorine Chem.*, 115, 107, 2005.

Woojin Lee, M. Paasandorj and Philip S. Stevens, Monitoring OH-initiated oxidation kinetics of isoprene and its products using online mass spectrometry, *Environmental Science & Technology, 39*, No. 4, 2005.

Xia X. and P. K. Hopke, Seasonal variation of 2-methyltetrols in ambient air samples, *Environ. Sci. Technol., 40*, 6934–6937, 2006.

Yu J., H. E. Jeffries and R. M. Lacheur, Identifying airborne carbonyl compounds in isoprene atmospheric photooxidation products by their PFBHA oximes using gas chromatography/ion trap mass spectrometry, *Environ. Sci. Technol., 29(8)*, 1923–1932, 1995.

Appendix : Total and Residual Ion Counts

Isoprene oxidation was carried out in a smog chamber, where reactants [isoprene, isopropyl nitrite (IPN) and nitrogen oxide] were introduced in the flow of purified air. Reactants were allowed to mix, before UV lights were switched on, at 10,000 seconds. UV triggered the photochemical production of OH radicals and acetone, from IPN.

Subsequent oxidation reaction between isoprene and OH radicals generated methyl vinyl ketone (MVK) and methacrolein (MAC). Concentration-time profiles of reactants and products were monitored by an ion-trap, time of flight mass spectrometer. A detailed description is provided in chapter 4.

The experiment resulted in a complex mass spectrum of signals versus reaction time, for ions produced by many different fragments of different species. For convenience, mass spectra of all ions would be displayed, separately.

The total ion count at any mass-to-charge (m/z) ratio would be the mass spectrum of overall signal obtained against the reaction time in smog chamber. The residual ion count would be obtained by removing or subtracting the contribution of reactants or products from that ion. These residual signals would be plotted separately to demonstrate the results more clearly. Generally, along the vertical axis, solid lines would depict the overall signals or signals being subtracted; while markers (+) would indicate the residual signals (after subtraction). Reaction time would be plotted along the horizontal axis, in units of seconds.

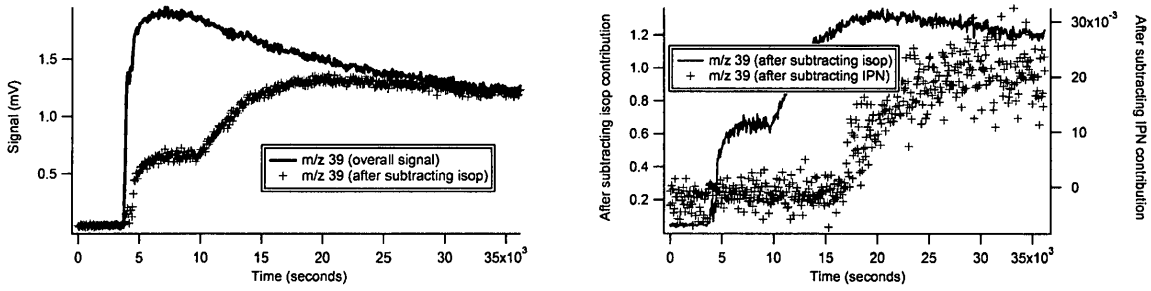

(a) (b)

Figure 1: Mass spectrum of m/z 39
a. Total ion count of m/z 39 (solid red line) and residual ion count of m/z 39 after subtraction of isoprene (black markers (+)).
b. Left hand side along y-axis is the residual ion count of m/z 39 after subtraction of isoprene ((solid red line) note that it's the same signal presented by black markers in (a). Right hand side along y-axis (with different scale) is the residual ion count of m/z 39 after subtraction of isoprene and isopropyl nitrite (IPN) [black markers (+)].

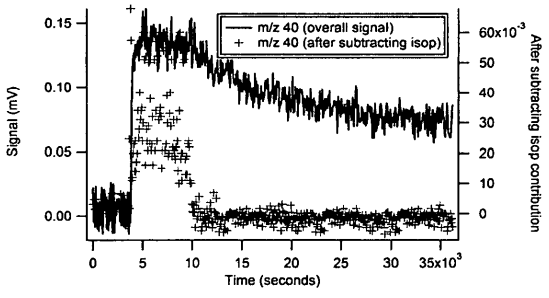

Figure 2: Mass spectrum of m/z 40
Left hand side along y-axis: total ion count of m/z 40 (solid blue line). Right hand side along y-axis: residual ion count of m/z 40 after subtraction of isoprene (black markers (+)), determined that m/z 40 is a pure isoprene fragment.

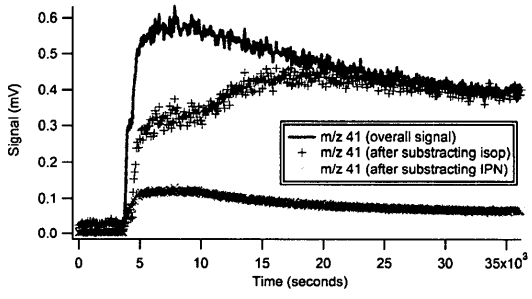

Figure 3: Mass spectrum of m/z 41
Total ion count of m/z 41 (solid dirty green line) and residual ion count of m/z 41 after subtraction of isoprene and isopropyl nitrite (IPN) (black markers (+)) which might be a minor product.

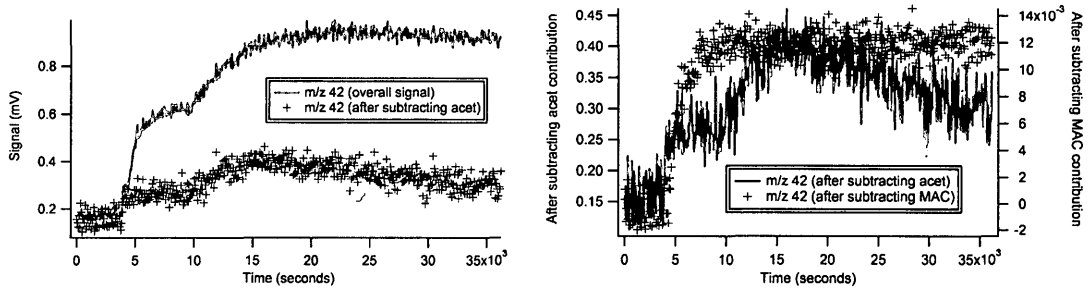

(a) (b)

Figure 4: Mass spectrum of m/z 42

a. Total ion count of m/z 42 (solid red line) and residual ion count of m/z 42 after subtraction of acetone (black markers (+)).

b. Left hand side along y-axis is the residual ion count of m/z 42 after subtraction of acetone ((solid red line) note that it's the same signal presented by black markers in (a). Right hand side along y-axis is the residual ion count of m/z 42 after subtraction of acetone and methacrolein (MAC) [black markers (+)], indicating presence of reactants in the remaining signal.

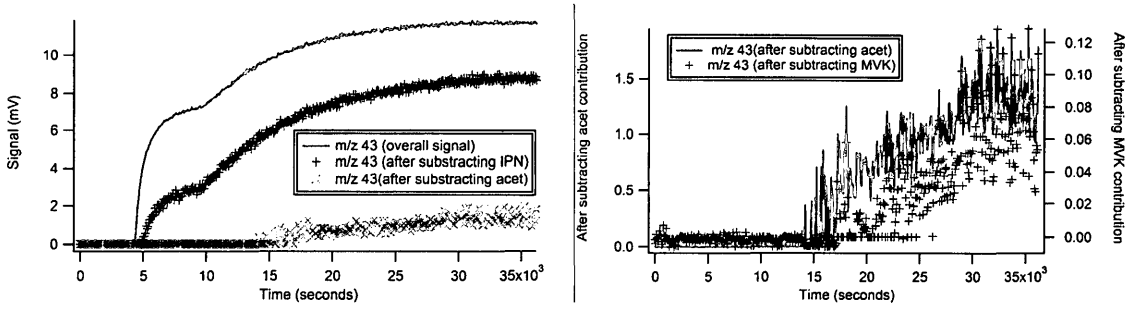

(a) (b)

Figure 5: Mass spectrum of m/z 43

a. Total ion count of m/z 43 (solid pink line) and residual ion count of m/z 43 after subtraction of IPN and acetone (grey markers (+))

b. Left hand side along y-axis is the residual ion count of m/z 43 after subtraction of isopropyl nitrite (IPN) and acetone (solid pink line) note that it's the same signal presented by grey markers in (a). Right hand side along y-axis is the residual ion count of m/z 43 after subtraction of IPN, acetone and methyl vinyl ketone [black markers (+)], indicating insignificant change after subtraction. Also the remaining data doesn't show satisfactory signal to assume a new ion and it might be noise.

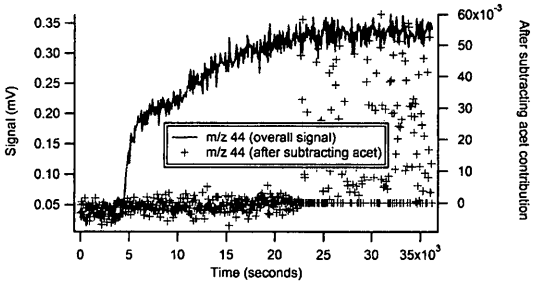

Figure 6: Mass spectrum of m/z 44
Left hand side along y-axis: total ion count of m/z 44 (solid brown line). Right hand side along y-axis (with different scale): residual ion count of m/z 44 after subtraction of acetone (black markers (+)) is noise, determining that m/z 44 is a pure acetone fragment.

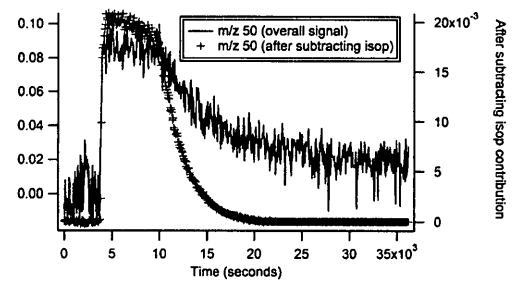

Figure 7: Mass spectrum of m/z 50
Left hand side along y-axis: total ion count of m/z 50 (solid sky blue line). Right hand side along y-axis (with different scale): residual ion count of m/z 50 after subtraction of isoprene (black markers (+)), indicate some isoprene left in the remaining signal.

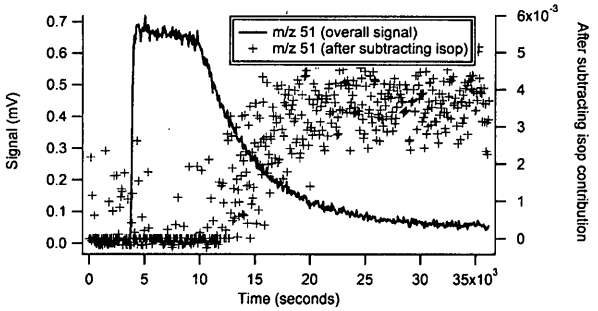

Figure 8: Mass spectrum of m/z 51
Left hand side along y-axis: total ion count of m/z 51 (solid red line). Right hand side along y-axis (with different scale): residual ion count of m/z 51 after subtraction of isoprene (black markers (+)), the remaining signal is different from isoprene and scattered, might be a minor product or noise.

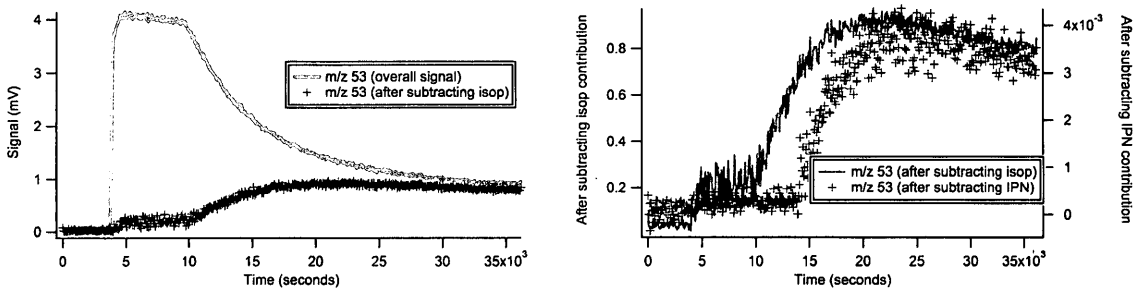

(a) (b)

Figure 9: Mass spectrum of m/z 53

a. Total ion count of m/z 53 (solid brown line) and residual ion count of m/z 53 after subtraction of isoprene (black markers (+)).

b. Left hand side along y-axis is the residual ion count of m/z 53 after subtraction of isoprene ((solid brown line) note that it's the same signal presented by black markers in (a). Right hand side along y-axis (with different scale) is the residual ion count of m/z 53 after subtraction of isoprene and isopropyl nitrite (IPN) [black markers (+)], looks like a minor product.

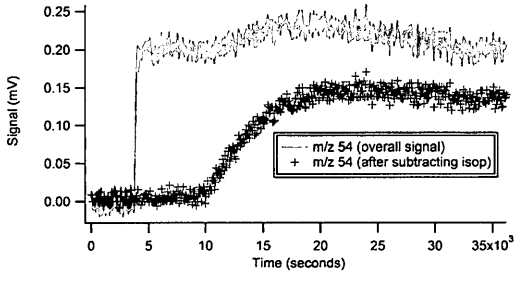

Figure 10: Mass spectrum of m/z 54
Total ion count of m/z 54 (solid pink line) and residual ion count of m/z 54 after subtraction of isoprene (black markers (+)), looks like a minor product.

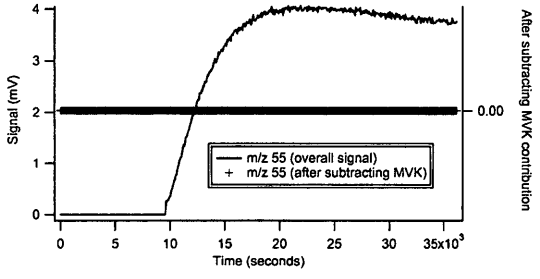

Figure 11: Mass spectrum of m/z 55
Left hand side along y-axis is total ion count of m/z 55 (solid green line). Right hand side along y-axis is residual ion count of m/z 55 after subtraction of methyl vinyl ketone (MVK) (black markers (+)), it is essentially zero signal because m/z 55 was used to calculate concentration of MVK changing with time.

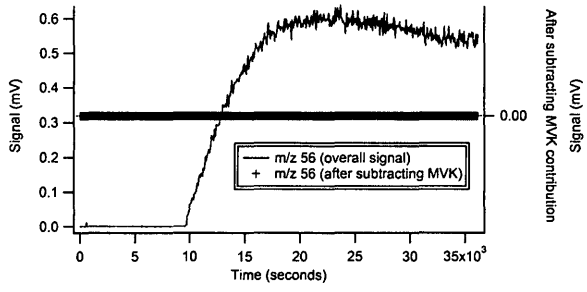

Figure 12: Mass spectrum of m/z 56 Left hand side along y-axis is total ion count of m/z 56 (solid grey line). Right hand side along y-axis is residual ion count of m/z 56 after subtraction of methyl vinyl ketone (MVK) (black markers (+)), it is essentially zero signal because m/z 56 (like m/z 55) was used to calculate concentration of MVK changing with time.

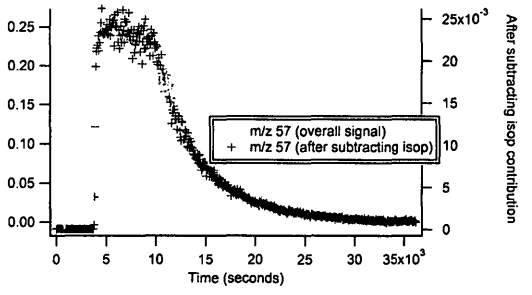

Figure 13: Mass spectrum of m/z 57 Left hand side along y-axis is total ion count of m/z 57 (solid yellow line). Right hand side along y-axis (with different scale) is the residual ion count of m/z 57 after subtraction of isoprene (black markers (+)), indicating some isoprene left in the remaining signal.

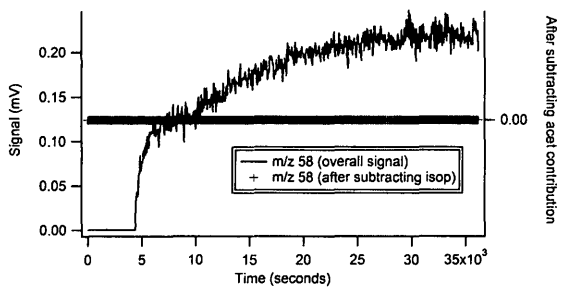

Figure 14: Mass spectrum of m/z 58 Left hand side along y-axis is total ion count of m/z 58 (solid light blue line). Right hand side along y-axis is residual ion count of m/z 58 after subtraction of acetone (black markers (+)), it is essentially zero signal because m/z 58 (like m/z 44) was used to calculate concentration of acetone changing with time.

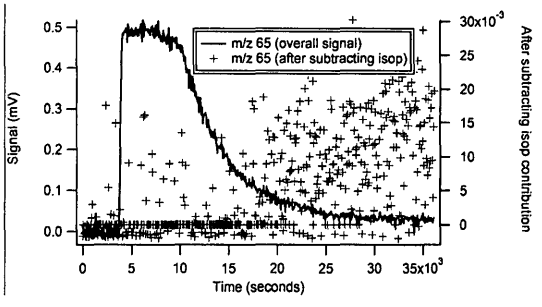

Figure 15: Mass spectrum of m/z 65 Left hand side along y-axis: total ion count of m/z 65 (solid royal blue line). Right hand side along y-axis (with different scale): residual ion count of m/z 65 after subtraction of isoprene (black markers (+)). The left over signal is random, therefore would be considered noise; showing that m/z 65 is a pure isoprene fragment.

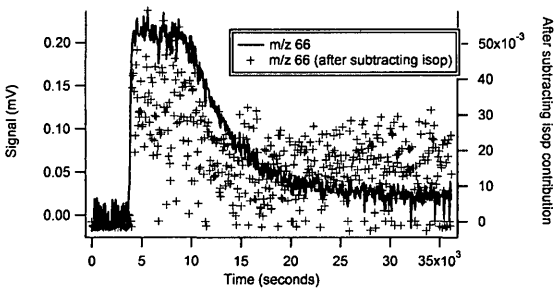

Figure 16: Mass spectrum of m/z 66
Left hand side along y-axis: total ion count of m/z 66 (solid dark green line). Right hand side along y-axis (with different scale): residual ion count of m/z 66 after subtraction of isoprene (black markers (+)), it is a scattered signal / noise; indicating m/z 65 to be pure isoprene fragment.

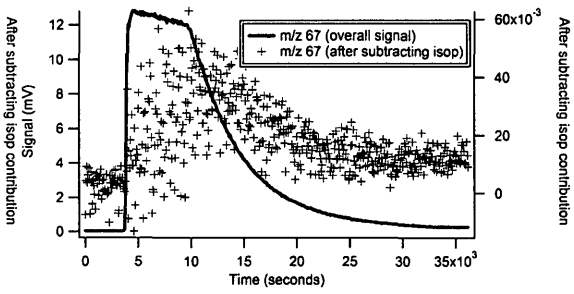

Figure 17: Mass spectrum of m/z 67
Left hand side along y-axis: total ion count of m/z 67 (solid light green line). Right hand side along y-axis (with different scale): residual ion count of m/z 67 after subtraction of isoprene (black markers (+)), it looks like noise, indicating that m/z 67 is a pure isoprene fragment.

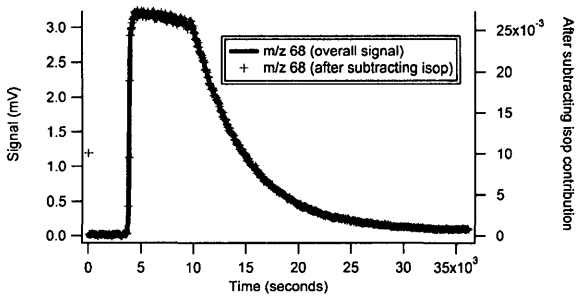

Figure 18: Mass spectrum of m/z 68
Left hand side along y-axis is the total ion count of m/z 68 (solid green line). Right hand side along y-axis (with different scale) is the residual ion count of m/z 68 after subtraction of isoprene (black markers (+)), indicate some isoprene left in the remaining signal.

[**Note**]: m/z 68 was used to calculate concentration of isoprene changing with time, but subtracted signal is not essentially zero. Unlike other masses, for example m/z 55 or 56 used to calculate concentration of MVK; isoprene fragments are highly volatile, making it difficult to determine the exact response factor of its fragment. This might be the issue here.

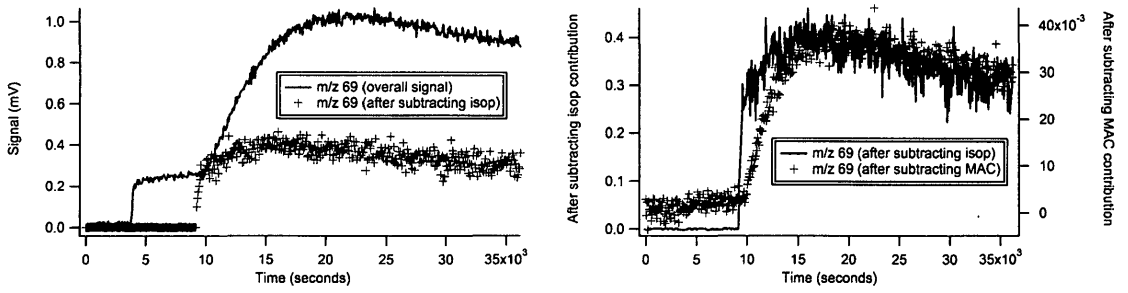

(a) (b)

Figure 19: Mass spectrum of m/z 69

a. Total ion count of m/z 69 (solid red line) and residual ion count of m/z 69 after subtraction of isoprene (black markers (+)).

b. Left hand side along y-axis is the residual ion count of m/z 69 after subtraction of isoprene ((solid red line) note that it's the same signal presented by black markers in (a). Right hand side along y-axis (with different scale) is the residual ion count of m/z 69 after subtraction of isoprene and methacrolein (MAC) [black markers (+)]. The remaining signal looks like a minor product, as it emerges after turning the UV lights on.

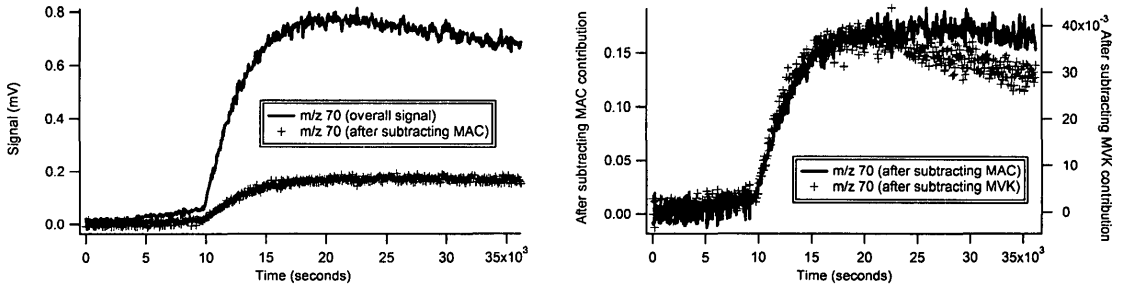

(a) (b)

Figure 20: Mass spectrum of m/z 70

a. Total ion count of m/z 70 (solid black line) and residual ion count of m/z 70 after subtraction of methacrolein (MAC) (black markers (+))

b. Left hand side along y-axis is the residual ion count of m/z 70 after subtraction of methacrolein (MAC) ((solid black line) note that it's the same signal presented by black markers in (a). Right hand side along y-axis (with different scale) is the residual ion count of m/z 70 after subtraction of methyl vinyl ketone (MVK) [black markers (+)]. Methacrolein or methyl vinyl ketone subtracted might have some portion left in the remaining signal.

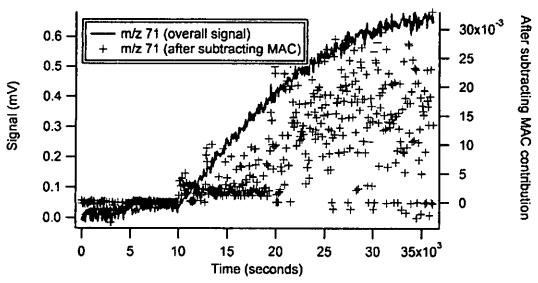

Figure 21: Mass spectrum of m/z 71
Total ion count of m/z 71 (solid light blue line) and residual ion count of m/z 71 after subtraction of methacrolein (MAC) (black markers (+)) which might be noise.

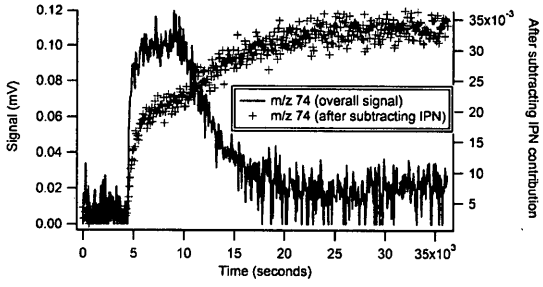

Figure 22: Mass spectrum of m/z 74
Total ion count of m/z 74 (solid dark purple line) and residual ion count of m/z 74 after subtraction of isopropyl nitrite (IPN) (black markers (+)) which might be a minor product and some left over IPN. [**Note**]: m/z 74 was used to calculate concentration of IPN changing with time, but subtracted signal is not essentially zero. Just like isoprene, IPN fragments are highly volatile, making it difficult to determine the exact response factors of its fragment.

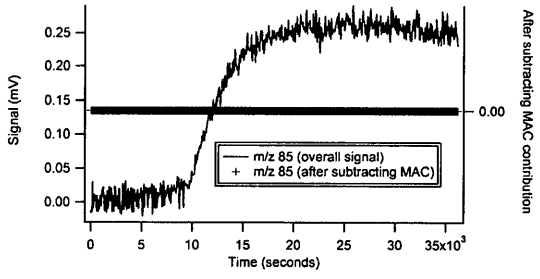

Figure 23: Mass spectrum of m/z 85
Left hand side along y-axis is total ion count of m/z 85 (solid grey line). Right hand side along y-axis is residual ion count of m/z 85 after subtraction of methacrolein (MAC) (black markers (+)), it is essentially zero signal because m/z 85 was used to calculate concentration of MAC as a function of time.